

TCNQ-based Supramolecular Architectures at Metal Surfaces

THÈSE N° 4859 (2010)

PRÉSENTÉE LE 15 DÉCEMBRE 2010

À LA FACULTÉ SCIENCES DE BASE

LABORATOIRE DE SCIENCE À L'ÉCHELLE NANOMÉTRIQUE

PROGRAMME DOCTORAL EN PHYSIQUE

ÉCOLE POLYTECHNIQUE FÉDÉRALE DE LAUSANNE

POUR L'OBTENTION DU GRADE DE DOCTEUR ÈS SCIENCES

PAR

Tzu-Chun TSENG

acceptée sur proposition du jury:

Prof. N. Grandjean, président du jury

Prof. K. Kern, directeur de thèse

Dr P. Broekmann, rapporteur

Prof. H. Brune, rapporteur

Prof. S. Tait, rapporteur



ÉCOLE POLYTECHNIQUE
FÉDÉRALE DE LAUSANNE

Suisse
2010

Abstract

Molecular self-assembly at metal surfaces has been recognized as an efficient strategy to create supramolecular nanoarchitectures with promising functionalities. The focus of this thesis lies on the strong electron accepting molecule 7,7,8,8-tetracyanoquinodimethane (TCNQ). The self-assembly of TCNQ and metal-TCNQ coordination networks on metal surfaces were investigated. The structural formation is directed by non-covalent interactions. By controlling fabrication parameters, surface coordination nanostructures with different chemical composition or molecular packing have been synthesized and characterized by scanning tunneling microscopy (STM). The electronic and magnetic properties of the surface organic or metal-organic nanostructures were studied by a combination of x-ray absorption spectroscopy (XAS) and x-ray photoelectron spectroscopy (XPS).

The thesis is organized into three parts. In the first part, the self-assembly of TCNQ molecules on Cu(100) and Ag(100) surfaces will be discussed. The two substrates provide different chemical environments as exhibited by the surface mobility of TCNQ. Charge transfer from either Cu(100) or Ag(100) substrate induces conformational bending of the $-C\equiv N$ cyano groups of TCNQ, which consequently facilitates the bonding of molecules to surfaces via nitrogen lone pairs. As shown by density functional theory (DFT) calculations, on Cu(100), the substrate-cyano interaction leads to local substrate reconstructions at the proximity of cyano groups. These charge-transfer induced structural modifications at the TCNQ/Cu(100) interface and the electrostatic interaction between molecules determine the self-assembly of TCNQ into long-range ordered domains. The adsorption and self-assembly of TCNQ on Ag(100) is presumably governed by a similar mechanism as concluded from the molecular packing and charge transfer phenomenon.

In the second part of this thesis, the fabrication of $MTCNQ_x$ ($M = Mn, Fe, Co,$ and Ni) coordination complexes on metal surfaces is presented. The molecular adsorption geometry in all structures indicates the participation of the cyano-substrate interaction in determining the final structures, except the $x = 1$ case in which all cyano groups are coordinated to metal adatoms. The competition between the coordination of TCNQ to metal adatom and TCNQ to substrate is shown by the growth phenomena on the Cu(100) and Ag(100) substrates. The weaker substrate interaction provided by the Ag(100) substrate results in multiple ordered phases ($x = 1, 2,$ or 4), in contrast to the single ordered $x = 2$ phase on Cu(100). The $MTCNQ_2$ networks synthesized on both substrates are

isostructural apart from a rotation of the network orientation to adapt the substrate periodicities. This highlights the importance of the substrate lattice in guiding the growth of supramolecular networks as well as the robust intra-network interaction to obtain a stable structure. The inherent chemical reactivity of Mn, Fe, Co and Ni atoms, which can be further modified upon adsorption due to substrate hybridization, strongly influences the resultant coordination structures. In addition to metal coordination, hydrogen bonding also plays a role in the stabilization of metal-TCNQ networks. Adjusting the substrate temperature has been an important and effective method to tune the interplay between adsorbate-adsorbate and adsorbate-substrate interactions. These experiments provide a systematic investigation on the formation of metal-TCNQ coordination structures on metal surfaces.

In the last part of this thesis, the electronic and magnetic properties of the MTCNQ_x complexes on metal surfaces will be discussed. XPS measurements and DFT calculations show that both the substrate and metal coordination atoms contribute to the electron donation to TCNQ molecules. The magnetic properties of the metal coordination centers were studied in x-ray magnetic circular dichroism (XMCD) measurements. The Mn centers are found to be paramagnetic from 300 K to 8 K. The Mn-coordinated networks represent ordered arrays of magnetic atoms carrying a high spin moment of $S = 5/2$. In the case of Ni-coordinated networks, the magnetism of Ni centers is induced by TCNQ coordination and dehybridization from the substrate. These results show the interesting physical phenomena emerging in two-dimensional metal-organic coordination systems.

Key words: *self-assembly, scanning tunneling microscopy, x-ray absorption spectroscopy, x-ray photoelectron spectroscopy, ultra-high vacuum, density-functional theory, TCNQ, transition metal, Cu(100) surface, Ag(100) surface, charge-transfer, reconstruction, metal-organic coordination*

Zusammenfassung

Molekulare Selbstorganisation auf Metalloberflächen hat sich als eine effiziente Strategie herausgestellt, um Supramolekulare Nanostrukturen mit vielversprechenden Eigenschaften herzustellen. Der Fokus dieser Arbeit liegt auf dem elektronenaffinen Molekül 7,7,8,8-tetracyanoquinodimethane (TCNQ). Die Selbstanordnung von TCNQ und Metall-TCNQ Koordinationsnetzwerken auf Metalloberflächen wurde untersucht. Das strukturelle Gefüge wird von nicht-kovalenten Wechselwirkungen gesteuert. Durch Kontrolle der Herstellungsparameter wurden zweidimensionale Koordinationsnanostrukturen mit verschiedener chemischer Zusammensetzung und molekularer Packung synthetisiert und mit einem Rastertunnelmikroskop (STM) analysiert. Die elektronischen und magnetischen Eigenschaften der organischen, bzw. metall-organischen Nanostrukturen, wurden mit Röntgenabsorptionsspektroskopie (XAS) und Röntgenphotoelektron-Spektroskopie (XPS) untersucht.

Die Arbeit gliedert sich in drei Teile. Als erstes wird die Selbstanordnung von TCNQ auf Cu(100) und Ag(100) Oberflächen behandelt. Diese Substrate bieten jeweils eine unterschiedliche chemische Umgebung für die Adsorbate, was durch deren Oberflächenmobilität deutlich wird. Ladungstransfer vom Cu(100) oder Ag(100) Substrat induziert eine konformative Krümmung der $\text{-C}\equiv\text{N}$ Cyanogruppen von TCNQ, was eine Bindung der Moleküle mit der Oberfläche über das freie Elektronenpaar des Stickstoffs ermöglicht. Dichtefunktionaltheorie (DFT) Rechnungen haben ergeben, dass auf Cu(100), Cyano-Substrat Wechselwirkungen zu lokalen Oberflächenrekonstruktionen in der Umgebung der Cyanogruppen führen. Diese durch Ladungstransfer induzierten Strukturänderungen der TCNQ/Cu(100) Grenzfläche und die elektrostatischen Wechselwirkungen zwischen den Molekülen bestimmen die Anordnung von TCNQ in langreichweitig geordnete Domänen. Die molekulare Anordnung und Ladungstransfereigenschaften deuten an, dass die Adsorption und Selbstanordnung von TCNQ auf Ag(100) durch einen ähnlichen Mechanismus bestimmt sein könnte.

Der zweite Teil konzentriert sich auf die Synthese von MTCNQ_x ($\text{M} = \text{Mn, Fe, Co}$ oder Ni) Komplexen auf Metalloberflächen. Die Adsorptionsgeometrie in fast allen Netzwerken deutet darauf hin, dass Cyano-Substrat Wechselwirkungen die endgültige Struktur mitbestimmen, mit Ausnahme einer 1:1 Mischung, in der alle Cyanogruppen eine Koordinationsbindung mit einem Metallatom eingehen. Der Wettbewerb zwischen den Wechsel-

wirkungen innerhalb der Adsorbate (Koordinationsbindungen) und den Wechselwirkungen von Adsorbaten mit dem Substrat wird im unterschiedlichen Wachstumsverhalten auf Cu(100) und Ag(100) deutlich. Eine schwächere Wechselwirkung mit dem Substrat, was bei Ag(100) der Fall ist, führt zu verschiedenen geordneten Phasen für $x = 1, 2$ oder 4, wohingegen auf Cu(100) nur eine einzige geordnete Phase ($x = 2$) beobachtet wird. Auf beiden Substraten haben die MTCNQ₂ Netzwerke die gleiche Struktur, abgesehen von einer Rotation der Netzwerkorientierung, um die unterschiedliche Oberflächenperiodizität auszugleichen. Dies unterstreicht sowohl die Bedeutung des Substratgitters beim Steuern des Wachstums der supramolekularen Netzwerke als auch die robusten Wechselwirkungen zwischen den Adsorbaten, um eine stabile Struktur zu erhalten. Die chemische Reaktivität von Mn, Fe, Co und Ni Atomen, die noch zusätzlich durch Hybridisierung mit dem Substrat modifiziert wird, bestimmt die resultierenden Koordinationsstrukturen im Wesentlichen mit. Neben Koordinationsbindungen, tragen auch Wasserstoffbrückenbindungen zur Stabilisierung der Metall-TCNQ Netzwerke bei. Die Kontrolle der Substrattemperatur ist ein wichtiger und effizienter Ansatz, um das Wechselspiel zwischen Adsorbat-Adsorbat und Adsorbat-Substrat Wechselwirkungen einzustellen. Diese Experimente liefern eine systematische Untersuchung des Wachstums von Metall-TCNQ Koordinationsstrukturen auf Metalloberflächen.

Im letzten Teil dieser Arbeit, werden die elektronischen und magnetischen Eigenschaften von MTCNQ_x auf Metalloberflächen behandelt. XPS Messungen und DFT Rechnungen zeigen, dass sowohl das Substrat als auch die koordinierten Metallatome zur Elektronenabgabe an TCNQ beitragen. Die magnetischen Eigenschaften der Metallkoordinationszentren wurden mit zirkularen magnetischen Röntgenschroterismus (XMCD) Messungen untersucht. Die Mn Zentren erweisen sich im Messbereich von 300 K bis 8 K als paramagnetisch. Die Mn koordinierten Netzwerke stellen geordnete Gitter von magnetischen Atomen dar, mit einem Moment von $S = 5/2$. Im Fall der Ni koordinierten Netzwerke wird das magnetische Moment der Ni Zentren durch TCNQ Koordination und Dehybridisierung vom Substrat induziert. Diese Ergebnisse zeigen die interessanten physikalischen Phänomene, die in zwei-dimensionalen metall-organischen Koordinationssystemen hervortreten.

Schlüsselbegriffe: *Selbstanordnung, Rastertunnelmikroskopie, Röntgenabsorptionsspektroskopie, Röntgenphotoelektron-Spektroskopie, Ultrahochvakuum, Dichtefunktionaltheorie, TCNQ, Übergangsmetal, Cu(100) Oberfläche, Ag(100) Oberfläche, Ladungstransfer, Rekonstruktion, metall-organische Koordination*

Contents

Abstract	i
Zusammenfassung	iii
Contents	vi
Abbreviations	vii
1 Introduction	1
2 Experimental and Theoretical Foundations	7
2.1 Experimental Methods	7
2.2 Experimental Set-up	16
2.3 Sample Preparation	18
3 Structure and Charge Transfer of TCNQ on Metal Surfaces	23
3.1 Charge Transfer-Induced TCNQ self-assembly on Cu(100)	24
3.2 TCNQ self-assembly on Ag(100)	35
3.3 Summary and Comparison	41
4 Metal-TCNQ Coordination Structures on Metal Surfaces	43
4.1 Mn, Fe, Co, Ni-TCNQ coordination structures on Cu(100)	44
4.2 Mn, Ni-TCNQ coordination structures on Ag(100)	51
4.3 Summary and Comparison	65
5 Physical Properties of Metal-TCNQ Coordination Structures	69
5.1 Charge Transfer of Metal-TCNQ coordination structures on Cu(100) . . .	70
5.2 Magnetic Properties of Metal-TCNQ Coordination Structures	76

6 Summary and Perspectives	85
Bibliography	89
Publications	105
Acknowledgements	107
Curriculum Vitae	109

Abbreviations

1D, 2D, 3D	one-, two-, three-dimensional
ALD	atomic layer deposition
CPS	counts per second
DOS	density of states
FCC	face-centered cubic
LEED	low energy electron diffraction
ML	monolayer
MOCN	metal-organic coordination network
NEXAFS	near edge x-ray absorption fine structure
TEY	total electron yield
STM	scanning tunneling microscopy
TCNE	tetracyanoethylene
TCNQ	tetracyanoquinodimethane
UHV	ultra high vacuum
XAS	x-ray absorption spectroscopy
XMCD	x-ray magnetic circular dichroism
XPS	x-ray photoelectron spectroscopy

Chapter 1

Introduction

Nanoscience has emerged in the early 1980s along with the development of novel experimental and theoretical tools which enable the investigation of materials at an atomic scale. Since then, big advances in research have led to the detailed understanding of physical phenomena, especially those dominant only in the quantum mechanical regime. Such fundamental insight into and control over materials have brought new science into novel applications. The last decades have seen the booming of semiconductor electronics and magnetic information storage, which are the best examples of how science revolutionizes our daily lives. The current semiconductor fabrication technology is a top-down approach, compiling precise iterations of deposition and surface patterning to create integrated circuits. As device miniaturization continues and requires more and more sophisticated equipments, a bottom-up self-assembly approach is generally considered as a more efficient way to create nanostructures. A bottom-up approach utilizes the concept of self-assembly where complex products are fabricated from relatively simple building blocks through possibly a few hierarchical steps. In fact, a few bottom-up methods are already integrated into current semiconductor fabrication, for example, atomic layer deposition (ALD). Concomitant with the development of bottom-up strategies, synthesis and manipulation of useful building blocks become important. Recently many groups of materials have been extensively studied, such as artificial carbon materials (fullerenes, CNTs and graphene), inorganic nanostructures (particles, fibers and clusters) and organic molecules (proteins, DNA and other artificial molecules). Among all these materials, molecules form a category of chemistry which is termed "supramolecular chemistry" by Dr. Jean-Marie Lehn in the early 1970s [1].

Supramolecular chemistry is the chemistry of the intermolecular non-covalent bonds,

in contrast to strong covalent and ionic bonds. It focuses on systems of molecules recognizing each other and choosing with which others they will form complexes. Such weak and reversible intermolecular forces are essential for most biological processes which usually involve complex reaction units. For example, DNA consists of two long molecules held together by hydrogen bonds in the shape of a double helix. The use of hydrogen bonds is vital to DNA replication that allows the two strands to be pulled apart like a zipper and used to template new double stranded DNA. Many synthetic supramolecular systems are inspired by biological reactions and this field of research is fueled by the interests to efficiently and precisely fabricate materials of multiple properties in a relatively simple way as nature does. Molecular self-assembly is the key concept of supramolecular chemistry. Self-assembly is activated by pre-programmed linkages of individual building blocks which lead to spontaneous formation of desired structures. Functionalities can also be designed through chemical methodologies. Along with the vast, virtually limitless, variety of molecular building blocks that can be synthesized, supramolecular self-assembly has made great advances and is still a growing field nowadays [2–10]. An important discovery at the beginning of supramolecular chemistry is the synthesis of the size-selective alkali metal cation receptors of crown ethers [15]. Today the detailed understanding of intermolecular forces has led to more sophisticated achievements, for example, molecular machines, "lock and key" recognition systems and complex structures for various purposes. To integrate more functionalities into supramolecular systems, various structural units (for appropriate spacing and conformation), photo- and electro-active molecules (porphyrins, phthalocyanines and quinones) and biomimetic building blocks are designed. Therefore, although termed "chemistry", supramolecular chemistry is actually an interdisciplinary field of organic, inorganic, physical and biological aspects. In addition to the catalysis mentioned already, charge transfer and redox properties, which are related to chemical reactivity of metal-organic structures, have attracted much scientific and technological attention. Molecular magnetism is nowadays another topic of great interest and importance under the category of supramolecular coordination chemistry. Molecule-based magnets, from single molecules to bulk crystals, are recently extensively studied [16–19]. They have shown intriguing and interesting physical properties. Apart from scientific importance, molecular magnets are envisioned as potential alternatives to conventional metal-based magnets for apparent advantages, including simple fabrication (low-temperature chemical routes), tunability of magnetic properties through synthesis and possibility to create surface-supported thin films or monolayers compatible with modern technology.

Surfaces and interfaces are of great scientific interests because an interface is where two phases or materials come into contact and where physical effects emerge. From the application point of view, interface properties are of paramount importance since modern technologies will most likely be supported on surfaces. In semiconductor industry, surface effects become more and more dominant due to high surface/volume ratio and have resulted in issues of device fabrication and performance as feature size continues to shrink. To tackle these difficulties, surface science focuses on the physical and chemical reactions occurring on both sides of an interface and is certainly one of the most active fields of research at present. Since the development of scanning probe microscopy techniques in the early 1980s many surface-induced phenomena have been studied at an unprecedented level of understanding and precision down to an atomic scale. Especially scanning tunneling microscopy (STM) has served as a powerful tool which offers a real space sub-angstrom resolution [20, 21]. Complemented by other analytical instruments, it has demonstrated its unparalleled importance in surface science.

Structuring surfaces has been an effective strategy to impose functionalities on materials. The above mentioned semiconductor fabrication is one of the most successful examples showing the great power of combining a multitude of top-down surface patterning steps to achieve desired performances. An opposite bottom-up approach is the atom-by-atom manipulation enabled by scanning probe techniques, which has attracted a lot of scientific interests [22–25]. Other examples of bottom-up surface patterning utilizing the concept of self-assembly include selective thin film growth, chemical functionalization for sensing and catalysis and deposition of artificial or biological molecules. We are especially interested in the molecular self-assembly on surfaces, which is also termed "two-dimensional (2D) supramolecular chemistry." The core of 2D supramolecular chemistry lies in the control of the growth phenomena of building blocks. First of all, an organic molecule has a well-defined geometry and possibly multiple functional groups. The adsorption of a molecule is then determined by multiple interactions at different locations of a molecule, which renders the adsorption configuration more complicated than atomic species. Due to such multiple point interaction, molecules are often flat-adsorbed on surfaces, apart from a few exceptions. In addition to molecular building blocks, metal atoms are also employed as coordination nodes in 2D supramolecular structures, which are called "metal-organic coordination networks (MOCNs)." The adsorption of metal atoms on metal surfaces is relatively simple. Individual atoms can be regarded as spheres which usually reside on hollow sites of a substrate. Upon metal-organic coordination, the coordination geometry

can be very different from the bulk phase due to the spatial confinement imposed by the surface. Therefore, although a lot of the growth behaviors on surfaces can be linked to and understood in the knowledge of solution-based supramolecular chemistry, it is inappropriate to directly translate supramolecular interaction principles derived from solution chemistry to substrate-supported systems. The presence of a substrate can lead to effects that cannot be fully predicted yet. In the following some principles governing the 2D supramolecular self-assembly will be discussed.

The surface mobility of building blocks is one of the most important parameters which determine the resultant structure. When the surface mobility is low, adsorbates stick on the substrate as deposited and the resultant structure is thus controlled by the kinetics of the system. On the other hand, when the surface mobility is high, adsorbates are allowed to move freely and assemble into the thermodynamic equilibrium structure. In the intermediate situations, the structural formation is mediated by the competition between kinetics and thermodynamics. Annealing has been a very important and effective strategy to tune coordination structures, attributed to the subtle bonds that can be broken and rejoined easily by annealing or cooling [26–32]. By increasing the substrate temperature, adsorbates gain thermal energy and the balance of the coordination reaction can be shifted towards the thermodynamic equilibrium.

The adsorbate-adsorbate interactions within the MOCN layer have to be considered. Three main interactions will be discussed here, including electrostatic forces, hydrogen bonding and metal coordination. Electrostatic interactions, although not directional, can significantly influence the molecular self-assembly, especially in charge transfer systems. Hydrogen bonding plays an important role in biological systems. The base pairing mechanism of DNA helixes represents the selectivity and directionality of hydrogen bonding which are vital to DNA functions in all living organisms. Although one single hydrogen bond is weak, multiple bonds between two components are often encountered, which lead to an overall significant strength enabling the formation of a stable structure. Metal coordination force is another widely used strategy to organize molecular components into supramolecular architectures [2, 6–10]. It is characterized by enhanced rigidity, selectivity and directionality in comparison with hydrogen bonding. The incorporation of metal ions into 2D supramolecular networks allows the design of structures with a higher level of structural complexity due to the possible multiple coordination numbers of metal ions. Nevertheless, metal ions possess distinct charge and spin states which lead to particular electronic and magnetic properties of metal-organic networks. Both hydrogen bonding

and metal coordination possess well-defined strength and directionality. Therefore, the spatial arrangement of building blocks can be steered by the choice of appropriate bonding motifs.

In addition to lateral adsorbate-adsorbate interactions, the adsorbate-substrate interaction is another significant parameter governing the supramolecular growth. When the substrate simply acts as a support, the molecules or metal atoms physisorb on the surface via van der Waals forces without changing their electronic state or chemical nature. Oppositely, chemisorption involves reactions such as charge transfer, bond formation, dissociation, etc. Most molecular assemblies supported on surfaces are influenced by the substrate symmetry and periodicity, leading to repeated patterns in a long-range scale. Substrate interaction can more reactively modify the chemical and electronic properties of adsorbed molecules and metal atoms, which simultaneously influence the coordination structures. On the other hand, molecules have been shown to induce substrate reconstruction or facetting upon adsorption [11, 12]. Such adsorbate-induced reconstructions can further lead to specific molecular arrangements on surfaces [13, 14]. The interplay among the various interactions discussed above determines the growth phenomenon of 2D supramolecular coordination networks. At the current stage of 2D supramolecular chemistry, there are still many open questions to be explored to gain full control over the growth of molecular nanostructures.

This thesis presents the results of the investigation on supramolecular architectures based on the molecule 7,7,8,8-tetracyanoquinodimethane (TCNQ) at Cu(100) and Ag(100) metal surfaces. Since the discovery of tetracyanoethylene (TCNE) in 1958 [33], its unusual reactivity has prompted intense studies on molecules containing cyano functional groups and has led to the discovery of TCNQ in 1962 [34]. TCNQ molecules are characterized by strong electron affinity. Charge transfer compounds based on TCNQ and related molecules have exhibited exceptional properties, such as metallic conductivity in TTF-TCNQ [35] and magnetism in various metal cyanide complexes [36–43]. Structural models are lacking, particularly for most M-TCNE and M-TCNQ (M = metal) compounds, due to their amorphous or only short-range ordered structures. Despite the structural uncertainty, magnetic ordering of metal cyanide materials has been proposed to arise from exchange interactions between localized spins on the metal ions and spins on the cyano radical anions. The aim of this study is to understand the M-TCNQ coordination interactions and the potential physical properties in these systems. We started with depositing submonolayer TCNQ on metal surfaces to investigate the interaction occurring

at the interface of TCNQ and metal substrates. Then, we proceeded to the fabrication of surface-supported M-TCNQ complexes. Structural formation principles were revealed by scanning tunneling microscopy with an unprecedented precision. Chemical and physical information was provided by a combination of x-ray absorption techniques.

The thesis is organized as follows:

Chapter 2 provides the technical background of this work. A brief introduction of scanning tunneling microscopy (STM), x-ray photoelectron spectroscopy (XPS), near edge x-ray absorption fine structures (NEXAFS) and x-ray magnetic circular dichroism (XMCD), will be given. Afterwards the experimental set-up and sample preparation will be described in detail.

Chapter 3 of this thesis concerns the self-assembly of TCNQ molecules on metal substrates. On Cu(100), a structural rearrangement of both the molecule and the metal surface atoms after charge transfer across the interface has been observed. The self-assembly phenomenon of TCNQ on Ag(100) has exhibited distinct differences to that on Cu(100). In particular, TCNQ has a high mobility on Ag(100). Despite the difference in surface mobility, it has been concluded that a similar interaction is responsible for the adsorption of TCNQ on Ag(100) based on structural and spectroscopic analysis.

Chapter 4 is devoted to metal-TCNQ coordination complexes. M-TCNQ ($M = \text{Mn, Fe, Co, and Ni}$) complexes on Cu(100) have exhibited drastic differences in the structural ordering. On the other substrate, Ag(100), Mn and Ni metals were chosen to shed light on the clarification of coordination principles. The hierarchical and the thermally-activated self-assembly reflect the importance of both thermodynamic and chemical driving forces in the structural formation. The results also signify that the adsorbate-substrate interaction can alter considerably the chemistry of the adsorbates which is ultimately revealed in the formation or absence of ordered patterns. In addition to the structural information, the STM data, as a convolution of geometric contour and lateral variations in the charge density of the surface structure, have indicated distinct electronic configuration in M-TCNQ complexes on Cu(100) or Ag(100).

Chapter 5 focuses on the physical and chemical aspects of the M-TCNQ complexes on Cu(100) or Ag(100). The first part contains the charge transfer, valence state and electronic configuration of MnTCNQ_2 on Cu(100) deduced from XPS and DFT analyses. Then, the magnetic properties of the coordination networks investigated by XMCD measurements will be presented. Theoretical modelling is in progress to conclusively and quantitatively interpret our experimental results.

Chapter 2

Experimental and Theoretical Foundations

Section 2.1 gives an introduction to the analytical methods used in this thesis, including scanning tunneling microscopy (STM), x-ray photoelectron spectroscopy (XPS), near-edge x-ray absorption fine structure (NEXAFS) and x-ray magnetic circular dichroism (XMCD). The experimental set-up, sample preparation and the molecule of interest, TCNQ, will be described in Section 2.2 and 2.3.

2.1 Experimental Methods

Scanning Tunneling Microscopy (STM)

Scanning Tunneling Microscopy is based on the concept of quantum tunneling. A classical electron tunnel junction is composed of two electrode plates separated by an insulating film. The tunneling current flowing through the junction is exponentially dependent on the thickness of the insulating film [45]. The set-up of a STM is strongly correlated to this configuration in which the scanning tip and the conductive sample are the electrodes and the vacuum gap between them serves as the tunnel barrier (Figure 2.1). The tip can be positioned in three dimensions relative to the sample by piezoelectric drivers in x-, y- and z-directions. When the tip is sufficiently close to the surface, a tunneling current can occur. The tunneling current is to the first order analogous to the tunneling junction described above and therefore the amount is proportional to the probability of an electron tunneling through the vacuum gap between the sample and the tip:

$$I \propto e^{-2\kappa d} \quad (2.1)$$

where κ is the decay constant for the electron wave function in the vacuum gap of width d and can be expressed by

$$\kappa^2 = \frac{2m_e}{\hbar^2}(V_B - E) \quad (2.2)$$

where m_e is the electron mass, E is the electron energy and V_B is the potential barrier. Since the tunneling probability decreases exponentially with increasing barrier width, the tunneling current is very sensitive to the tip-sample distance d . Thus, small variations in the surface topology lead to big changes in the tunneling current signal. In the constant current mode, which is applied for all the STM images in this work, the tip-sample distance is adjusted by a feedback movement of the z-piezo to keep the tunneling current constant while scanning across the x-y plane. The vertical displacement of the tip, corresponding to the voltage applied on the z-piezo, versus the x-y position gives a contour map of the surface. Although this simple picture has been used to explain STM topographs, a more sophisticated consideration of the real system has to be taken to include important issues, e.g., the electronic structure of the tip and the local density of states (LDOS) on the surface (cf. Figure 2.1). At the general surface-tip distances of a few angstroms, the surface-tip interaction can be neglected. Therefore the tunneling current can be calculated in the first-order perturbation theory in terms of the wave functions determined separately for the surface and the tip [46–49]. The tunneling current can be written as

$$I \propto \int_0^V \tau(E, V, d) \rho_s(E, x, y) \rho_t(E - V) dE \quad (2.3)$$

where $\tau = e^{-2\kappa' d}$ is the tunneling transmission factor, ρ_s is the DOS on the sample which is dependent on the (x,y) position, ρ_t is the DOS associated with the tip and V is the bias voltage on the sample. κ' can be expressed in a similar form to Equation 2.2 as

$$\kappa'^2 = \frac{2m_e}{\hbar^2} \left[\frac{1}{2}(W_s + W_t + V) - E \right] \quad (2.4)$$

where W_s and W_t are the work functions of sample and tip, respectively (cf. Figure 2.1). Equation 2.3 contains the essential physics and is a good starting point for qualitative interpretation of STM tunneling current and topographs. The transmission factor τ reflects the surface topology by the parameter d . The electronic structure of both the sample and the tip are taken into account by ρ_s and ρ_t . Therefore, in interpreting STM images, it

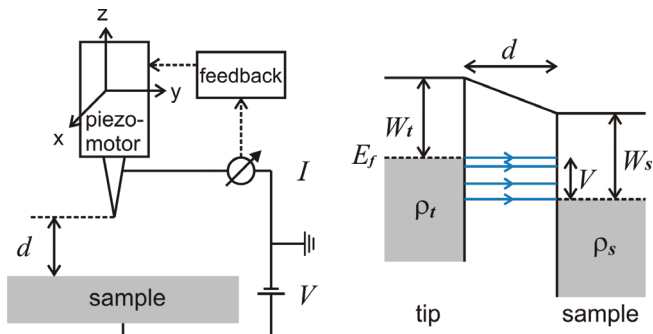


Figure 2.1: Schematic representations of a scanning tunneling microscope and the corresponding potential energy diagram.

is extremely important to keep in mind that both the profile and the height of an object are the convoluted result of the spatial topology and electronic configuration of the whole system. In the case of molecular adsorbates, the STM patterns often show sub-molecular structures related to molecular orbitals rather than actual atomic positions, especially the more accessible orbitals close to the Fermi level, i.e., the highest occupied (HOMO) and lowest unoccupied (LUMO) molecular orbitals. Scanning tunneling microscopy is unique in providing high resolution topography and at the same time electronic information. Combined with other analytical tools and theoretical calculations, it has been demonstrated to be very reliable in the characterization of supramolecular assemblies on surfaces.

X-ray Photoelectron Spectroscopy (XPS)

X-ray photoelectron spectroscopy (XPS) is a quantitative spectroscopic technique that measures the chemical state and electronic state of elements existing in a sample and allows the determination of element composition of a huge variety of materials, e.g., metals, oxides, ceramics, organics and even biological samples. This technique is based on the photoelectric effect, which is the phenomenon that an electron absorbs the energy of a

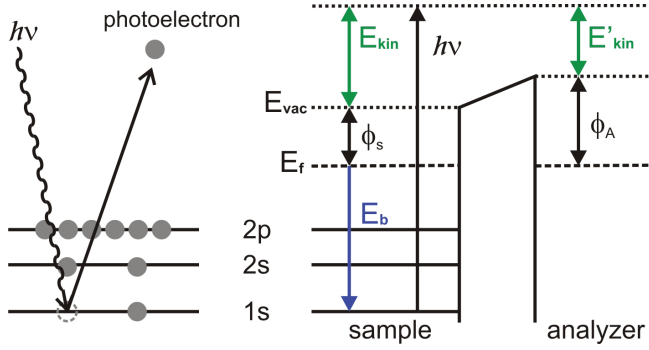


Figure 2.2: Schematic representation of the photoelectron emission and the corresponding energy diagram. The electrons excited by photons escape the sample at energy E_{kin} and enter the analyzer at E'_{kin} . Knowing the work function of the analyzer, the binding energy of electrons specific to their electronic configurations can be calculated. XPS spectra are then obtained by plotting the number of electrons versus their binding energy.

photon and consequently has enough energy to escape a material. It is therefore a simple process of single photon in and single electron out. The process and the corresponding energy diagram are illustrated in Figure 2.2. Monochromatic photons of energy $h\nu$ are shined on a sample, leading to the ionization and emission of core electrons. The kinetic energy and the number of the emitted electrons, which are called photoelectrons, are measured. Energy conservation according to

$$E_{kin} = h\nu - E_b - \phi_s \quad (2.5)$$

has to be satisfied (cf. Figure 2.2), where E_b is the binding energy of the electron and ϕ_s is the work function of the sample. As illustrated in Figure 2.2, the Fermi levels of both sides are aligned by an electrical contact between the sample and the spectrometer. The electrons enter the analyzer at the energy E'_{kin} . The work function of the analyzer ϕ_A is a known value if the spectrometer is correctly calibrated. Therefore the binding energy is obtained without knowing the work function of the sample.

A typical XPS spectrum is a plot of the number of electrons detected (counts per second, CPS) versus the binding energy of these electrons. Each element produces a characteristic set of XPS peaks at characteristic binding energy values that directly iden-

tify each element that exist in the sample. These characteristic peaks correspond to the electronic configuration of the atoms, e.g., 1s, 2s, 2p, 3s, etc. The XPS peak intensity is proportional to the probability of the photoelectric effect, which is related to an element-specific cross section factor. The ratios of the peak intensities after normalization by the cross section factors correspond to the chemical stoichiometry of the sample. For a given element the cross section of photoionization is independent on the valence state of the atoms. The background correction is usually done by the method established by Shirley [50]. In the case of molecules of submonolayer coverage adsorbed on surfaces, the concentration of the analyzed element is low, and thus it is often necessary to use the spectra recorded on clean substrates for background substration.

XPS is advantageous in distinguishing atoms at different electronic or chemical states. A clear example is the change in binding energy, which is called core level shift or chemical shift, between a metal and its oxide. In the oxide form, i.e., positively charged metal ion, the XPS peak is shifted to larger binding energies. The reason is that when a metal atom loses an electron in the outermost shell, the leftover electrons feel a stronger Coulomb interaction from the atom nucleus. Therefore it takes more energy to excite electrons in a positively charged atom. Similarly, in the investigation of molecules, it is more important to identify the energy shift between different chemical states than the absolute value of a particular core level. The atoms in a molecule are under different environments, e.g., different neighboring atoms, bondings or charge states. The power of XPS is the ability to identify and analyze these atoms quantitatively.

More details can be found in Reference [51].

Near Edge X-ray Absorption Fine Structure (NEXAFS)

Near Edge X-ray Absorption Fine Structure (NEXAFS) spectroscopy refers to the absorption fine structure close to an absorption edge, within about 30eV above the actual edge. Opposite to the XPS technique where the incident photon energy is fixed and the photoelectron intensity is measured as a function of electron binding energy, in NEXAFS the x-ray energy is scanned and the absorption is measured as a function of incident photon energy. If the incident energy is just sufficient to excite a core electron, the photoelectron will jump into empty states above the Fermi level, leading to fine structures in the NEXAFS spectrum associated with excitations into unoccupied orbitals.

NEXAFS has particular applications to molecules adsorbed on surfaces. Using linearly

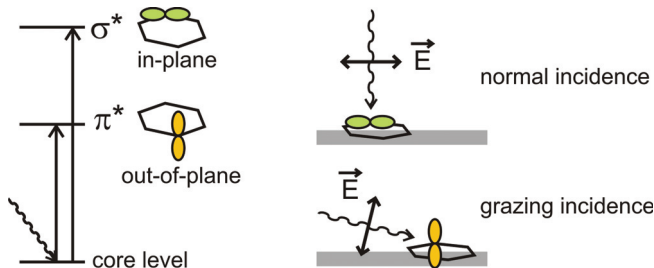


Figure 2.3: Schematic representation of the angular dependence of NEXAFS spectra which enables the identification of orbital symmetry and the corresponding energy.

polarized x-rays, information concerning the orientation of the molecule can be deduced from the polarization dependence of NEXAFS resonances. The resonances originate from the electronic transition of core electrons to unoccupied valence orbitals. According to the symmetry of the valence orbital the NEXAFS peaks can be labeled as σ^* or π^* . The excitation process is governed by dipole selection rules, which leads to strong resonances when the electric field vector \vec{E} of the linearly polarized x-rays is along the orbital orientation, and vice versa. A well-known example is the benzene molecule having the σ^* and π^* orbitals in- and out-of the molecular plane, respectively (left part of Figure 2.3). As illustrated on the right-hand side of Figure 2.3, when the benzene molecule is flat-lying on a surface, the NEXAFS resonance corresponding to the in-plane σ^* orbital will be prominent at normal incidence. On the other hand, the peak corresponding to the out-of-plane π^* orbital will dominate the NEXAFS spectrum at grazing incidence. By analyzing the angular dependence of the NEXAFS peaks, the orbital orientation and the associated bond angles can be determined. Detailed information on the curve fitting of NEXAFS spectra and determination of molecular orientations on surfaces is available in literature [52–55]. First of all, NEXAFS spectra usually require background correction. The spectra contain step-like features due to excitation of electrons into a continuum final state, such as free electron states. For molecules adsorbed on metallic surfaces, such steps occur due to the transition of molecular core electrons into metal continuum states, which can hybridize with molecular states and further complicate the near edge lineshape. The step background is given by [52, 54]:

$$\begin{aligned}
I_{step} &= H\left[\frac{1}{2} + \frac{1}{2}\operatorname{erf}\left(\frac{E-P}{W/c}\right)\right], \quad E \leq P+W \\
&= H\left[\frac{1}{2} + \frac{1}{2}\operatorname{erf}\left(\frac{E-P}{W/c}\right)\right]\exp[-d(E-P-W)], \quad E > P+W
\end{aligned} \tag{2.6}$$

where H is the height of the step; P is the position of the inflection point of the step; W is the FWHM (full width at half maximum) of the step; c is a constant defined by $c = 2\sqrt{\ln 4}$. The exponential term describes the decay of the step background above the edge due to decreased overlap between the initial and the final states in the electronic transition, which is shown to influence the NEXAFS lineshape strongly in many systems [56, 57]. After appropriate background subtraction, the spectra can be fitted by peaks representing specific bonds or orbitals. The angular dependence of the peak intensity originates from the electron transition probability, which is highest when the the x-ray \vec{E} vector is along the orientation of either σ^* or π^* orbitals (right part of Figure 2.3). Since the incident angle is known, the orientation of the orbitals can be calculated. Following J. Stöhr and D. A. Outka [52, 55], the orbitals are categorized into two groups by their spatial distribution, i.e., the vector- and plane-type. The vector-type orbital is characterized by a vector along the bonding while the plane-type has its normal parallel to the bonding. In order to account for the not-fully-linearly polarized synchrotron radiation, a \mathbf{E}^\perp component, in addition to the major \mathbf{E}^\parallel component, is defined. Thus, the angular dependence of the resonance intensities for three-fold or higher substrate symmetry, for the vector case, is expressed by:

$$I_v^\parallel = A(\cos^2 \beta \sin^2 \theta + \frac{1}{2} \sin^2 \beta \cos^2 \theta) \tag{2.7}$$

$$I_v^\perp = \frac{1}{2} A \sin^2 \beta \tag{2.8}$$

and, for the plane case, by:

$$I_p^\parallel = B(1 - \cos^2 \gamma \sin^2 \theta - \frac{1}{2} \sin^2 \gamma \cos^2 \theta) \tag{2.9}$$

$$I_p^\perp = \frac{1}{2} B(1 + \cos^2 \gamma) \tag{2.10}$$

where A and B are constants; θ is the angle between the incidence and the surface normal; β and γ are the angles of the surface normal to the polar angle of vector-like orbital and

plane-like orbital, respectively. The measured intensity contains contributions from both \mathbf{E}^{\parallel} and \mathbf{E}^{\perp} and is given by:

$$I = C[PI^{\parallel} + (1 - P)I^{\perp}] \quad (2.11)$$

where C is a constant and P is the polarization factor. As the polarization factor is usually known as a characteristic of the synchrotron radiation and θ is also known from the experimental geometry, the bond orientation of a molecule adsorbed on a surface can be deduced.

More information is available in Reference [52–55].

X-ray Magnetic Circular Dichroism (XMCD)

As discussed above, x-ray absorption is an element-specific analysis method. The use of circularly polarized x-ray allows further access to the magnetic properties of the sample. Core electrons are excited in the absorption process into empty states above the Fermi energy and therefore probe the electronic and magnetic properties of the empty valence levels. The transition is governed by dipole selection rules. For $3d$ transition metals, the transitions in the following are allowed:

$$\begin{aligned} K : 1s &\rightarrow 4p_{1/2} \\ L_2 : 2p_{1/2} &\rightarrow 3d_{3/2}, 4s \\ L_3 : 2p_{3/2} &\rightarrow 3d_{3/2}, 3d_{5/2}, 4s \end{aligned}$$

Their magnetic properties are largely determined by the $3d$ shell configuration, which is best probed by L -edge absorption spectra, i.e., $2p$ to $3d$ transitions. The absorption of circularly polarized light by a magnetic atom is dependent on the orientation of both the light polarization and the spin polarization as explained in the following: photons transfer their angular momentum to electrons during photoelectron excitation. Right (R) circularly polarized light will excite electrons of one type of spin polarization and left (L) polarized light will excite electrons of the opposite spin polarization. Furthermore, since spin flips are forbidden in dipole transitions, spin-up photoelectrons can only be excited into spin-up empty states and spin-down photoelectrons into spin-down empty states. Thus, the spin-split final states act as a spin momentum detector for the polarization of the

photoelectrons and the absorption intensity is proportional to the number of available final states. In the case of L edge absorption, the L_2 and L_3 bands correspond to transitions of electrons of opposite spin polarization due to their opposite spin-orbit coupling ($l-s$ and $l+s$, respectively). If there is no net magnetization, the number of transition events corresponding to L_2 and L_3 levels are the same, despite the incident polarization, due to the equal number of spin-up and spin-down core electrons and the simultaneously equal number of up and down empty states. On the other hand, when a net spin moment exists, e.g., more spin-up electrons than spin-down electrons (or equivalently less spin-up holes than spin-down holes), the majority spin-up photoelectrons can only jump into the fewer spin-up empty states, and vice versa. This leads to the growth or incline of the L_2 and L_3 peak intensities in the XAS spectra. The use of oppositely polarized light defines that only electrons of one type of spin polarization can be excited at a time. By subtracting two XAS spectra recorded with left and right circular polarization, the resultant XMCD signal is proportional to the difference between majority and minority $3d$ empty states, i.e., the net spin moment. Similarly, the information on the orbital moment can be extracted from the XMCD spectra. If the empty d shell possesses an orbital moment, it will act as an orbital momentum detector for the excited photoelectron. By the summation of the L_2 ($l-s$) and L_3 ($l+s$) XMCD intensities, the spin moment is eliminated and the orbital moment information is revealed.

XMCD sum rules for the calculation of the values of the L , S and T operators projected to the x-ray incidence angle θ have been derived [58,59] :

$$\langle L_\theta \rangle = -2n_h \frac{\int_{L_3+L_2} (I_\theta^- - I_\theta^+) dE}{\int_{L_3+L_2} (I_\theta^- + I_\theta^+ + I_\theta^0) dE} \quad (2.12)$$

$$\langle S_\theta^{eff} \rangle = 2\langle S_\theta \rangle + 7\langle T_\theta \rangle = -n_h \frac{9 \int_{L_3} (I_\theta^- - I_\theta^+) dE - 6 \int_{L_3+L_2} (I_\theta^- - I_\theta^+) dE}{\int_{L_3+L_2} (I_\theta^- + I_\theta^+ + I_\theta^0) dE} \quad (2.13)$$

where n_h is the number of holes in the d -shell. The term $\langle T_\theta \rangle$ arises from the multipole expansion of the spin density. I^0 corresponds to the absorption intensity measured with linear polarization parallel to the x-ray incidence direction and is usually approximated as $I_\theta^0 = (I_\theta^+ + I_\theta^-)/2$.

More information on both experimental and theoretical aspects is available in References [58–62].

2.2 Experimental Set-up

All sample preparation and characterization presented in this thesis were performed *in-situ* under ultra-high vacuum (UHV) conditions, except the TCNQ powder samples prepared in atmosphere.

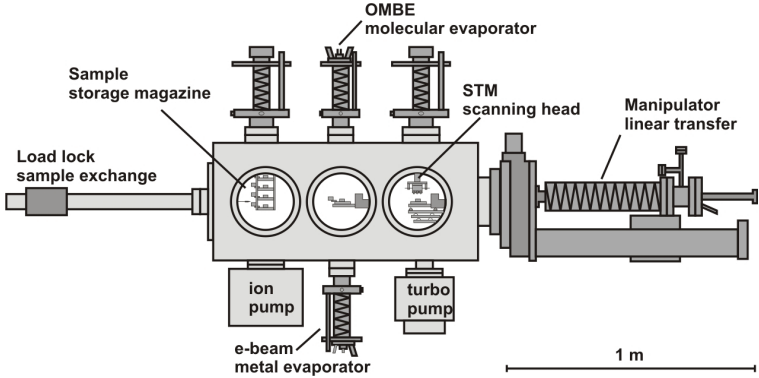


Figure 2.4: Schematic drawing of the UHV-STM system employed in this study. The base pressure is $\sim 5 \times 10^{-10}$ mbar. The UHV chamber is equipped with material evaporators enabling *in-situ* sample preparation. The sample holder is attached to the end of the manipulator, which can be transferred to required positions for sample preparation or characterization. The load lock system on the left side of the figure allows sample exchange without breaking the vacuum. Figure adapted from [63].

All STM measurements were done in a home-built variable temperature scanning tunneling microscope (STM) UHV chamber with a base pressure of $\sim 5 \times 10^{-10}$ mbar (Figure 2.4). The chamber is equipped with standard UHV tools, such as an ion gun to sputter-clean surfaces, a quadrupole mass spectrometer to monitor residual gases, and a load lock unit for sample exchange. Organic and metal evaporators are attached with gate valves allowing quick exchange of materials without breaking the vacuum. A sample storage magazine is installed which has a capacity of four samples. The sample holder is mounted on a movable manipulator and thus the sample can be transferred to required positions for cleaning, material deposition or sample exchange. The sample can be heated up to 1100 K by electron bombardment by a tungsten filament mounted below the sample

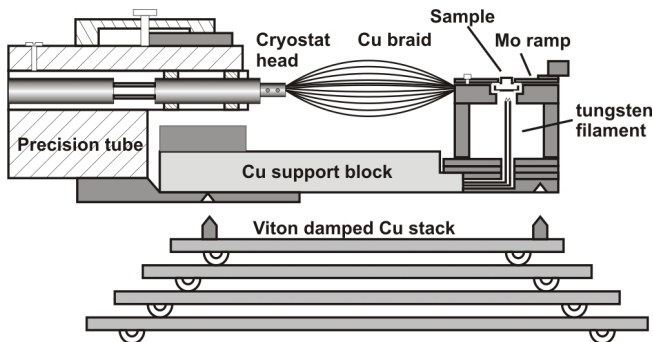


Figure 2.5: Schematic drawing of the sample holder of the UHV-STM system. Figure adapted from [63].

(Figure 2.5). The sample can be cooled down to 100 K by a helium flux cryostat connected by a Cu braid. During STM measurements, the sample holder is decoupled from the precision tube and rests on the viton-damped copper-stack and at the same time the whole UHV chamber is suspended from the ceiling.

All x-ray absorption measurements were carried out in similar UHV systems. XPS measurements were conducted at the Interface Analysis group of MPI Stuttgart, NEXAFS at the HE-SGM beamline of BESSY Berlin and XMCD at the ID-08 beamline of ESRF Grenoble.

XPS measurements were performed in a Kratos AXIS HSi 165 Ultra spectrometer with a monochromated Al K_{α} X-ray source (1486.6 eV) operated at a power of 150 W (15 kV and 10 mA). The spectrometer was calibrated by measuring a Ag crystal which has a characteristic peak in the Ag 3d region at 368.4 eV. The samples prepared for XPS measurements were characterized by low energy electron diffraction (LEED). Moreover, the coverage of adsorbates was determined by tracking the intensities of LEED spots. The C 1s XPS spectra were fitted by the Shirley background [50]. However, the N 1s spectra from the submonolayer TCNQ samples has a low signal which is superimposed on the sloping edge of the Cu L3VV and L2VV Auger peaks (kinetic energy 919 and 939 eV, and thus apparent binding energy 568 and 548 eV with Al K_{α} light source with a long tail to lower binding energy). Therefore, the N 1s spectra were analyzed by subtracting a clean Cu(100) surface spectrum to remove this sloping background. The peak fitting was then

done using 70% Gaussian and 30% Lorentzian characteristics.

All NEXAFS spectra were recorded in the total electron yield (TEY) mode with a light polarization factor $P = 0.8$ (see Equation 2.11). For the energy calibration, the photocurrent on a carbon-contaminated gold grid was recorded simultaneously with each spectrum. For the latter, a characteristic peak at 285 eV was used for energy alignment of all spectra. The NEXAFS raw data have to be appropriately processed before the spectra can be interpreted. First the spectra were normalized to a common value at the pre-edge. The spectra measured at the same angle were then averaged to increase the signal-to-noise ratio. Afterwards the spectra were normalized to the photon flux by dividing by the spectrum measured on a freshly sputtered Au wafer at corresponding incident angle. The resultant spectra can now be normalized again to a common pre-edge value to compare edge jumps. The edge jump is related to the coverage of molecules on the surface. Finally, the edge jump was normalized to the same value for all spectra to quantitatively compare the near-edge resonances according to the methods described in Section 2.1 and [52–55].

The XMCD measurements were conducted at the ID-08 beamline of the ESRF. The UHV chamber is composed of three parts: the preparation chamber, the STM chamber and the measurement chamber. The samples were characterized by STM before x-ray measurements. The XMCD spectra were recorded in the measurement chamber equipped with a cryomagnet operating at variable magnetic field between ± 5 Tesla and at variable temperature of 8-300 K. The magnetic field is colinear with the incident beam and the sample can be rotated for angular dependent XAS measurement. An evaporator can be mount for *in-situ* deposition. The XAS spectra were taken in the total electron yield (TEY) mode by measuring the drain current on the sample. The spectra have to be normalized to the incident photon flux, which is the photocurrent measured on a gold mesh positioned before the sample. The XMCD spectrum is the difference between the XAS spectra recorded at opposite helicity, i.e., right- and left-circularly polarized light.

2.3 Sample Preparation

In this study, single crystal Cu(100) and Ag(100) substrates were utilized. Both crystals are fcc (face-centered cubic) having the nearest atomic neighbors along the [011] direction (Figure 2.6). The nearest neighbor distances are 2.55 and 2.89 Å for Cu(100) and Ag(100), respectively. The samples were cleaned under UHV condition by repeated cycles of sequential Ar^+ sputtering and annealing. The Ar^+ beam was typically set to an en-

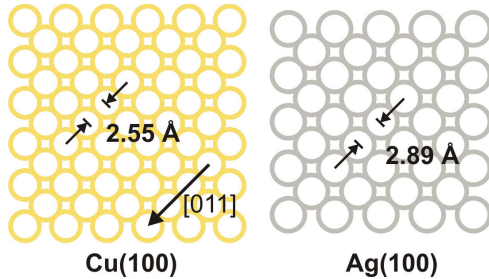


Figure 2.6: Schematic representations of the Cu(100) and Ag(100) surfaces utilized in this study.

ergy of 1 keV at an incident angle of 45° . The sputtering current detected on the sample was about $1.0 \mu\text{A}$. One cleaning cycle typically took 20 min of sputtering and 10 min of annealing at 800 K. After a few cycles of such cleaning procedures, atomically clean and flat surfaces were produced, showing terraces of ~ 100 nm width.

The organic TCNQ layers were prepared *in-situ* under UHV conditions. The TCNQ molecules (98%, Aldrich) were deposited by organic molecular beam epitaxy from a Knudsen cell evaporator at deposition rates of 0.01-0.1 ML/min with sublimation temperatures ranging from 370 to 400 K. One monolayer of TCNQ is defined as the surface fully covered by the flat-lying molecules. Metals of Mn, Fe, Co and Ni were utilized in this study. The metal atoms were always deposited after the TCNQ to limit the surface intermixing of metal atoms with the substrates. Metal atoms were evaporated using an e-beam heating evaporator (EFM3, Omicron). Both molecular and metallic materials were thoroughly degassed before use. Depending on the need of each experiment, the substrate was kept at low (160 K), room or elevated (up to 490 K) temperatures during TCNQ and metal deposition. The STM experiments on Cu(100) were performed by depositing both organic and metallic building blocks at Cu(100) held at 160 K to freeze out adsorbate diffusion and therefore avoid their aggregation. Metal-organic coordination occurred at subsequent annealing up to 470 K. On the other hand, the Ag(100) substrate was kept at elevated temperatures during metal deposition. The concept is similar that TCNQ molecules are very mobile at higher temperatures and uptake metal atoms arriving on the surface quickly to obtain uniform structures instead of clustering of metals.

Similar sample preparation procedures were used in the XPS and XMCD experiments

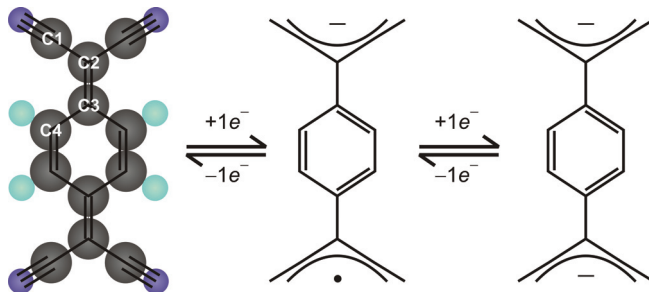


Figure 2.7: Chemical structure of TCNQ, $\text{TCNQ}^{\bullet-}$ and TCNQ^{2-} . In the neutral form the C2-C3 bond in TCNQ is double and the central ring is not aromatic. The uptake of at least one electron, however, aromatizes the central ring, changing C2-C3 bond from double to single and enhancing the conformational freedom of the molecule [44].

carried out at the Interface Analysis group of MPI Stuttgart and ESRF at Grenoble, respectively. Coordination structures were always characterized by either STM or LEED measurements. The NEXAFS measurements of molecular TCNQ from submonolayer to multilayer coverages were performed at BESSY in Berlin. TCNQ powder samples were simply tablets of TCNQ powder made in atmosphere and pumped in UHV for at least 5 hours. The pressure during measurements was below 5×10^{-9} mbar.

The chemical structure of TCNQ is outlined in Figure 2.7. The main features that determine TCNQ acceptor functionality are the four peripheral cyano groups and the central hexagonal ring. The four carbon atoms under different chemical environments are denoted from C1 to C4. In its neutral form the hexagonal ring is not aromatic and the molecular conformation is very rigid owing to the alternation of multiple and single bonds (p-quinoid character). The uptake of one electron, however, aromatizes the central hexagon ring (Fig. 2.7), which can only take place by changing the bond C2-C3 from double to single. The extra electron is thus accommodated in one of the peripheral nitrogen atoms, so that one of the molecular ends remains radical in character, whereas the other end loses the radicaloid character by accumulating one extra electron. Bond conjugation at the dicyanomethylene ends, however, remains, so that both the extra electron and the radical character are delocalized at each dicyanomethylene group.

The dianion form of TCNQ is also well known: in this case the second electron is

accommodated at the radicaloid dicyanomethylene end. In the anionic and dianionic forms, bond conjugation is restricted to the central ring and to the dicyanomethylene groups: the C2 carbon atom now has a higher sp^3 character and, consequently, the cyano groups are able to bend. The conformational freedom of $\text{TCNQ}^{\bullet-}$ and TCNQ^{2-} is thus much larger than that of neutral TCNQ. Charge transfer can therefore be expected to influence strongly the structure of the TCNQ/metal interface.

The molecular structure of TCNQ illustrated in Figure 2.7 is the unrelaxed geometry calculated for isolated molecules in gas phase [44]. The size of the neutral molecule along the long axis is 9.0 Å. Tentative models proposed in this thesis based on this simplified geometry have revealed much information about the structural formation, despite the molecular conformational change and substrate relaxation neglected. DFT calculation on the system of TCNQ/Cu(100) was carried out in collaboration with the groups of Prof. F. Martín and Prof. R. Miranda at Universidad Autónoma de Madrid, Spain. DFT calculation on the system of $\text{MnTCNQ}_2/\text{Cu}(100)$ was performed in collaboration with the group of Prof. M. A. Van Hove at City University of Hong Kong, China.

Chapter 3

Structure and Charge Transfer of TCNQ on Metal Surfaces

Organic heterostructures based on blends of molecules with electron-accepting (large electron affinity) and electron-donating (small ionization potential) characters display interesting electrical and optical properties with promising technological applications, such as organic light-emission diode (OLED), organic field effect transistor (OFET), solar cell, low molecular-weight conductor and organic magnet [36, 43, 64–69, 71]. These blends of molecules are deposited onto or placed in contact with metallic layers, and their performances thus depend crucially on both purely electronic factors (such as alignment of energy levels, electronic localization [72, 73] or electronic coupling between molecular orbitals and metal electronic states) and morphology (such as molecular nanostructure [74] and crystalline perfection [26]). Interfaces between organic species having either a donor or acceptor character and metal surfaces are thus of paramount importance for the performance of the devices described above. This observation has motivated great interests in understanding the electronic structure of metal/organic interfaces [75] and particularly the alignment of the energy levels at the interface related to the charge transfer between the organic donor or acceptor and the metallic surface [76–80]. Charge transfer, however, not only leads to modifications in the alignment of energy levels, but is usually also related to structural transformations in both donating and accepting species [81, 82]. Unfortunately, the role of the substrate in supramolecular organization at surfaces is often overlooked and is not well understood yet.

We describe here experiments and theoretical simulations that unequivocally demonstrate that, for strong charge transfer systems, both the molecules and the substrate un-

dergo strong structural rearrangements that determine molecular ordering. Such charge-transfer induced structural rearrangements at both sides of the metal/organic interface might have significant effects on the subsequent growth and structure of the organic film and, therefore, on device performance.

3.1 Charge Transfer-Induced TCNQ self-assembly on Cu(100)

TCNQ is one of the strongest organic electron acceptors and has long been regarded as a prime candidate for organic/inorganic charge transfer compounds [83, 84]. The interface between TCNQ and copper can thus be considered as a model system for the interfaces between the organic acceptors and the metallic contacts which are usually involved in OLEDs or organic solar cells. A combination of scanning tunnelling microscopy (STM), low-energy electron diffraction (LEED), x-ray photoelectron spectroscopy (XPS), near-edge x-ray absorption fine structure spectroscopy (NEXAFS) and density functional theory (DFT) calculations shows that the donation of about one electron from the substrate to the TCNQ molecules leads to a molecular conformation very similar to the well-documented structure of the anion or the dianion in solution. The conformation of the anionic molecule allows strong bonding between the nitrogen lone pairs and the substrate Cu atoms, so strong that the surface atoms bonded to the cyano groups are significantly lifted from their usual positions at the surface. Finally, the stress field associated with the local reconstruction mediates new adsorbate-adsorbate interactions and thereby results in a peculiar anisotropic growth for the self-assembled two-dimensional islands that could not have been predicted on the basis of the gas-phase conformation of TCNQ. Although some of these processes (charge transfer, adsorbate conformational changes, adsorbate-induced reconstructions) have been suggested to have a role in the self-assembly of organic acceptors on solid surfaces [81, 82, 85], the causal link among these processes could only be revealed by a powerful combination of complementary experimental and theoretical tools. Moreover, such a combination of techniques enables us to quantify the strength of this effect rather than just suggest its likelihood. This effect illustrates the important consequences that strong electronic interactions at the interface between organic donors or acceptors and metallic electrodes might have on the crystal structure of organic thin films contacted to them, and calls for further studies to characterize metal/organic interfaces for technological applications.

TCNQ adsorbs initially along the electron-rich step edges of the Cu(100) surface, as well as on the Cu(111) [86], but with the molecular long axis perpendicular to the step. Further growth proceeds from the steps in the form of two-dimensional compact islands with a well-defined rectangular shape (Figure 3.1), the longer side of which is perpendicular to the step. TCNQ molecules, both at step edges and in rectangular islands, appear as ellipsoids with an apparent size of $11 \text{ \AA} \times 6 \text{ \AA}$ and an apparent height of $\sim 1.3 \pm 0.3 \text{ \AA}$, which is consistent with an adsorption geometry in which the average molecular plane is parallel to the surface.

Figure 3.2 shows a close-up STM image of a TCNQ island and the LEED pattern for a TCNQ coverage close to one monolayer (ML) deposited on Cu(100). Clearly visible in the STM image of Figure 3.2 is the existence of a quasi-periodic array of one-dimensional dislocation lines in the molecular overlayer every three or four molecular rows as indicated by arrows. In the dislocation-free regions, our measurements are compatible with a structure commensurate with the Cu(100) lattice, with unit cell vectors given by $\mathbf{b}_1 = 4\mathbf{a}_1 + 3\mathbf{a}_2$ and $\mathbf{b}_2 = -2\mathbf{a}_1 + 2\mathbf{a}_2$ as depicted in Figure 3.1(b) (\mathbf{a}_1 and \mathbf{a}_2 being the surface lattice vectors along the close-packed directions). Across the dislocation lines (which run parallel to the \mathbf{b}_1 direction), the whole molecular row is shifted by one Cu(100) lattice parameter and the vector linking equivalent molecules across the dislocation line can be written as $\mathbf{b}'_2 = -2\mathbf{a}_1 + 3\mathbf{a}_2$. We have checked that the combination of these two structures (also taking into account the existence of four different domains) yields a LEED pattern in complete agreement with the experimental one (Figure 3.2). The molecules adsorb with their long axes orienting 19° from the substrate [011] direction. This orientation turns out to be a key factor for the self-assembly, which we will discuss later with the support of DFT calculations.

As mentioned above, the TCNQ islands grow in a manner elongated along the \mathbf{b}_1 direction. Statistical analysis of the self-assembled TCNQ island morphologies shows that the aspect ratio, that is, the ratio between the length of the long side of the island and the length of the short side of the island, is 4.3 ± 1.5 , corresponding to 2.4 ± 0.8 times more molecules along \mathbf{b}_1 than \mathbf{b}_2 . We conclude that the interaction linking the molecules along \mathbf{b}_1 must be larger than the interaction that holds the molecules together along \mathbf{b}_2 . This is a rather surprising conclusion if we consider the charge distribution of neighbouring TCNQ molecules placed at the experimentally determined distances.

Figure 3.1(b) presents electrostatic potential maps evaluated at a surface of constant charge density, with a color code that indicates the sign of the potential (red for negative

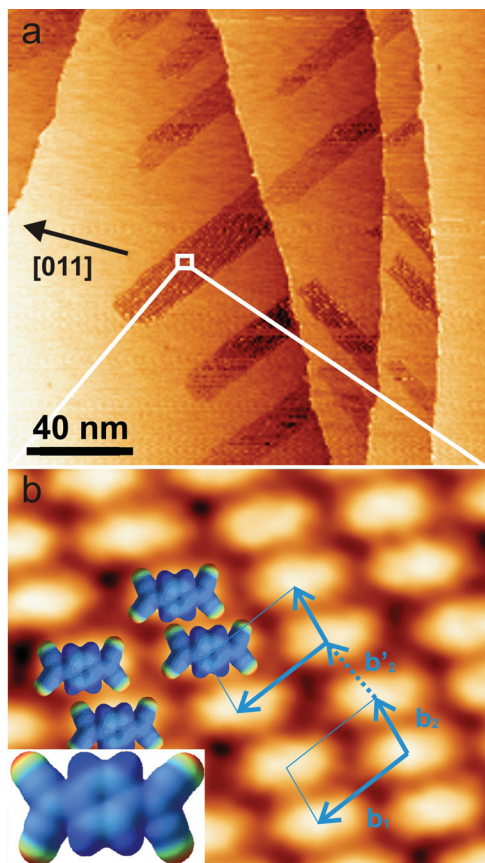


Figure 3.1: Elongated self-assembled islands of TCNQ on Cu(100). (a) Representative STM image ($80 \times 80 \text{ nm}^2$) showing the elongated TCNQ islands on Cu(100). (b) Details of the molecular arrangement. Constant charge density isosurfaces for TCNQ molecules calculated in the gas phase have been superimposed on the STM image. The projection of the electrostatic potential over the surface has been colour-coded onto it, in such a way that the red areas correspond to areas in which the electrostatic potential is negative and the blue-coded areas represent positive potential.

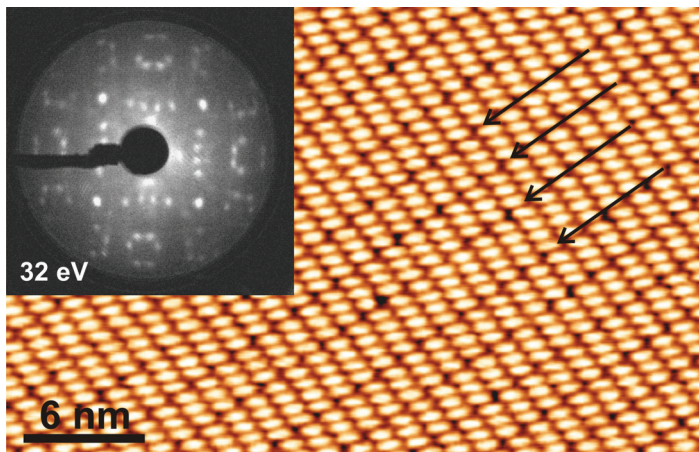


Figure 3.2: Highly ordered self-assembled monolayer of TCNQ on Cu(100). Some dislocation lines (described in the text) are marked by black arrows. Inset: LEED pattern recorded at 32 eV. The unit cell dimensions and symmetry as determined by STM are in good agreement with those obtained by LEED (see text).

and blue for positive). The isosurfaces have been calculated for neutral TCNQ molecules in the gas-phase conformation. Red-coded areas represent negatively charged areas, and blue-coded areas represent areas with a positive partial charge. These have been superimposed on the molecularly resolved STM image. Thus, the interaction along \mathbf{b}_2 can be ascribed to electrostatic interaction between the negatively charged cyano groups and positively charged hydrogen atoms of the central ring. This is the main bonding motif for self-assembled monolayers of TCNQ on the Au(111) surface [87]. On the other hand, the origin of the interaction along \mathbf{b}_1 remains unclear with this approximation, as it seems to bring together two negatively charged cyano groups.

XPS reveals the charge-transfer effects of TCNQ/Cu(100) by comparing the core level shifts with neutral TCNQ (see Figure 3.3). The N 1s spectrum of the TCNQ powder sample (top of Figure 3.3(a)) shows a prominent peak at 399.6 eV and a shake-up feature at 2.4 eV higher binding energy. On the other hand, the spectrum of TCNQ powder over the C 1s region (top of Figure 3.3(b)) is naturally more complex because carbon atoms in TCNQ are present in four different chemical environments (denoted by

C1 to C4 in Fig. 2.7). Three components of the C 1s resonance are identified to be at 289.3, 286.8 and 285.4 eV. The position of the peak at the highest binding energy (289.3 eV) is 2.5 eV above the peak at 286.8 eV, which correlates with the 2.4 eV energy difference observed in the N 1s region between the shake-up and the main peak. Therefore, the 289.3 eV peak is assigned to be the shake-up resonance of the C 1s region. Furthermore, it has been reported in charge distribution calculations that the carbon atoms in a TCNQ molecule fall into two groups, i.e., the positively charged (C1 and C2) in the allyl-like C1-C2-C1 part and the negatively charged at the central ring (C3 and C4) (cf. Figure 2.7) [88]. XPS measurement is sensitive to the atomic charge state and generally the binding energy of electrons is higher if the atom is more positively charged. Thus, it is reasonable to assign the other two peaks at 286.8 and 285.4 eV to the positively charged C1-C2-C1 part and the negatively charged quinoid ring, respectively. Both N 1s and C 1s spectra agree well with neutral TCNQ reported in literature [89–94]. The intensities of the C 1s 286.8 and 285.4 eV peaks are expected to be similar due to the equal number of carbon atoms in the C1-C2-C1 part and in the quinoid ring. However, for the powder sample, carbon contamination from atmosphere cannot be excluded and thus very likely results in the unequal peak intensities of the 286.8 and 285.4 eV peaks. Furthermore, the peak width of the powder sample is larger than that of the submonolayer sample, which can be explained by electron scattering induced by the nonuniform surface morphology of the powder sample.

The N 1s spectrum of 1 ML TCNQ adsorbed on Cu(100) is characterized by a single prominent peak at 398.7 eV (middle of Figure 3.3(a)) and a shake-up at 400.1 eV. The peak positions are consistent with previous reports for TCNQ anion-containing compounds, e.g., LiTCNQ, KTCNQ, NiTCNQ₂ and CuTCNQ, and is a clear indication of charge transfer from Cu to TCNQ [89–92, 94–97]. In addition to the charge state of TCNQ, the 398.7 eV peak has been reported in related systems to be a signature of cyano groups interacting with substrates via the π -orbital located on the triple bonds [106, 107]. Thus, the contribution of the π bonding at the CN triple bonds can not be excluded in the adsorption of TCNQ on Cu(100). The participation of the CN triple bond will be discussed later in the NEXAFS section. The C 1s XPS lineshape of the 1 ML TCNQ/Cu(100) is similar to the powder sample, apart from a substantial energy shift to the lower binding energy (middle of Figure 3.3(b)). A shake-up feature at 287.2 eV and two main resonances at 285.7 and 284.6 eV are identified. All the three peaks show a shift to the lower binding energy compared with those of neutral TCNQ. The separation between the shake-up and

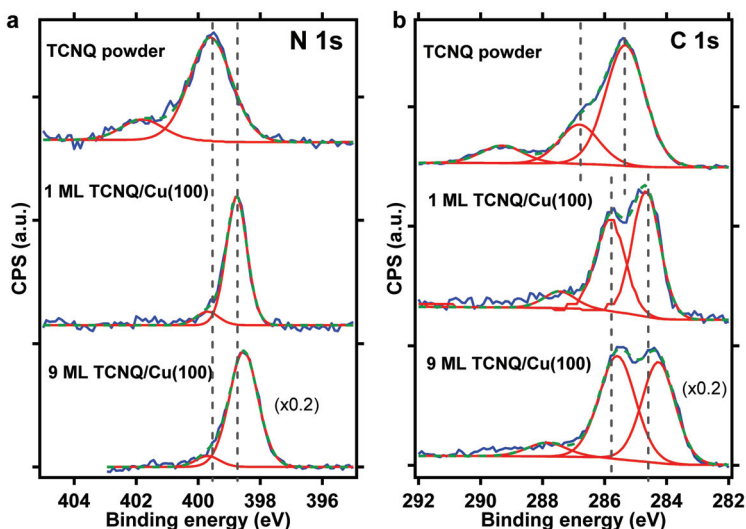


Figure 3.3: XPS spectra of (a) nitrogen 1s and (b) carbon 1s core levels for TCNQ/Cu(100) and a bulk sample (powder) of TCNQ. The spectra show raw experimental data (blue), the fit to the experimental data (green) and the decomposition of the fit into their individual components (red). In each spectrum, a high energy shoulder is visible, being the molecular "shake-up" peak. On adsorption at the Cu(100) surface, both the nitrogen and carbon 1s core level of the TCNQ shift to lower binding energies, indicative of electron transfer from the copper substrate to the TCNQ in both submonolayer and multilayer coverages.

the first main peak is 1.5 eV, which corresponds to that observed in the N 1s region of charged TCNQ. In accordance with the peak assignment of the C 1s resonances of TCNQ powder, the 285.7 eV peak is then linked to the C1-C2-C1 part of TCNQ and the 284.6 eV peak to the central ring. The 284.6 eV peak is a characteristic feature of molecules containing benzene rings [108, 109]. Thus, the energy shift from 285.4 to 284.6 eV evidences the aromatization of TCNQ quinoid rings upon charge transfer. This charge transfer is probably responsible for the observed increase of the work function by 0.6 eV on completion of the monolayer in the related fluorinated TCNQ adsorbed on Cu(111). As shown in Figure 2.7, the aromatization of the quinoid ring requires the weakening the

C2-C3 bond from double to single. Consequently, TCNQ gains conformational freedom, which might explain the seemingly unfavourable interaction shown in Figure 3.1(b) (see the discussion below).

Another interesting phenomenon is exhibited by the XPS spectra of the multilayer TCNQ on Cu(100) (bottom of Figure 3.3). Both the N 1s and C 1s spectra of multilayer TCNQ resemble those of the submonolayer sample except an intensity scaling up and an increase in the peak width. The N 1s spectrum is fitted by a single peak of larger width at a slightly shifted position of 398.5 eV. The components of the C 1s spectrum show similar trends. The wider peak can be explained by the disordered surface morphology and the small energy shift can be reasonably attributed to the modified atomic environment due to different molecule packing in the multilayer. It is rather surprising that the TCNQ multilayer is negatively charged even though the molecules in the topmost layers are not in direct contact with the Cu(100) substrate. The XPS spectra taken after annealing at 400 K for 10 min do not exhibit noticeable changes, indicating neither desorption nor chemical reaction takes place. Deposition of Cu atoms on top of the TCNQ multilayer neither induces changes in the XPS spectra. Thus, it can be inferred that TCNQ interacts so strongly with the Cu(100) substrate that the Cu atoms are pulled out of the substrate and diffuse into the TCNQ multilayer. This conclusion is supported by previous reports on the fabrication of Cu-TCNQ nanowires and films where solid diffusion of Cu into TCNQ is shown [98–100]. This phenomenon contrasts that of TCNQ multilayer adsorbed on Ag(100) which will be discussed in the following (Section 3.2) or TCNQ adsorbed on Ni(111) [92].

To understand the conformation and bonding geometry of TCNQ on the Cu(100) surface, an angle-resolved NEXAFS study was performed at the Berliner Elektronen-Speicherring Gesellschaft für Synchrotronstrahlung (BESSY). The spectra, shown in Figure 3.4, were normalized and fitted according to standard procedures for NEXAFS analysis described in Chapter 2 and References [52–55]. In Figure 3.4(a), the nitrogen 1s NEXAFS spectra of TCNQ powder and 1 ML TCNQ/Cu(100) are shown. In comparison with previous works, peak 1 is attributed to the LUMO localized at the cyano groups, peak 2 also to the cyano groups and peak 3 to a delocalized orbital over the molecule [110–112]. In agreement with our XPS results, we interpret the absence of resonance 1 on adsorption as the result of charge-transfer populating the LUMO orbital and aromatizing the central quinoid ring. Resonance 2 contains the two orthogonal π^* -orbitals localized on the CN group, which lie close in energy for neutral molecules. On adsorption, the degenerate

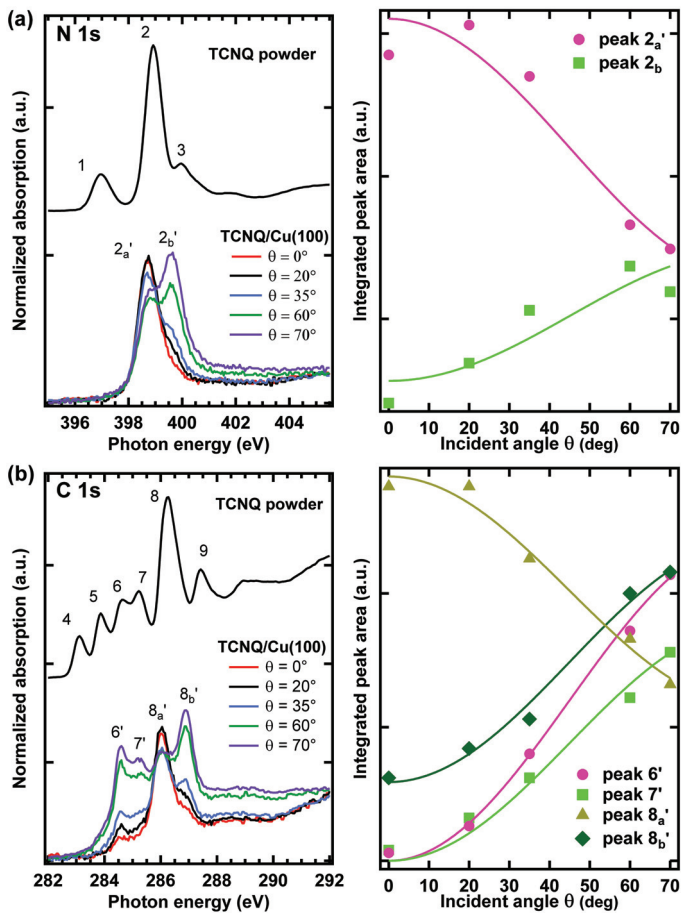


Figure 3.4: NEXAFS measurements of (a) N 1s and (b) C 1s spectra of TCNQ/Cu(100) and a powder sample of TCNQ. The absence of peak 1, 4 and 5 is an indication of charge transfer from copper to TCNQ. The right panels show the peak intensity versus incident beam angle θ . Best fits to these trends indicate a flat-lying central ring and tilting cyano groups by $15.7\text{--}32.8^\circ$ of TCNQ.

π^* -orbitals split and as a result we observe the separation of peak 2 into peaks $2'_a$ and $2'_b$. The separation of the peaks $2'_a$ and $2'_b$ amounts to 0.9 eV. Such orbital splitting has been observed in related systems [57, 110, 113] and occurs due to the interaction of CN bonds to the substrate, which is consistent with the association of the 398.7 eV peak in the N 1s XPS spectrum to the π -bonding of CN groups to Cu(100). The C 1s NEXAFS spectra, shown in Figure 3.4(b), can be interpreted in the same way as the N 1s spectra. The disappearance of resonances 4 and 5 upon adsorption indicates the charge transfer from Cu(100) to TCNQ. Resonances 6 and 7 assigned to the central ring of TCNQ stay unchanged in energy. In the mean time, a similar peak splitting of peak 8 into $8'_a$ and $8'_b$ by 0.8 eV again indicates the interaction of CN groups to the Cu(100) substrate. The bonding angle of TCNQ can be determined by analyzing the dependence of peak intensity with x-ray incidence angle as shown in the right panels of Figure 3.4. The direction of the incident beam is characterized by the angle θ between the beam and the surface normal. The integral of peaks are plotted together with regression curves according to Equation 2.11. We can thus calculate the bonding angle of TCNQ on Cu(100), that is the angle between the surface and the vector along the bond. We obtain 0° (0° , 28.5° , 32.8° , 25.3° , 15.7°) for peak $6'$ ($7'$, $8'_a$, $8'_b$, $2'_a$, $2'_b$). Note that, on adsorption peaks 3 and 9 might overlap with $2'_b$ and $8'_b$, respectively, and become indistinguishable. This might lead to some inaccuracy in the determination of bond angles, but nevertheless we can conclude that TCNQ adsorbs on Cu(100) with the central ring (peaks $6'$ and $7'$) flat-lying and the CN groups (peaks $8'_a$, $8'_b$, $2'_a$ and $2'_b$) tilted towards the surface by 15.7 - 32.8° . This bent conformation of TCNQ should still allow appreciable overlapping of the CN π orbitals to the substrate and is supported by DFT calculations, which we will discuss in the following.

To shed light on the interaction that holds the islands together along the \mathbf{b}_1 direction, we carried out DFT calculations for both isolated molecules adsorbed on Cu(100) and the complete overlayer (in this case with the experimentally obtained unit cell vectors). The optimized geometry for the adsorbed TCNQ is shown in Figure 3.5. This geometry corresponds to the minimum of all the configurations explored for the single molecule adsorbed on Cu(100). The calculated binding energy is 2.23 eV, indicating a rather strong chemisorption. The calculated binding energy for the complete overlayer is slightly larger, 2.35 eV per molecule, indicating further stabilization of the system owing to the particular organization of the overlayer. The orientation of the molecule with respect to the substrate [011] direction is found to be 19° (shown in Figure 3.5(c)), which agrees well with the one observed in the STM images. This adsorption orientation renders the cyano groups lying

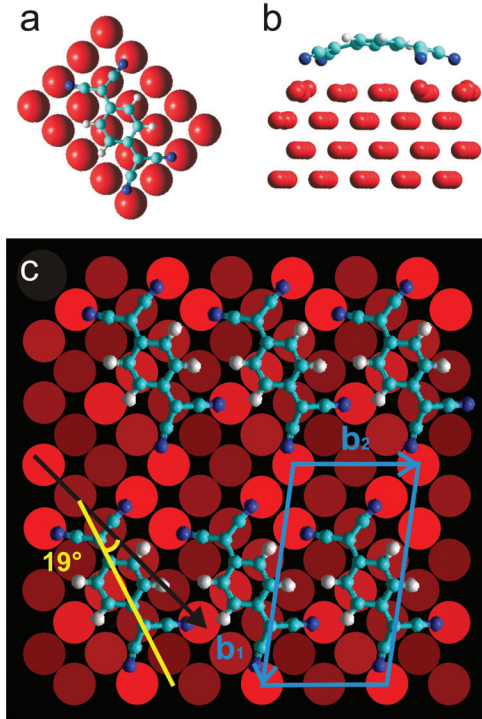


Figure 3.5: Structural rearrangements at both sides of the TCNQ/Cu(100) interface from DFT calculations. (a) Top and (b) side views of the calculated relaxed conformation for a single TCNQ molecule adsorbed on Cu(100) (where light blue corresponds to carbon atoms, dark blue corresponds to nitrogen atoms, red corresponds to the copper atoms of the substrate and white corresponds to hydrogen atoms). Bending of the C2-C3 bond and surface reconstruction are clearly observed. (c) Top view of the calculated relaxed conformation for the self-assembled TCNQ monolayer. Different shades of red of the copper atoms represent different distances between the copper atom and the unperturbed, unreconstructed equilibrium position (the brightest red shade corresponds to copper atoms separated by 0.22 Å above their equilibrium positions, whereas the darkest shade corresponds to copper atoms placed 0.16 Å below the equilibrium position). Reconstructed atoms act as a glue to link molecular rows along \mathbf{b}_1 .

close to the top positions of the Cu(100) surface. Interestingly, the conformation of the TCNQ molecule is not planar, consistent with our NEXAFS analysis. The C2-C3 bonds bend so that the cyano groups point towards the surface, or more specifically towards the top positions of the surface. The bending of the C2-C3 bond is energetically very costly unless the conjugation of double and single bonds associated with the neutral form of TCNQ is removed by the uptake of at least one electron from the surface (see Figure 2.7). A theoretical estimation based on a Bader analysis of the charge density yields a charge transfer from the Cu(100) surface to the TCNQ adsorbate of 1.5 e^- per TCNQ, in qualitative agreement with the XPS results shown in Figure 3.3. Such a bent geometry has already been described for the related F_4TCNQ species adsorbed on a Cu(111) surface, and was also attributed to charge transfer from the surface [81]. In contrast, adsorption of TCNQ on Au(111), a surface for which the charge transfer is expected to be much lower, owing to its larger work function and overall reduced reactivity, does not result in a bent conformation of the adsorbate [87].

The bending of the cyano groups towards the surface enables a rather strong chemical interaction between the lone pairs of the nitrogen atoms and the d_z orbitals of Cu atoms in the substrate. Such strong interactions lead to a high adsorption energy and, more importantly, to a rearrangement of the copper surface atoms bonded to the cyano groups. As can be seen in Figure 3.5(b), these copper atoms are lifted from their equilibrium positions by about 0.22 \AA . A similar surface reconstruction has been theoretically and experimentally observed for the adsorption of the related TCNE molecule on Cu(100) [82, 85]. The rearrangement of these copper atoms creates a stress field in such a way that the energy cost to lift a second atom out of its unperturbed equilibrium position is significantly reduced for the immediate neighbours of the already reconstructed copper atom bonded to the cyano group. Figure 3.5(c) shows a top view of the calculated relaxed geometry for a self-assembled TCNQ overlayer on Cu(100). The out-of-plane position of the copper atoms has been colour-coded in different shades of red, in such a way that lighter shades of red indicate atoms protruding farther out from the surface. A close inspection of the spatial distribution of such reconstructed atoms reveals that they are mainly located at the bonding positions of the cyano groups in the TCNQ molecules, which are optimized by the TCNQ adsorption orientation. The stress field around the reconstructed atoms makes it energetically favourable for copper atoms attached to cyano groups of different molecules to be in close proximity, and therefore has a profound effect on the self-ordering of TCNQ islands. In the present case, reconstructed copper atoms

are tightly grouped along the \mathbf{b}_1 direction of the TCNQ layer. We can thus conclude that the bonding between the nitrogen lone pairs and the substrate Cu atoms is the major coordination interaction which governs the TCNQ self-assembly. This strong N-Cu bonding is enabled by the conformational freedom that TCNQ gains upon charge transfer from the Cu(100) substrate. The substrate rearrangement induced by this strong N-Cu bonding consequently results in a significant attractive interaction along the \mathbf{b}_1 domain orientation and an anisotropic growth of elongated rectangular TCNQ islands. Although substrate-mediated elastic interactions have been invoked before to explain the ordering of several nanostructures on solid surfaces, for example, copper-oxygen islands formed on partial oxidation of the Cu(110) surface, the distance range in which they have a significant role is usually one order of magnitude larger than the one described here [114–116].

The results shown here exemplify the fundamental role that charge-transfer processes across metal/organic interfaces have on molecular self-assembly and subsequent crystal growth. Such charge transfers modify the energy level alignment, but they also affect molecular conformation and, thereby, molecular self-assembly. For example, they are usually related to the existence of strong bonding between surface and adsorbate, and in such situations the static-surface approximation is no longer applicable: substrate reconstruction and surface-mediated interactions must be explicitly taken into account, and gas-phase expectations based on intermolecular interactions are not likely to work. These arguments prompt further studies to properly address the relation between electronic interactions and geometrical structures in metal/organic interfaces. For example, comparison with molecules containing cyano groups but not having such a strong accepting character, or with strong organic acceptors not containing cyano groups, will further clarify the interplay between charge transfer and chemical bonding across the interface.

3.2 TCNQ self-assembly on Ag(100)

TCNQ molecules are mobile on Ag(100) at room temperature as indicated by the fuzziness of the bare substrate in STM images such as Figure 3.6(a). Well-ordered molecular domains are only observed when the coverage is close to one monolayer. Besides step edge decoration TCNQ forms single big domains extending over entire terraces. Figure 3.6(a) shows that the molecular phase has a rhombic unit cell. The orientation of the two mirror-symmetric domains, parallel to the shorter edge of the unit cell, are indicated by blue arrows in Figure 3.6(a). The in-plane 90°-rotated domains are observed elsewhere

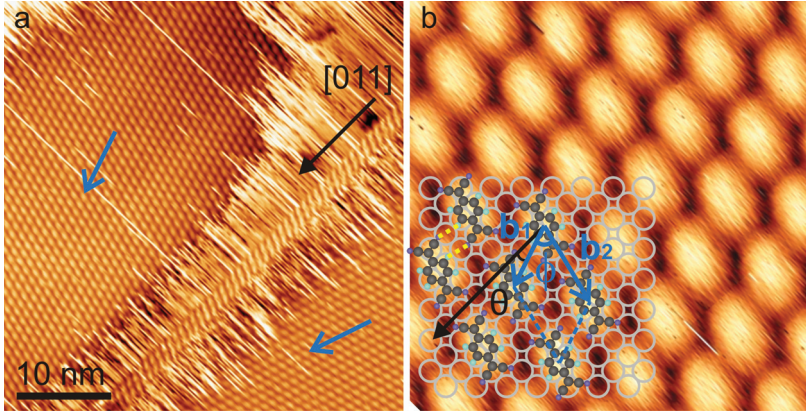


Figure 3.6: STM images of the TCNQ adlayer on Ag(100). (a) TCNQ molecules self-assemble into an ordered rhombic structure when the coverage is close to 1 ML. Mirror-symmetric domains with the unit cell vectors $\mathbf{b}_1 \pm 18.7^\circ$ to substrate [011] direction are indicated by blue arrows. The fuzziness of the image indicates the mobility of TCNQ on Ag(100). (b) The rhombic superstructure is marked by \mathbf{b}_1 and \mathbf{b}_2 unit cell vectors. The unit cell parameters of the model, $|\mathbf{b}_1| = 9.1 \text{ \AA}$, $|\mathbf{b}_2| = 11.9 \text{ \AA}$, $\phi = 57.5^\circ$, and $\theta = 18.4^\circ$, match well with the measured values from STM data.

and attributed to the fourfold substrate symmetry. In the high resolution STM image (Figure 3.6(b)) individual molecules are imaged as oval protrusions with an apparent size of $6.2 \text{ \AA} \times 8.9 \text{ \AA}$. The detail analysis of the STM data yields the unit cell parameters $|\mathbf{b}_1| = 9.2 \pm 0.2 \text{ \AA}$, $|\mathbf{b}_2| = 12.0 \pm 0.4 \text{ \AA}$, $\phi = 56.8 \pm 1.9^\circ$, and the domain orientation $\theta = 18.7 \pm 1.4^\circ$ (see Figure 3.6(b)), consistent with a commensurate $(3, 1/1, 4)$ superstructure with respect to the surface lattice vectors along the close-packed directions. A tentative model is depicted on top of Figure 3.6(b) with the unit cell indicated. Similar to the molecular phase on Cu(100) (Section 3.1), the molecules adsorb with the nitrogen atoms close to the top sites of the Ag(100) substrate. The molecular long axes orient approximately 19° from the substrate [011] direction, leading to non-equivalent binding sites of the cyano groups on the surface. The closest distance between the hydrogen atoms at a neighboring molecule and the nitrogen of the cyano groups amounts to about 3.0 \AA as indicated by yellow dotted lines in the model. This length is comparatively too long to be a hydrogen

bond. Therefore, we assume that hydrogen bonding does not account for the packing of the molecules and presumably an electrostatic attraction similar to the one on the Cu(100) dominates the intermolecular interaction along the \mathbf{b}_1 direction. No stable domains were observed at submonolayer coverage, which is in contrast to the TCNQ adsorption on Cu(100). We ascribe this behavior to the stronger adsorbate-substrate coupling on the copper surface which is accompanied by strong relaxations at the metal surface.

To gain insight into the bonding mechanism of TCNQ on Ag(100), angle-resolved NEXAFS measurements were carried out at the Berliner Elektronen-Speicherring Gesellschaft für Synchrotronstrahlung (BESSY). The spectra, shown in Figure 3.7, were normalized and fitted according to standard procedures for NEXAFS analysis (see Section 2.1 and Reference [52–55]). The nitrogen 1s and carbon 1s NEXAFS spectra of 0.8 ML TCNQ/Ag(100), together with those of TCNQ powder, are plotted in Figure 3.7(a) and (b), respectively. The N 1s and C 1s lineshapes of TCNQ on Ag(100) have strong resemblance to those on Cu(100) (see Figure 3.4), which implies a similar bonding configuration of TCNQ on both substrates despite the very different substrate coupling evidenced by the TCNQ mobility. First of all, the absence of peaks 1, 4 and 5 on adsorption discloses the charge transfer from Ag(100) populating the LUMO of TCNQ. The splitting of resonance 2 into peaks $2'_a$ and $2'_b$ in the N 1s NEXAFS spectra is explained by the energy separation of the two orthogonal π^* -orbitals on the CN group due to the interaction of CN groups to the Ag(100) substrate. A similar phenomenon is observed in the C 1s region by the splitting of peak 8 into $8'_a$ and $8'_b$. The energy difference between peaks $2'_a$ and $2'_b$ on Ag(100) amounts to 0.8 eV, which is similar to the 0.9 eV observed on Cu(100), and the splitting of peak 8 is 0.8 eV on either substrate. Both the absence of LUMO resonances and the splitting of molecular orbitals represent the non-vanishing substrate interaction on Ag(100), which can not be predicted from the surface mobility of TCNQ. However, with our experimental resolution, the difference in the bonding strength can not be determined yet from the peak splitting observed in the NEXAFS measurements.

The concave geometry of TCNQ induced by charge transfer (see Figure 3.5) is shown to be major in the coordination of TCNQ on Cu(100) by facilitating the bonding of the nitrogen lone pairs to the d_z orbitals of the substrate. Here a similar charge transfer to TCNQ is revealed by the NEXAFS lineshape. In addition to the information on the electronic structure of TCNQ molecules, NEXAFS can also reveal information about their orientation. The conformational change of TCNQ is examined by analyzing the angular dependence of NEXAFS resonances as shown on the right panels of Figure 3.7. Similar

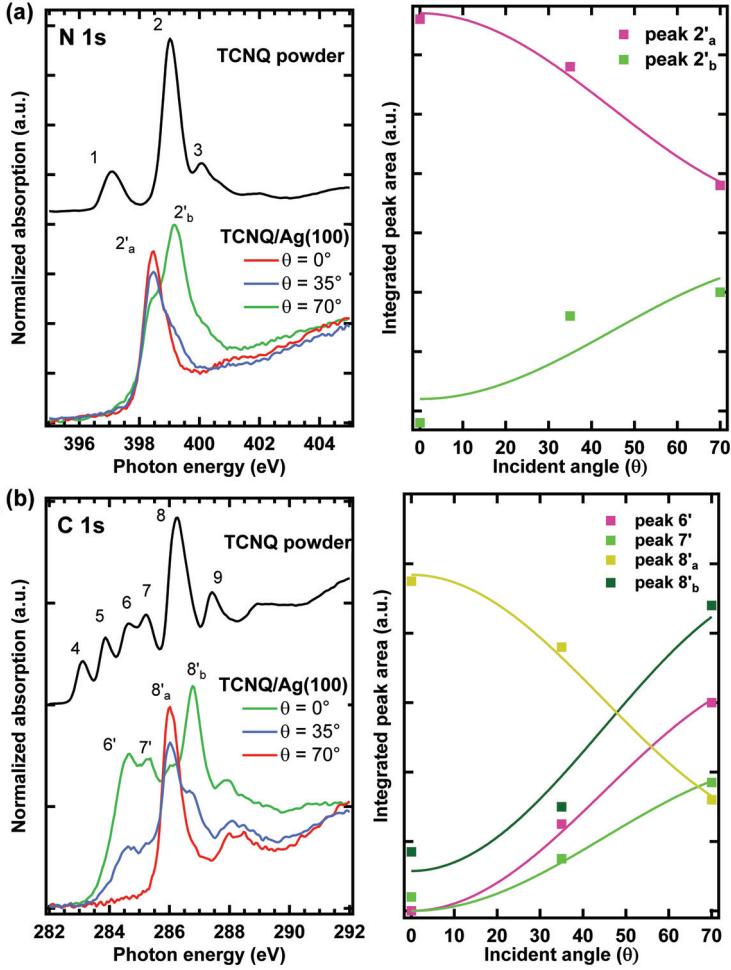


Figure 3.7: NEXAFS measurements of (a) N 1s and (b) C 1s spectra of TCNQ/Ag(100). The right panels show the peak intensity versus incident beam angle θ . Best fits to these trends yield bonding angle of 0° (0° , 14.9° , 24.1° , 29.2° , 16.9°) for peak 6' (7', 8'_a, 8'_b, 2'_a, 2'_b).

to the Cu(100) case, the peaks 6' and 7' represent the central ring of TCNQ while $8'_a$, $8'_b$, $2'_a$ and $2'_b$ are attributed to the cyano groups. The integral of resonances are plotted versus the angle between the incident beam and the surface normal (θ). Best fits to the trends according to Equation 2.11 are shown by the regression curves. The bond orientation, which is the angle between the bond and the surface, is thus obtained to be 0° (0° , 14.9° , 24.1° , 29.2° , 16.9°) for peak 6' ($7'$, $8'_a$, $8'_b$, $2'_a$, $2'_b$). The result exhibits a flat-lying central ring and tilted cyano bonds in accordance with the conformation of charged TCNQ. Therefore, it can be presumed that TCNQ molecules coordinate through the nitrogen lone pairs to the Ag(100) substrate although the strength of this bonding is not sufficient to immobilize them on Ag(100).

A careful inspection of the NEXAFS spectra of TCNQ molecules at different coverages on Ag(100) reveals some delicate information on the adsorption of TCNQ. Figure 3.8 shows the N 1s and C 1s NEXAFS spectra measured at grazing incidence of 0.5 to 1.5 ML TCNQ, together with those of the 1.5 ML TCNQ/Ag(100) sample after annealing at 400 K for 1 min. The preparation of the 1.5 ML TCNQ/Ag(100) sample requires a cooling of the substrate to 200 K in order to increase the sticking coefficient of molecules. In contrast to the Cu(100) case where multilayer sample can be prepared at room temperature, this requirement of low substrate temperature already implies the different bonding strength provided by Ag(100) from Cu(100). From 0.5 to 1 ML coverage, both the N 1s and C 1s NEXAFS spectra of TCNQ/Ag(100) show simply a continuous increase in the intensity without apparent change in the lineshape. The N 1s spectra contain the $2'_a$ and $2'_b$ peaks which reveal the interaction of cyano groups to the substrate as discussed in Figure 3.7. Similarly, the C 1s lineshape indicates the charge transfer to TCNQ and the substrate interaction by the peaks 6', 7', $8'_a$ and $8'_b$. At 1.5 ML, however, the N 1s and C 1s spectra exhibit strong characteristics of neutral TCNQ by the appearance of the previously occupied LUMO peaks 1, 4 and 5. The emergence of the resonances $2'_a$ and $2'_b$ into the single peak 2, or $8'_a$ and $8'_b$ into 8, further indicates that molecules in the second monolayer do not undergo substrate coordination interaction. This phenomenon is strikingly different from the substrate interaction discussed already on Cu(100) where charge transfer persists in thick multilayers (see Figure 3.3 and the discussion in the text). As the charge transfer is ascribed to the Cu atoms mixing into the TCNQ multilayer on Cu(100), we can rationally infer that Ag atoms do not diffuse out of the Ag(100) substrate. Therefore, only the first monolayer of TCNQ which is in direct contact with the Ag(100) substrate undergoes charge transfer and metal coordination. We performed annealing treatment to

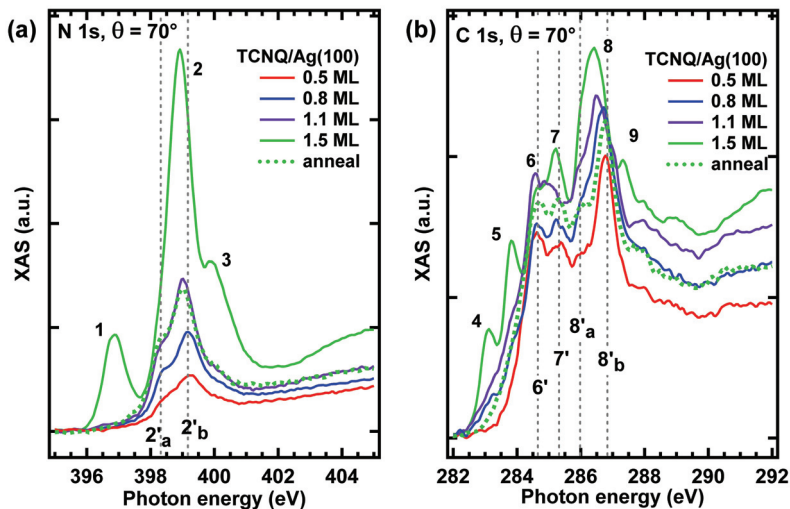


Figure 3.8: (a) N 1s and (b) C 1s NEXAFS spectra for various coverages of TCNQ on Ag(100). At submonolayer coverages, TCNQ molecules obtain charge from the substrate and the NEXAFS lineshape indicate coordination of the cyano groups to the substrate by the splitting of peaks 2 and 8. In contrast, the 1.5 ML TCNQ exhibits the existence of neutral molecules intact from substrate coordination. After annealing at 400 K for 1 min, the intensity and lineshape of the spectra indicate that TCNQ molecules in the second monolayer desorb and a monolayer of TCNQ is left on the surface.

elucidate the role of Ag atoms. The spectra taken after annealing the 1.5 ML sample at 400 K for 1 min are plotted in Figure 3.8. Both the N 1s and C 1s spectra show reduced intensity which is estimated to correspond to about 1 ML coverage. Thus, we infer that TCNQ molecules above the second monolayer are weakly physisorbed without considerable chemical bonding. These molecules desorb readily at 400 K while this temperature is not sufficient to remove the multilayer adsorbed on Cu(100) (Figure 3.3). The lineshape also indicates that the first monolayer of TCNQ, which is charged and coordinated with the Ag(100) substrate, is left after annealing by showing the splitting of peak 2 and 8 and the absence of peak 1, 4 and 5. This observation is rather unexpected since Ag diffusion

in TCNQ film has been reported [100]. However, we attribute the difference to the unique property of single crystal Ag(100) surfaces.

3.3 Summary and Comparison

The drastic difference of the TCNQ surface mobility exemplifies the distinct chemical nature of Cu(100) and Ag(100) surfaces. On Cu(100), the charge-transfer induced bending of TCNQ anion facilitates the bonding of TCNQ molecules to surface Cu atoms via nitrogen lone pairs on the cyano groups. In turn, Cu atoms are lifted from their unperturbed position to attain energy equilibrium. Such reconstruction of the Cu(100) surface creates favorable sites for other TCNQ molecules to arrange around and consequently well-ordered domains form. The CN triple bond hybridization also contributes to the adsorption of TCNQ on Cu(100), evidenced by the π^* -orbital splitting in the NEXAFS analysis. In this case the substrate strongly affects the domain growth. On Ag(100), even though surface coupling is apparently reduced, substrate interaction still leads to specific growth directions, which is a composite result of lattice match and molecule-molecule lateral interaction. The charge transfer from Ag(100) to TCNQ, and the concomitant bending of molecule conformation, indicates a cyano-Ag coordination mechanism similar to that on Cu(100), i.e., through the nitrogen lone pairs. The NEXAFS data show considerable π^* -orbital splitting, which signifies the participation of the CN triple bond interaction with the Ag(100). Despite the similarities in the bonding mechanism and charge transfer effects of submonolayer TCNQ on the different substrates, the adsorption of the multilayer exhibits great differences. TCNQ multilayer on Cu(100) undergoes charge transfer, attributed to Cu diffusion into the multilayer, while on Ag(100) the multilayer behaves like neutral non-reacting molecules. The influence of the chemical environment to the supramolecular ordering will be further amplified in the growth phenomena of metal coordination structures in the next chapter.

Chapter 4

Metal-TCNQ Coordination Structures on Metal Surfaces

Metal-ligand coordination interactions are generally more rigid and directional than hydrogen bonds and therefore are employed to supramolecular systems in order to synthesize more robust structures. The resultant metal-organic structures combine the properties of their constituents and are characterized by higher structural stability and complexity. General design principles follow the coordination chemistry of metal ions having specific coordination geometry (tetrahedral, square-planar, octahedral, etc.) and the choice of molecules representing adequate functional groups. This has yielded supramolecular compounds in solution with tailor-made properties [2, 6–10]. However, the rules of coordination chemistry in solution has to be modified to appropriately describe the phenomena occurring on surfaces [26]. For example the coordination geometry of the metal atoms changes due to the spatial confinement on surfaces. The two-dimensional confinement might impose chiral properties on the surface structures. And, most crucially, the substrate actively influences the adsorbates from geometrical arrangements to chemical modifications.

The study in TCNQ-based surface nanostructures is initiated by the rich electronic and magnetic properties of this group of materials synthesized by solution supramolecular chemistry [35, 118, 119]. As reported in literature, many factors can influence the properties of M-TCNQ compounds, for example, structure, stoichiometry, synthesis routes, etc. Due to the lack of long-range structural ordering in bulk crystals, the accurate interpretation of physical properties has been difficult. We take advantage of the powerful STM technique to study how building blocks coordinate with one another on surfaces. In

this chapter the emphasis lies in the thermodynamically driven formation of metal-TCNQ coordination structures on surfaces. In Section 4.1, the formation of Mn-, Fe-, Co- and Ni-TCNQ complexes on Cu(100) is discussed. The ordering dissimilarity of these complexes on Cu(100) cannot be predicted in solution chemistry and emerges on the surface due to the delicate lateral interactions between building blocks and their coupling to the surface. To gain insight into the interplay between adsorbate-substrate and adsorbate-adsorbate interactions, we proceed experiments on a Ag(100) substrate. The Ag(100) substrate provides a similar four-fold symmetry, a larger atomic periodicity and certainly a different chemical environment. The growth phenomenon of Mn- and Ni-TCNQ on Ag(100) is completely different from that on Cu(100), which indicates the active role of the substrate in guiding the self-assembly of adsorbed molecules and metal atoms into larger surface structures (see Section 4.2). These experiments reveal the design principles behind the self-assembly of 2D supramolecular structures, including the thermally activated structural formation, the chemical potential tuned by reactant concentration and the reactivity of adsorbates modified by substrate interaction. Such detailed understanding of self-assembly processes is essential to establish a full scope of 2D supramolecular coordination chemistry.

4.1 Mn, Fe, Co, Ni-TCNQ coordination structures on Cu(100)

A typical experimental STM topograph of the Mn-TCNQ assembly on Cu(100) is shown in Figure 4.1(a). The lower part of the figure shows Mn-free close-packed TCNQ molecules, characterized and modeled in detail in Section 3.1. Above this region is a periodic network structure of a chemical composition of MnTCNQ_2 . The 1:2 M:TCNQ coordination ratio is often encountered in solution-based metal cyanides. In solution chemistry the 1:2 ratio is usually due to TCNQ dimerization or tuning solvent ligands to sterically limit the coordination number. Here, the stoichiometry is achieved by each TCNQ monodentately coordinating to two Mn atoms while each Mn atom coordinating to four TCNQ molecules. The molecular phase converts into the network phase as the Mn is vapor deposited to the surface and appropriate post-annealing is applied. The yield of the MnTCNQ_2 phase is quantitative with the Mn coverage, indicating very efficient diffusion and mixing of each of the two components on the surface. Domain size is typically 30 nm in width. Two differently-oriented domains of the networks were observed, as marked by the red arrows

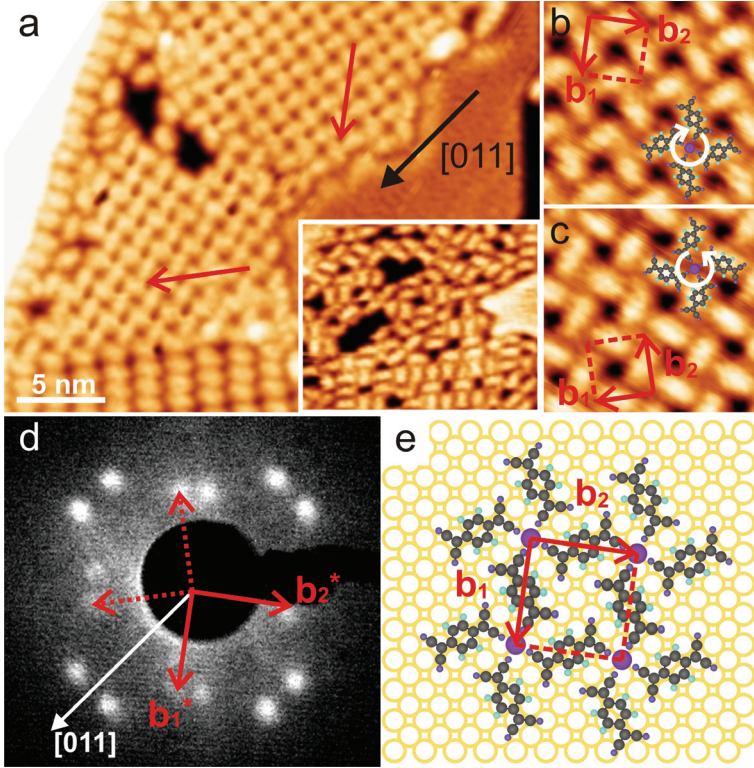


Figure 4.1: (a) STM images of the MnTCNQ₂ networks on the Cu(100) substrate. Two mirror-symmetric networks with their domain orientation $\pm 37^\circ$ from substrate [011], marked by red arrows along the shortest Mn-Mn direction, are observed. The inset shows that the structures become disordered when the Mn concentration is too high. (b-c) STM images reveal that the chirality is achieved by the correlated unidentate linkages of four TCNQ cyano groups to one central Mn atom. (d) LEED pattern of ~ 0.5 ML of MnTCNQ₂ on Cu(100). The $\pm 37^\circ$ -orientated domains are highlighted by the two sets of reciprocal lattice vectors \mathbf{b}_1^* and \mathbf{b}_2^* . (e) Tentative model of the MnTCNQ₂ coordination network. The commensurate (4, 3/ -3, 4) structural matrix leads to a commensurate (5 x 5) unit cell relative to the substrate.

along the shortest Mn-Mn direction approximately $\pm 37^\circ$ from the substrate [011] direction in Figure 4.1(a). These domains are enantiomorphic (i.e., one represents the mirror image of the other) due to the substrate symmetry. They have distinct organizational chirality, where the two enantiomorphic forms differ in the packing of the TCNQ molecules around the Mn center in a propeller-like arrangement. To be more specific, high resolution STM images of the two domains are presented in Figure 4.1(b-c) with TCNQ molecules and Mn atoms overlaid on top. The comparison of the two models shows clearly that the chirality of the complexes is a result of the correlated unidentate linkages of four TCNQ cyano groups to one central Mn atom. Therefore the $+37^\circ$ -oriented domain is composed of clockwise-folded entities and the -37° -oriented domain is anticlockwise-folded as indicated by the arrows around the Mn atoms in Figure 4.1(b-c). The square unit cell of the MnTCNQ₂ superstructure is also depicted in Figure 4.1(b-c). The lattice size, defined by Mn atoms, is measured to be approximately 12.8 Å from STM data. The LEED measurements provide structural parameters which are consistent with the STM data. In Figure 4.1(d) the LEED pattern of ~ 0.5 ML of MnTCNQ₂ on Cu(100) is presented. The two sets of reciprocal lattice vectors (\mathbf{b}_1^* and \mathbf{b}_2^*) indicate the coexistence of two square structures orienting $\pm 37^\circ$ from substrate [011] direction with a periodicity of approximately $5a_0$ ($a_0 = 2.55$ Å, being the nearest neighbor distance of the Cu(100) substrate). Based on the accurate Mn-Mn distance and the domain orientation determined from STM and LEED measurements, a structural model of the MnTCNQ₂ network is proposed in Figure 4.1(e). First, Mn atoms are positioned on substrate hollow sites according to a (4, 3/−3, 4) superstructure matrix with respect to the Cu(100) substrate. This yields a grid of Mn atoms with a periodicity of $5a_0 = 12.8$ Å and \mathbf{b}_1 domain orientations $\pm 36.9^\circ$ with respect to substrate [011], both of which agree well with the STM and LEED data. Then TCNQ molecules are arranged according to the STM topography to coordinate with Mn atoms at their *trans* positions, leading to an adsorption geometry of molecules residing on bridge sites with their molecular long axes approximately 18° from the substrate [011] direction. This molecule orientation is similar to that in the molecular phase discussed in Section 3.1, which hints that the molecule-substrate interaction prevails. In this coordination configuration the cyano groups at the *trans* positions of the molecules coordinate with Mn atoms with the Mn-N coordination bonds estimated to be 2.0 Å from the model. This distance falls in the typical range of metal coordination lengths on surfaces and also agrees with similar metal-N bonds in bulk compounds. A close inspection of the tentative model further shows that the other two "uncoordinated" cyano groups point towards the

top positions of the Cu(100) surface, which is similar to the configuration described in the system of TCNQ/Cu(100) (Figure 3.5). Therefore, the strong bonding between the nitrogen lone pair and the substrate Cu atoms presumably persist upon Mn coordination. We note that no other ordered Mn-TCNQ phase is observed. Further increasing Mn concentration leads to disordered structures as shown in the inset of Figure 4.1(a). In the disordered phase, molecules seem to preferentially pack orthogonal or parallel to the others. Increasing post-annealing temperatures up to 420 K does not change either the ordering or the domain size, indicating a rather strong interaction holding the disordered structures. We expect a strong adsorbate-substrate interaction rendering the disordered Mn-TCNQ domains very stable, which will be discussed in Section 5.1.

We proceed to the synthesis of other metal-TCNQ coordination structures consisting of Fe, Co, or Ni. As presented in Figure 4.2(b), TCNQ molecules coordinate with Fe, forming nanoporous open-cavity networks. Similar to the Mn case, molecular TCNQ domains are observed at insufficient Fe coverages. Disordered aggregates of Fe-TCNQ, as indicated by the white arrows in Figure 4.2(b), can not be fully eliminated by tuning the fabrication parameters. The network structure is found to be very similar to that of the MnTCNQ₂ phase discussed above, i.e., a square lattice defined by a (5 x 5) unit cell rotated $\pm 37^\circ$ from the substrate [011] direction as highlighted by red arrows in Figure 4.2(b). The domain size of FeTCNQ₂ is maximum 10 nm in width, which is significantly smaller than that of MnTCNQ₂ networks. The difference in the domain size of Mn- and Fe-TCNQ₂ can be partially attributed to the natural coordination strength of different metals. This is evidenced by the fact that MnTCNQ₂ networks form at room temperature while only disordered Fe-TCNQ aggregates are observed without post-annealing treatments. It seems reasonable to assume that the Fe-N coordination is strong that once Fe coordinates with TCNQ the whole entity has little mobility to optimize the adsorption configuration. And thus, annealing is required to thermodynamically activate the ordering. The substrate very likely influences the ability of Fe to direct structural ordering since such a strong effect is not observed in bulk compounds produced in solution. Furthermore, the commensurability of MTCNQ₂ networks requires precise matching of the superstructure lattice to the substrate atomic periodicity. In turn, the local metal-N bond length is limited to a narrow range, which can also influence the resultant domain size.

Continuing the study with Co-TCNQ complexes, the coordination structure is completely different from either MnTCNQ₂ or FeTCNQ₂. Most of the Co-TCNQ structures

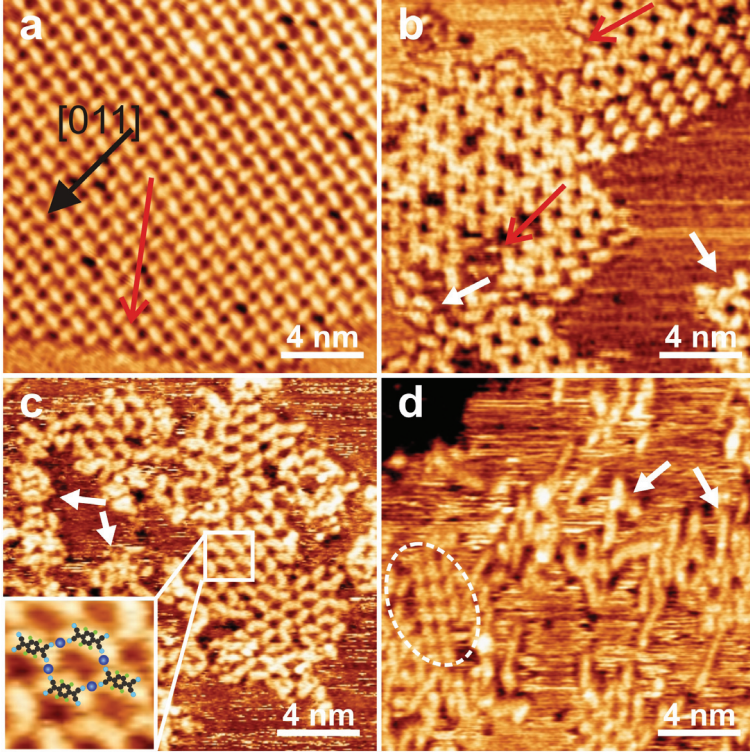


Figure 4.2: (a) a clockwise-folded MnTCNQ₂ domain. (b) FeTCNQ₂ networks in the coexistence of disordered aggregates (marked by white arrows) and molecular TCNQ phase. (c) ordered Co₂TCNQ domains together with disordered structures. The inset signifies the unusual bonding motif, i.e., fully coordinated TCNQ and two-fold coordinated Co atoms. Such Co₂TCNQ networks represent only a minority while most Co-TCNQ structures are disordered. (d) Ni-TCNQ structures exhibit nearly no long-range ordering even though some repeating chain-like structures (pointed by arrows) are observed.

are disordered apart from small pockets of parallel-packed TCNQ molecules as shown in Figure 4.2(c). The inset of Figure 4.2(c) shows the zoom-in of one ordered Co-TCNQ domain where a model of the molecules and Co atoms is superimposed. The model reveals a full coordination configuration of TCNQ, i.e., all cyano groups coordinate to Co atoms monodentately. Each Co atom is two-fold coordinated to two TCNQ molecules, resulting in a 2:1 Co:TCNQ chemical composition. Not only the stoichiometry but also the arrangement of TCNQ molecules has not been observed before. However, this Co_2TCNQ network represents only a minor structure which is observed rarely with a maximum domain size of 5 nm in width. The scarcity of the ordered Co_2TCNQ network can be interpreted as the following: first, the two-fold coordination geometry of Co centers is unusual. Most 2D metal-organic networks that have been synthesized so far with long range ordered domains and high stability comprise metal nodes that are three- or four-fold coordinated to organic molecules [120–123]. Two-fold coordination has been observed in a few Cupyridyl systems and was attributed to the strict substrate templating effect or the steric hindrance for higher coordination due to substrate confinement [124, 125]. Second, the size of the pores in the Co_2TCNQ network is large compared with that in the MnTCNQ_2 phase. Large pores in 2D MOCNs have been achieved by the design of suitable molecule functional sites, lengths and, again, require high coordination numbers of the metal nodes to stabilize the porous networks [120, 121]. In addition, as well-known in solution chemistry, structures with large cavities are generally not stable [126]. In those metal cyanides possessing similar molecular arrangements, solvent molecules or bulky ligands are usually included to support the pores from collapsing [127–129, 137]. Such ligands can bond to metal atoms and thus lead to a more often observed octahedral coordination environment of metal centers, instead of the two-fold linear geometry in the surface-supported Co_2TCNQ .

Most of the Co-TCNQ structure is disordered as indicated by the white arrows in Figure 4.2(b). The disordered aggregates contain constituents of random sizes which can be understood as various combinations of molecules and Co atoms. The existence of TCNQ fragments can not be excluded since some segments are smaller than one molecule but too large to be attributed to Co atoms. The fuzziness of the image also hints that there are mobile species on the surface, which might be TCNQ fragments induced by Co reactivity.

Following the trend of less and less ordering from Mn to Co, the Ni-TCNQ structure on Cu(100) exhibits nearly no ordering (see Figure 4.2(d)). The molecular TCNQ phase

converts into the disordered phase as the Ni is deposited to the surface. Molecular TCNQ domains (highlighted by a dashed circle in Figure 4.2(c)) are observed at insufficient Ni coverages. Similar to Co, Ni atoms exhibit sufficiently strong reactivity to alter the strong Cu-N bonding. The resultant Ni-TCNQ coordination structures show no long-range ordering. However, linear-shaped segments are observed as indicated by white arrows in Figure 4.2(c). It has been difficult to obtain better resolution due to the existence of mobile species on the surface, which is implied by the fuzziness of STM images. However, we could still identify that these linear structures seem to be head-to-head linked molecules instead of the kinked configuration in the Co₂TCNQ network.

Since the atomic size of Mn, Fe, Co and Ni, i.e., the metal-N ligand lengths of Mn-, Fe-, Co- and Ni, are similar, the lattice match between substrate and the ligand length are not expected to influence the resultant structures so dramatically [38, 41, 131, 132]. Therefore, the inherent chemical and electronic properties of different metal species have to be considered. A number of mass spectrometry studies have been reported concerning the reactions between transition metal ions and cyano molecules in gas phase [133–136]. A few important conclusions have been drawn: first, the CN-metal bond strength falls in the order: $\text{CN-Ni}^+ > \text{CN-Co}^+ > \text{CN-Fe}^+ > \text{CN-Mn}^+$, which is governed by the electrostatic interactions. Second, the metal-cyano complexes exhibit two coordination modes, i.e., the end-on and side-on modes. In the end-on mode, metal ions coordinate directly to the nitrogen atom and the CN-metal bond is approximately linear. On the other hand, the side-on mode means that metal ions attach to CN triple bonds. These two coordination modes are competitive in the complexation processes of metal ions and cyano molecules. Mn ions are mostly end-on coordinated while the side-on coordination becomes more and more preferential from Fe, Co to Ni. As end-on coordinated, metal ions can detach without damaging the molecule. Only for large molecules a mechanism termed remote functionalization occurs [137], which can induce the reduction or cleavage of the C-C or C-H bonds remote from the cyano groups. However, in the side-on coordination mode, metal ions can induce bond order reduction, insert into various available C-C or C-H bonds in the molecule and result in molecule fragmentation [133–136]. Finally, the CN-metal bond strength is correlated with the reactivity of the metal ion insertion into C-C or C-H bonds. In the other words, Ni ions exhibit the strongest reactivity to be side-on coordinated and induce bond reduction or molecule decomposition while Mn ions tend to attach in a end-on mode without chemically modifying the molecules. These gas phase phenomena have shown strong correlation to the growth of metal-TCNQ structures on Cu(100). For Mn,

homogeneously ordered MnTCNQ₂ networks can be synthesized and attributed to the relatively weak but moderate cyano-Mn bonding. In the MnTCNQ₂ networks, the Mn centers are end-on coordinated as shown in Figure 4.1 by our STM data and the structural model. At high Mn surface concentrations, the excess of Mn adatoms very likely attach to TCNQ molecules in a side-on mode since the preferential end-on sites are occupied. As side-on coordinated, Mn adatoms can induce chemical modifications of the TCNQ molecules, e.g., bond order reduction, and lead to the disordered Mn-TCNQ structures. For Fe, annealing is necessary to activate the ordering of the stronger cyano-Fe bonding for the formation of FeTCNQ₂ networks. The existence of the disordered Fe-TCNQ structures corresponds to the higher reactivity of Fe and their tendency to be side-on coordinated which result in chemically changed molecular species. In the case of Co and Ni, STM images indicate the existence of mobile species, which are very likely induced by chemical reactions, such as metal insertion and molecule fragmentation described above and in literature [133–136]. Other experiments of cyano molecule adsorption on Ni, Pd or Pt substrates have also demonstrated that the substrate reactivity can induce the reduction of CN triple bond and concomitant strong covalent bonding from the substrate to the carbon or nitrogen atoms [106,107]. This comparison to both gas-phase systems and adsorption on reactive substrates provides a consistent explanation to the ordering phenomena of Mn-, Fe-, Co- and Ni-TCNQ nanostructures on Cu(100). XPS measurements of the M-TCNQ on Cu(100) will be presented in Section 5.1 to gain further insight into their chemical states. For a more detailed understanding, systematic studies of different M-TCNQ combinations on different substrates and theoretical analysis are required.

4.2 Mn, Ni-TCNQ coordination structures on Ag(100)

To gain insight into the substrate effects we proceed to the synthesis of 2D metal-TCNQ complexes on a Ag(100) substrate. In contrast to the buckling of the surface Cu atoms induced by the strong coupling to cyano groups, the Ag(100) surface is chemically less active, as evidenced by the mobility of TCNQ on Ag(100), and therefore is used to reduce the substrate coupling. This allows the analysis of the competition between intra-network forces (e.g. molecule-molecule and molecule-metal interactions) and network-substrate interactions (e.g. molecule-substrate and metal-substrate interactions). Additionally, the larger lattice constant of Ag(100) ($a_0 = 2.89 \text{ \AA}$, being the nearest neighbor distance of the Ag(100) substrate) enables the investigation of the influence of lattice match between

substrate atomic size and superstructure periodicity to the organization of metal-organic coordination networks. Mn and Ni atoms are employed on Ag(100) due to the apparent differences in the structural ordering of Mn- and Ni-TCNQ complexes formed on Cu(100) (see Section 4.1). The growth phenomenon of MTCNQ_x nanostructures on Ag(100) exhibits distinguishing characteristics to that on Cu(100). Long-range ordered MTCNQ_x networks with $x = 1, 2$ or 4 are obtained by controlling the fabrication parameters (e.g. metal/TCNQ concentration ratio, substrate temperature upon adsorbate deposition and post-deposition annealing treatment). In all structures each metal center is four-fold coordinated via monodentate bonds to the cyano groups. The networks are composed of chiral entities and exhibit enantiomorphic arrangements. The $x = 2$ and 4 structures exhibit distinct chiral motifs and are nearly identical for the Mn and Ni metals. However, the two metals differ strongly in the molecular arrangement and uniformity in their $x = 1$ structures when all cyano groups of TCNQ are coordinated to metal atoms. The networks are found to be partially incommensurate to the Ag(100) registry and the non-equivalent binding and adsorption sites of the metal centers are evidenced by distinct topography features in the STM images. The STM data also indicate distinct changes in electronic configuration of the metal centers upon full coordination of TCNQ molecules in the $x=1$ networks.

Ni or Mn atoms are deposited onto the TCNQ precursor layer to obtain charge transfer complexes. The cyano groups of the TCNQ molecules react readily with the metal atoms at room temperature, resulting in the formation of mononuclear complexes as shown in Figure 4.3. The coordination structures formed by these two metals are geometrically identical. Figure 4.3(a) shows an overview STM image of NiTCNQ₄ structures and Figure 4.3(b) exhibits the details of a MnTCNQ₄ domain. These complexes resemble propellers with four TCNQ molecules surrounding a single metal atom. The propeller arrangement of MTCNQ₄ is achieved by monodentate bonds from the nitrogen of the cyano moieties to the central metal atom. A similar coordination motif has been observed in other MOCN systems [138–140]. Two types of MTCNQ₄ propellers, labeled as R (clockwise folded) and S (anticlockwise folded), are identified in high resolution STM images such as Figure 4.3(a) and 4.3(b). The R and S complexes are enantiomorphs, i.e., one represents the mirror image of the other with respect to the substrate [011] direction, as highlighted by yellow and black squares, respectively. Such chiral entities arise from the surface confinement. MTCNQ₄ complexes are mobile and only observed at step edges or in well-ordered MTCNQ₄ domains at sufficiently high concentration of complexes (Figure 4.3(a)).

The domain size increases with coverage or post-deposition annealing treatment and can reach a width of 100 nm. The fuzziness of the bare surface next to the MTCNQ₄ domains in Figure 4.3(a) indicates the presence of mobile species at room temperature.

MTCNQ₄ network is a racemic mixture of the R and S enantiomers as indicated by the alternate yellow and black squares in Figure 4.3(a) and 4.3(b). Two non-equivalent domain orientations can be identified in Figure 4.3(a). Both domains consist of the same R and S enantiomers but differ in the arrangement of the MTCNQ₄ units. As a consequence one domain is not superimposable onto the other by in-plane rotation and translation but instead they are mirror-symmetric to the substrate [011] direction. The two domain orientations are indicated by the **b**₁ unit cell vectors oriented approximately $\pm 19.0^\circ$ with respect to the substrate close-packed direction (Figure 4.3(a)). The unit cell of the MTCNQ₄ superstructures in Figure 4.3 is indicated by the **b**₁ and **b**₂ vectors. The lattice size, which is equivalent to the second shortest metal-metal distance, is measured to be approximately 28.1 Å from STM data. Based on the accurate topographical information from the STM data a model of the structure is proposed in Figure 4.3(c). In the model we assume that the metal centers reside on the energetically favored hollow sites of the substrate (M^{hollow}). Four molecules arrange around one metal center with their central ring adsorbed close to bridge sites. The M-N bond is estimated to be 1.9 Å from the model, which is in good agreement with similar M-N bonds in bulk compounds and typical metal coordination lengths in two-dimensional MOCNs [38, 41, 124, 131, 132, 138, 141]. Note, that we expect strong relaxations of the molecules upon adsorption (see Chapter 3) which can affect the bond distances significantly [14, 81, 142]. However, for simplicity we assume an unrelaxed gas-phase structure of the TCNQ molecule in our models. The propeller-like packing of TCNQ molecules could be stabilized by potential intra-complex hydrogen bonds. R complexes are composed of molecules with the long axes $+19.0^\circ$ from the [011] direction while S complexes are composed of -19.0° oriented molecules. The molecule orientations are nearly identical to those in the molecular phase shown in Figure 3.6. This means that the two equivalent adsorption configurations of the molecules lead to distinct chiral binding motifs upon coordination to Mn or Ni atoms. In principle, e.g., the $+19.0^\circ$ rotated molecules should form also an S complex (anticlockwise-folded) if only the coordination of the metal center to the molecules is considered. However, this enantiomer has not been observed for these molecules, signifying that the binding to the surface breaks the symmetry of the organic ligand. This can be seen in the model of the molecular phase already in Figure 3.6(c) where only the cyano groups at *trans* positions have

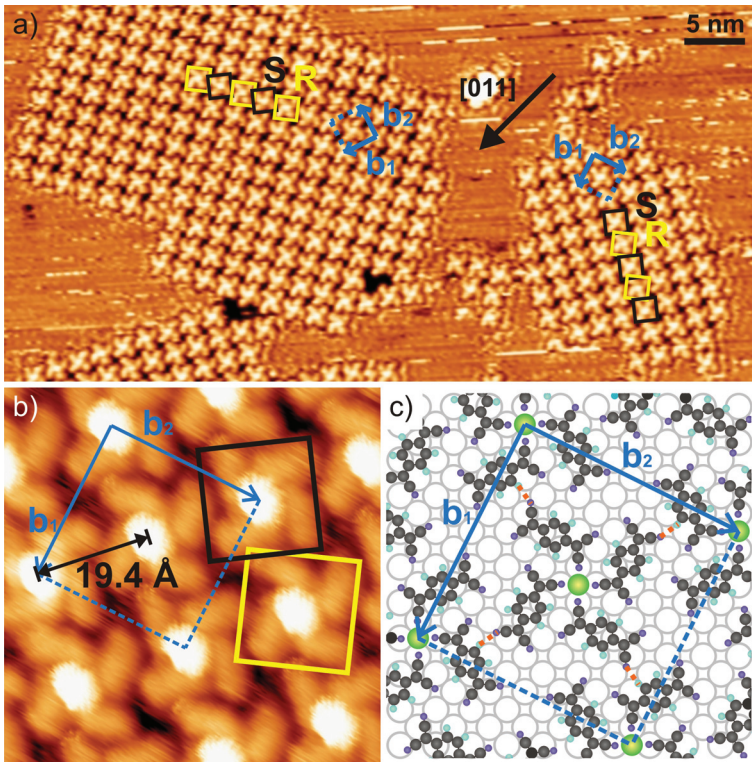


Figure 4.3: (a) STM image of NiTCNQ₄ networks on Ag(100). Mirror-symmetric NiTCNQ₄ complexes, R and S, are observed. The complexes self-assemble into ordered hydrogen bond-assisted networks at sufficiently high coverage. Such NiTCNQ₄ domains are racemic, i.e., composed of alternately packed R and S species as highlighted by yellow and black squares, respectively. Due to the substrate symmetry, two mirror domains are observed. (b) High resolution STM image of MnTCNQ₄ network with the R-, S-complex and the unit cell marked. The structure is identical to the NiTCNQ₄. (c) Structural model based on distances and orientations measured in STM images. Metal coordination and potential inter-complex hydrogen bonds, highlighted by orange dotted lines, amount to 1.9 and 2.4 Å, respectively.

identical adsorption sites. Note, that this difference was found to have dramatic effects on the coupling of vanadium adatoms by the related TCNE molecule on Ag(100) [143]. Since the molecules do not change significantly their orientation upon coordination, it evidences that the molecule-substrate interactions prevail. The MTCNQ₄ network can be expressed by the commensurate superstructure defined by (9, 3/-3, 9). The model gives a periodicity of $9.5a_0 = 27.5 \text{ \AA}$ and domain orientations of $\pm 18.4^\circ$ with respect to [011] in good agreement with the STM data. The formation of extended structures suggests that the surface plays a role in guiding the self-assembly as well as the formation of single complexes. Furthermore, the racemic packing of R and S enantiomers is likely mediated by inter-complex hydrogen bonds as depicted by orange dotted lines in Figure 4.3(c). The bond lengths are estimated to be 2.4 \AA , which can be reasonably associated to weak hydrogen bonds. Each MTCNQ₄ binds to four adjacent complexes through such hydrogen bonds. Due to the intermediate strength of both adsorbate-substrate interaction and inter-complex hydrogen bond, single MTCNQ₄ complexes can reversibly attach to the networks, as revealed by the continuously changing domain edges and the presence of mobile single MTCNQ₄ complexes.

Both Ni and Mn centers in MTCNQ₄ complexes have very pronounced contrasts as shown in the STM images of Figure 4.3. Contrast in STM images is a convolution of geometric contour and lateral variations in the charge density of the surface structure, which is directly related to electronic properties. Although scanning parameters and tip conditions can modulate the absolute apparent heights, the complexes are mainly imaged as presented in Figure 4.3. In particular, the metal centers are much brighter than the molecules. Therefore such unusual contrasts can be associated with electronic properties rather than tip-induced phenomena. The apparent heights of Ni and Mn relative to the molecules are 0.7 and 1.2 \AA , respectively. Such prominent contrasts were not observed in MTCNQ complexes on Cu(100) (see Section 4.1). As will be discussed later, we ascribed these observations to distinct electronic states of the metal centers generated by the surrounding ligand and substrate environment.

Upon increasing the metal concentration another two-dimensional square metal cyanide phase with a stoichiometry of MTCNQ₂ evolves. The local bonding motif is similar to that in the Mn- and Fe-TCNQ₂ networks on Cu(100) discussed in Section 4.1, i.e., each TCNQ is monodentately coordinating to two Mn atoms while each Mn atom is four-fold coordinated to cyano groups. The resultant networks on Cu(100) and Ag(100) have therefore a similar structure. However, the substrate interaction still leads to specific growth direc-

tions on the Ag(100) surface, which will be discussed in detail in the following. Although the composition is identical to most common metal-cyanide crystals, the coordination structure of the surface-supported MTCNQ₂ networks differs strongly from the bulk compounds in which the 1:2 ratio is achieved by TCNQ dimerization or tuning solvent ligands to sterically limit the coordination number [38,132,144,145]. Similar to the 1:4 phase, the structure of the NiTCNQ₂ and MnTCNQ₂ networks on Ag(100) are indistinguishable.

In Figure 4.4 the STM images of NiTCNQ₂ domains are presented. The size of the MTCNQ₂ domains is typically $20 \times 20 \text{ nm}^2$. The high-resolution STM image presented in Figure 4.4(b) shows that the nearest neighbor metal centers are not identical but exhibit alternately stronger and weaker contrasts. The R and S MTCNQ₄ entities are identified to be the primary building blocks of the MTCNQ₂ networks as highlighted by the yellow and black squares in Figure 4.4(a-b). Based on the STM analysis of metal-metal distances and domain orientations a tentative model is proposed in Figure 4.4(c). Individual MTCNQ₄ complexes are adsorbed with their bright metal centers on hollow sites at the same azimuthal orientation as in the MTCNQ₄ domains (see, e.g., the R complex highlighted by the yellow square in Figure 4.4(b)). Adjacent MTCNQ₄ complexes are of the same chirality and positioned according to the superstructure matrix $\begin{pmatrix} 5 & 4 \\ -4 & 5 \end{pmatrix}$. According to the STM data, the dimmer metal atoms link the corners of MTCNQ₄ units together and therefore will reside on top sites of the substrate as revealed by the geometrical model in Figure 4.4(c). Thus, two mirror symmetric structures are formed and labeled as R and S domains since they are composed of respectively R and S propellers linked by additional metal atoms (Figure 4.4(a)). This configuration is consistent with STM images that display two types of metal centers. The difference between the apparent heights for the two different metal centers amounts to about 0.4 \AA . A similar value was found for the MnTCNQ₂ network. This distinction in height reveals differences in the local density of states at the metal centers. A careful analysis of the STM images suggests that TCNQ molecules are slightly closer to the brighter centers, which is consistent with our model. A close inspection of the model reveals that the N-M^{top} and N-M^{hollow} bonds are not equivalent in either bond angles or lengths, which is highlighted by the inequivalent red dashed squares formed by the four N atoms around the two types of metal centers (Figure 4.4(c)). These differences in binding geometry as well as adsorption sites, explain the alternate apparent heights of metal centers in the STM images. Such a height modulation of the metal centers was not observed for the nearly identical MnTCNQ₂ structure on Cu(100). On the copper surface, the MnTCNQ₂ domains grow uniformly (see Figure

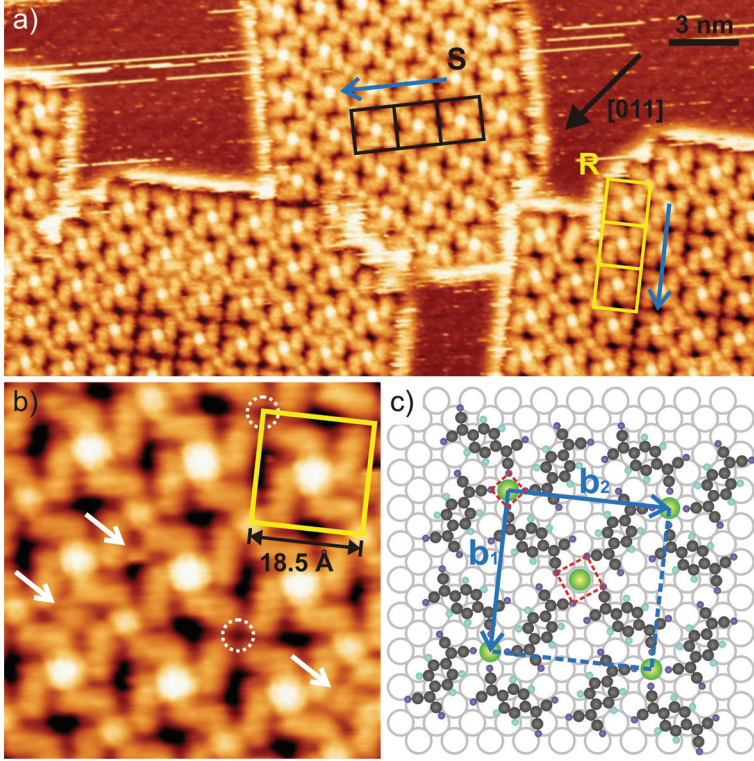


Figure 4.4: (a-b) STM images and (c) structural model of NiTCNQ₂ networks on Ag(100). The STM images of MnTCNQ₂ networks are nearly identical. The MTCNQ₂ networks are homochiral and composed of either R or S enantiomers. Therefore the R domains are mirror symmetric to the S domains with the \mathbf{b}_1 unit cell vectors oriented $\pm 38.7^\circ$ with respect to the substrate [011] direction measured from the model. The alternate contrasts of metal centers are attributed to the differences in adsorption sites and local binding configuration (see text).

4.1). We will discuss the relationship between the STM contrasts and the electronic states of metal centers in Chapter 5.

In both Ni- and Mn-TCNQ₂ networks metal vacancies are observed as indicated by the white dotted circles in Figure 4.4(b). All metal vacancies are found at the dimmer sites, which can be well explained by our model since top sites are less favorable and N-M^{top} bonds are expected to be weaker because of non-optimal bond angle and length. Another observation that supports our model is that the rims of MTCNQ₂ domains always terminate with MTCNQ₄ complexes with brighter centers (Figure 4.4(a)). This phenomenon implies that the MTCNQ₂ network is composed of MTCNQ₄ units and additional coordination nodes of metal atoms as we propose. Furthermore, interstitial Ni atoms are observed in NiTCNQ₂ networks as indicated by white arrows in Figure 4.4(b). The Ni interstitials are mobile and hop between the pores of the NiTCNQ₂ networks. In the pores, the trapped Ni atoms coordinate in an end-on mode but cannot coordinate to more than one or two molecules at the same time (see the structural model in Figure 4.4(c)). In addition, they can hop to attach to cyano groups in a side-on coordination mode (see the discussion in Section 4.1), which explains the mobility of Ni interstitials in the NiTCNQ₂ networks. Mn interstitials are also observed in MnTCNQ₂ networks. However, such hopping behavior is less observed for Mn. Since Mn atoms prefer end-on coordination to cyano groups, the difference in the hopping of Mn and Ni atoms can be reasonably attributed to their distinct metal-cyano interactions.

The interconnected R and S complexes in MTCNQ₂ networks retain their azimuthal orientations as in the MTCNQ₄ domains. The apparent height of the bright M^{hollow} centers also remains unaltered, i.e. Ni^{hollow} = 0.7 Å and Mn^{hollow} = 1.2 Å relative to the molecule. This indicates that the MTCNQ₄ monomers are not altered upon interconnection by additional M^{top} atoms. The formation of MTCNQ₂ networks can therefore be understood as the rearrangement of MTCNQ₄ complexes from the hydrogen bond-assisted networks to accommodate additional metal atoms as coordination nodes. The process of the MTCNQ₂ formation is enantioselective. The R and S MTCNQ₄ enantiomers separate, leading to homochiral MTCNQ₂ network domains. The two types of MTCNQ₂ networks, R- and S-domains, are consequently mirror symmetric with their **b**₁ vectors enclosing an angle of +38.7° and -38.7° given by our model to the substrate [011] direction, respectively. The stable domain boundaries indicate that the MTCNQ₄ complexes are more stable while interlocked by metal centers within MTCNQ₂ networks compared to the hydrogen-bonded network discussed above. Quantitatively each TCNQ molecule monodentately

coordinates to two metal atoms, which accounts for the structural stability.

Further increasing the Ni concentration results in networks with a 1:1 Ni:TCNQ stoichiometry. Two types of NiTCNQ structures are observed, including the square α phase and the rhombic β phase shown in the left and right panels of Figure 4.5, respectively. At a sample preparation temperature below 460 K the coexistence of α , β and NiTCNQ₂ with hopping Ni atoms is observed. The preparation at 400 K results in the formation of α and β networks of about 20 and 5 nm in width, respectively. The domain size of both α and β increases with higher preparation and post-deposition annealing temperature and can be as large as 40 and 120 nm in width, respectively. After preparation at 400 K, the fraction of 1:1 phase can be raised at the expense of the 1:2 phase with post-deposition annealing treatment up to 460 K. Above 440 K, the coverage of β phase increases faster than α phase and at 460 K pure 1:1 phase is obtained with the coverage ratio of approximately $\alpha:\beta = 1:1.6$. We could not obtain pure β phase because further increase of substrate temperature results in the decomposition of TCNQ molecules.

In the α phase the TCNQ molecules orient perpendicular to their neighboring molecules, which is clearly resolved in the enlarged STM image in Figure 4.5(b). The metal centers are imaged with alternating contrast, whereas no height modulation was found for the molecules. Due to the square structure of the α -NiTCNQ networks, two mirror symmetric domains are observed (cf. Figure 4.5(a) and (b)). The domain orientation is defined by the \mathbf{b}_1 vector along the shortest Ni-Ni direction. The structure is similar to the 1:2 network with all pores filled with metal atoms. However, there are three distinguishing features of the α -NiTCNQ networks compared to the 1:2 phase: first, the metal centers at *trans* positions of the molecules have the same apparent height in contrast to the 1:2 structure. Second, the 1:1 α network is more densely-packed than the 1:2 phase. The length of the \mathbf{b}_1 vector is 11.8 ± 0.5 Å measured from the STM data. In fact, the packing density of the molecules is highest in this phase even compared to the pure molecular phase. Third, the \mathbf{b}_1 orientation is measured to be $13.8 \pm 1.2^\circ$ from the substrate [011], which means that the α phase does not comprise NiTCNQ₄ as primary building blocks as the 1:2 networks do. Based on the above-mentioned distances and angles a geometrical model is proposed in Figure 4.5(c). The square unit cell is expressed by the superstructure matrix $(4, -1/-1, -4)$. Both the orientation, $\pm 14.0^\circ$ from substrate [011], and the length, 11.9 Å, of the \mathbf{b}_1 vector are in good agreement with the STM measurements. Furthermore, the Ni atoms reside alternately on hollow and top sites in the model, which explains the alternate contrasts of Ni centers along the orientation of the diagonal of the

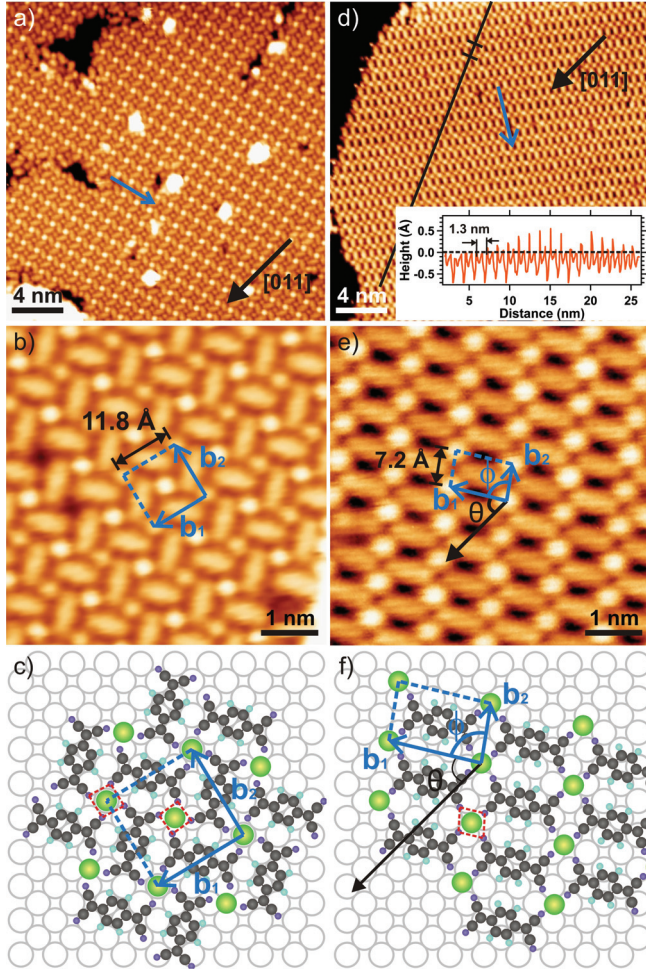


Figure 4.5: STM images and geometrical models of (a-c) α and (d-f) β NiTCNQ phases. The lattice of the α phase is square whereas the β phase is rhombic, as indicated by the unit cells depicted on the STM images. Structural models are proposed based on the dimensions and orientations from STM data. From the models, the α phase is commensurate to the substrate while the β phase is not. The (in)commensurability is related to the substrate coupling and results in distinctive STM contrasts.

unit cell. TCNQ molecules adsorb on bridge sites and arrange perpendicularly to the neighboring molecules. In this phase the TCNQ molecules are fully coordinated, i.e., all cyano groups are coordinated to Ni atoms. The inequivalent bonding of cyano groups at *cis* positions are indicated by the red dotted squares in Figure 4.5(c). The lengths of the coordination bonds are estimated to be 2.0-2.2 Å, which fall in the range of typical metal-ligand distances, while the bond angles are 147.9-149.5° measured from the model.

The apparent heights of the two types of Ni centers in the α -NiTCNQ network relative to molecules are 0.2 Å and -0.2 Å, which are substantially different from those in NiTCNQ₂. This hints that this phase is electronically different to either NiTCNQ₄ or NiTCNQ₂. Here, all molecules are fully coordinated which could result in the reduced interaction with the substrate and therefore a lifting of the molecules away from the Ag(100) surface. In this case, the coupling of α -NiTCNQ to the substrate is greatly reduced, leading to electronically distinctive networks.

The other type of the 1:1 Ni:TCNQ network, denominated as β phase, is presented in the right panels of Figure 4.5. Within a single domain of the β phase the TCNQ molecules orient parallel to each other. Figure 4.5(d) and (e) show the mirror symmetric domains with the marked domain orientations parallel to the molecular long axes. The 90°-rotational domains are observed elsewhere on the surface. The rhombic unit cell is depicted in the high resolution STM image of Figure 4.5(e). The unit cell parameters are measured and averaged to be $|\mathbf{b}_1| = 11.3 \pm 0.2$ Å, $|\mathbf{b}_2| = 7.2 \pm 0.3$ Å, $\phi = 85.6 \pm 1.5^\circ$, and $\theta = 58.5 \pm 2.5^\circ$ (see Figure 4.5(e)). According to these dimensions and angles a commensurate superstructure is not likely. Therefore we propose that the β -NiTCNQ network is incommensurate to the Ag(100) substrate. The geometrical model (Figure 4.5(f)) is depicted according to the above measured distances and orientations. TCNQ molecules are also fully coordinated in this structure, i.e., four monodentate bonds per TCNQ molecule. Due to both the rhombic symmetry and incommensurability the four Ni-N bonds are not equivalent in the bonding geometry and also have some variations in angle and length. Therefore each Ni center has a distorted fourfold coordination as highlighted by the red dotted rhomb in Figure 4.5(f). TCNQ molecules are also fully coordinated in this structure, i.e., four monodentate bonds per TCNQ molecule. Due to both the rhombic symmetry and incommensurability the four Ni-N bonds are not equivalent in the bonding geometry and also have some variations in angle and length. Therefore each Ni center has a distorted fourfold coordination as highlighted by the red dotted rhomb in Figure 4.5(f). A careful analysis of the STM data shows that the boundaries of the β networks

terminate along both diagonals of the unit cell, meaning that the binding strength along the longer diagonal is similar to that along the shorter even though the bond lengths are not equivalent in the model. This signifies the limitation of the tentative model because effects such as bond bending and stretching to optimize the coordination interactions cannot be revealed. The bond length is measured to be 1.9-2.3 Å from the model, which is similar to that in the α phase. On the other hand, the Ni-N bond angles in the β phase given by the model is 160.4-170.8°, which are close to the optimal linear configuration. Note, that the variation in bond length and angle is due to the two non-equivalent Ni-N bonds in the rhombic unit cell. The optimal bond angles are expected to lead to a strong intra-layer interaction which explains the formation of huge β domains above 440 K despite the incommensurability. The increasing β phase with higher temperatures hints that the molecules and Ni atoms need thermal energy to overcome an energy barrier to form this structure where the adsorbates presumably do not reside entirely on preferential adsorption sites.

Although the stoichiometry is identical to the α phase, the molecular arrangement and incommensurability are expected to affect the electronic properties of the β -NiTCNQ network. The STM contrast reveals distinctive features between the α and β -phase. In the β phase the heights of the Ni centers exhibit a continuous modulation of the apparent height of about 0-0.5 Å relative to the molecules along the direction of the shorter diagonal of unit cell. The inset of Figure 4.5(d) displays a line profile along the short diagonal of the unit cell running across both Ni atoms and TCNQ molecules. The dashed black line indicates the uniform apparent heights of TCNQ. The Ni positions are indicated by markers 1.3 nm from each other. It can be clearly seen that the Ni centers exhibit a wave-like pattern in the apparent height. The origin of this effect could be related to the apparent incommensurability with the Ni centers being more sensitive to their atomic environment, or such a modulation reveals complicated intrinsic electronic properties of the network. Neighboring profiles along the short diagonal of the unit cell do not exhibit a clear periodicity, however they are also not completely unrelated. The wave-like pattern of adjacent profiles appears to be shifted by about half of the wave length shown in Figure 4.5(d), i.e., by ~ 8 nm or 7-8 unit cells.

Analogous bonding motifs and geometrical structures for both 1:1 networks were reported for bulk compounds, where the crystalline structure is tuned by synthesis routes [43, 141, 146–148]. The structures found on the surface represent sheets of the continuous metal-TCNQ bulk structure where the coordination to the molecules is limited to two

dimensions. Compared to the bulk the metal atoms have a reduced coordination number. Such bulk analogues are reported to exhibit electrical conductivity or magnetic ordering. Since all reactive cyano groups are engaged in coordination bonds we expect that the interaction of the molecules with the surface is significantly reduced. However, it remains to be shown if such fully reticulated networks exhibit in part some of the intriguing electronic properties of their parent bulk compounds. We note, that no further structural transition was observed upon increasing the metal concentration.

The 1:1 structures are clearly distinguished from the $x = 2$ and 4 networks. This becomes more evident when using Mn as coordination centers. The 1:1 phase can also be produced with Mn atoms (see Figure 4.6) but, although the $x = 2$ and 4 structures are identical for both metals, the $x = 1$ phase of MnTCNQ exhibits pronounced differences compared to NiTCNQ. At a preparation temperature above 400 K, small α MnTCNQ domains about 8 nm in width can be formed. By increasing the substrate temperature to 460 K, the domain size can be increased to about 15 nm. The square MnTCNQ structure contains many Mn vacancies and big voids. Defects cannot be fully eliminated by annealing at 460-470 K until the molecules decompose at even higher temperatures. The high resolution STM image (inset of Figure 4.6) shows that neighboring molecules have a small misalignment from perpendicular packing, meaning that the long axes of molecules are not azimuthally identical. Small domains of parallel-packed β -MnTCNQ phase are also observed as indicated in Figure 4.6. In contrast to the huge domains formed by Ni, the β MnTCNQ forms only small patches of max. 5 nm in width and represents only a minority structure. The structural ordering reflects the chemical dissimilarity between Mn and Ni since such pronounced changes cannot be predicted by atomic size or coordination number as both metals form indistinguishable $x = 2$ and 4 structures. This behavior is not expected from the coordination chemistry point of view. While isostructural M-TCNQ compounds of different metal species can be synthesized in bulk with local variations in bond lengths and angles [38, 132, 144, 149], here the tolerance to such local variations is reduced due to surface confinement. In addition, the full coordination of the TCNQ renders the molecular networks very rigid. Therefore the limited conformational freedom of bond bending and stretching could explain partially the structural dissimilarity between NiTCNQ and MnTCNQ. An opposite phenomenon is observed on Cu(100) where MnTCNQ₂ forms well-ordered domains whereas Ni-TCNQ does not show any ordering (see Figure 4.2(d)). This signifies that the adsorbate-substrate interaction can alter considerably the chemistry of the adsorbates which is ultimately

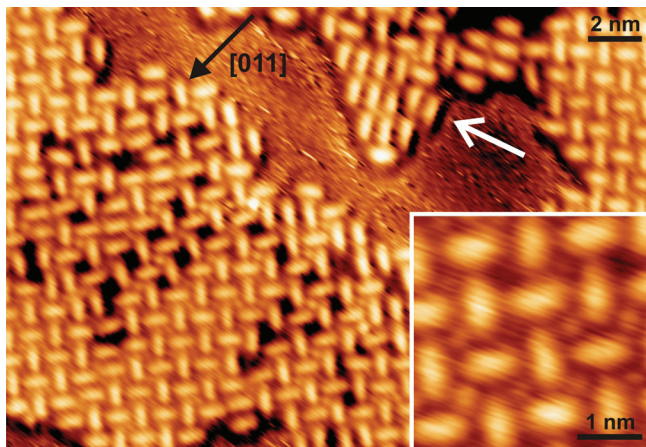


Figure 4.6: STM images of MnTCNQ networks. The structures have many similarities to NiTCNQ but with considerably less ordering. The inset shows the nonuniformity of Mn centers which can be attributed to the structural disorder of the MnTCNQ phase. The Mn centers are imaged as depressions with respect to the TCNQ molecules.

revealed in the formation or absence of ordered patterns. Besides the structural variation, the contrast of the metal centers also displays appreciable differences. Instead of the regular contrasts of the Ni centers in NiTCNQ networks, Mn centers in the 1:1 phase are usually imaged as depressions with nonuniform heights (inset of Figure 4.6). The nonuniformity can be attributed to structural disorder while the overall darker contrast is probably due to the inherent electronic difference of the MnTCNQ from NiTCNQ and networks with lower Mn concentrations.

The structural transition from MTCNQ_4 arrays to interconnected MTCNQ_2 networks exhibits a hierarchical self-assembly process. This phase transformation is driven by the relative metal concentration and occurs at room temperature, which is attributed to the weak and reversible hydrogen bonding between MTCNQ_4 entities. The next level of structural complexity, the 1:1 phases, requires both sufficient metal concentration and appreciable thermal activation for the network formation. As discussed in the previous section, the MTCNQ_2 networks can be transformed into 1:1 phases at the presence of hopping metal atoms above 400 K. The excess of metal atoms enables this phase trans-

formation. As the 1:1 networks are structurally not related to the MTCNQ_4 entities in contrast to the MTCNQ_2 networks, the formation of 1:1 structures requires the dissolution of MTCNQ_4 but not a simple rearrangement of primary building components on the surface. In addition, it requires a different interaction between the cyano groups and the substrate to allow the 1:1 fully coordinated configuration to occur. Both of them explain the high preparation or post-annealing temperatures required for complete structure transition into the 1:1 phases. Such organizational hierarchy has been observed in a few other two-dimensional metal-coordination systems and appears to be a feature of rather small ligand molecules [138, 140].

4.3 Summary and Comparison

In Section 4.1 the M-TCNQ ($M = \text{Mn, Fe, Co, Ni}$) structures on $\text{Cu}(100)$ are presented. The four metals exhibit distinct growth phenomena with TCNQ from long-range ordered MnTCNQ_2 to completely disordered Ni-TCNQ segments. Lattice match is one of the controlling factors of the resultant structure. However, it seems not sufficient to explain the dramatic differences because the M-N bond lengths have only small variation as reported for bulk crystals. Therefore, apart from geometrical considerations, there must be other factors governing the growth of 2D supramolecular structures. The inherent chemical properties of different metals is certainly crucial, e.g., reactivity and electronic configuration. The substrate hybridization is also important, which changes the chemistry of metal atoms and molecules, and therefore makes it impractical to directly apply 3D supramolecular rules to 2D. To fully understand the changes between systems requires further studies comparing different combinations of M-TCNQ and substrates.

The growth of MTCNQ_x ($x = 1, 2, 4$) on $\text{Ag}(100)$ further highlights the determining role of the substrate in 2D supramolecular self-assembly. Sufficient thermal mobility enables molecules to arrange themselves into ordered structures [150]. Instead of the single ordered 1:2 M:TCNQ phase observed on $\text{Cu}(100)$, the various structures formed on $\text{Ag}(100)$ are attributed to the weaker substrate coupling on $\text{Ag}(100)$. The 1:4 and 1:2 networks are based on the same MTCNQ_4 primary components and therefore the phase transformation is driven by the chemical potential raised by metal concentration. The 1:1 phase is structurally not based on the MTCNQ_4 blocks. The formation requires sufficient metal concentration, the dissolution of the MTCNQ_4 entities and at the same time the breaking of cyano-substrate bonding by increasing the substrate temperature. All the

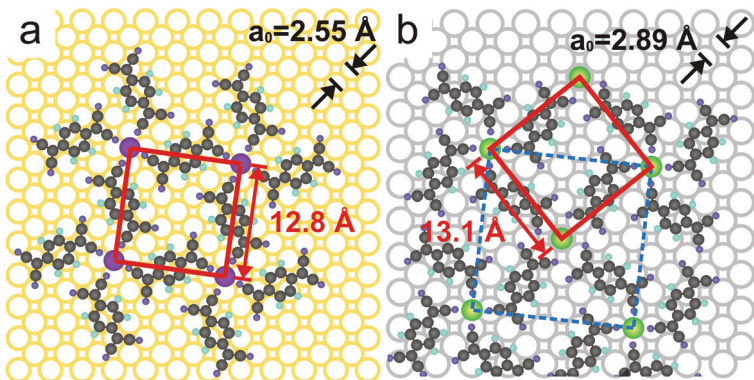


Figure 4.7: Geometrical models of MTCNQ_2 networks on (a) $\text{Cu}(100)$ and (b) $\text{Ag}(100)$ substrates. The red squares enclose the smallest metal grids of respective networks are similar in size, i.e., edges of 12.8 and 13.1 Å for $\text{Cu}(100)$ and $\text{Ag}(100)$, respectively. The growth orientation are adapted to follow the substrate periodicity. The blue dashed square in b indicates the structural unit cell.

networks are composed of regular arrangements of Mn or Ni centers with interdistances ranging from 7.2 to 19.4 Å mediated by the TCNQ ligands. The electronic changes evidenced by STM topographs in these MTCNQ_x structures reflect the local coordination bonding environments as well as the $\text{M}:\text{TCNQ}$ coordination ratio. The $\text{Ag}(100)$ substrate greatly accounts for the structure formation, signified by the detailed arrangements emerging from the adsorbate-substrate coupling. This enables the intricate interactions within the MTCNQ_x complexes to be explored.

The geometrical models displayed in Figure 4.7 are to emphasize the similarity in the coordination geometry of MTCNQ_2 networks synthesized on $\text{Cu}(100)$ and $\text{Ag}(100)$. The MTCNQ_2 on both substrates can be regarded as a metal grid held by TCNQ molecules. The grid size is therefore defined by TCNQ molecules and roughly equivalent to the diagonal distance of TCNQ, due to the M-N bonding at molecule *trans* positions, as highlighted by the red squares in Figure 4.7. The similar grid size obtained on two different substrates indicates that the M-N interaction is strong enough to retain the same geometry on two different substrates. However, the substrate interaction still leads to specific growth direction as illustrated by the two differently oriented red grids in Figure

4.7. The rotation of the grid assists the network to adapt substrate periodicity. Not only the domain orientation, the fine details of the structure also adjust themselves to optimize the coordination configuration, e.g., the two types of metal adsorption sites in the case of the Ag(100) substrate and the local bond stretching allowed by flexible coordination interactions.

Substrates not only guide the network formation but also actively modify the adsorbate chemical properties and influence their coordination ability. The well ordered networks on Ag(100) contrast sharply with the generally disordered structures on Cu(100) (except MnTCNQ₂). Further studies are required to accurately describe how substrate interactions participate and how much they can influence the supramolecular structures.

Chapter 5

Physical Properties of Metal-TCNQ Coordination Structures

During the past five decades, TCNQ has been extensively studied due to a wide range of electrical, magnetic and structural properties exhibited in TCNQ-based compounds. The variety of properties arises from its electron accepting ability which leads to the formation of charge transfer complexes with many organic and inorganic electron donor species. One of the famous examples is the metallic electrical conductivity of TTF-TCNQ [35, 101]. This discovery has raised the interest in designing organic metals and has led to the development of a family of metal-TCNQ conductors and semiconductors [98, 99, 102, 141]. Despite extensive efforts to understand these materials, there has been a long debate on their electrical behavior and the conducting mechanism has not been fully understood yet. One of the crucial issues to be resolved is the coordination structure and crystallinity of metal-TCNQ compounds. Since the molecule packing is highly dependent on the material preparation conditions, most of the conflicts in literature regarding the electrical conduction is very likely related to the chemical nature of the materials. The attempt to understand the origin of electrical conduction has amplified again the importance of charge transfer by the observation of two-dimensional conduction between two insulating crystals of TTF and TCNQ [103]. In those experiments, the interface quality, e.g., imperfection at the crystal surfaces or uncontrollable relative orientation of the two crystals, might have led to the substantial spread in the measured interfacial conductivity. Therefore, there is a demand for controlled sample preparation for the elucidation of physical properties. The magnetic behavior of metal cyanide materials is governed by spin moments induced by charge transfer. In contrast to most molecular magnets in

which magnetic interactions are too weak to maintain ordering at ambient temperatures, cyano molecules are unique in dictating spin coupling as shown by room-temperature organic magnets VTCNE₂ and $M[M'(CN_6)]$ [43, 70, 104]. Unfortunately, these materials often lack crystallinity and therefore the microscopic origin of the exceptional properties is not fully understood. Recently, self-assembled organic monolayers on well-defined substrates have drawn considerable attention. These experiments have shown the possibility to create very complex two-dimensional architectures. However, the exploration into their physical properties is still at the beginning [71, 103]. In the previous chapters, we have discussed the growth behavior of metal-TCNQ coordination networks on metal surfaces. To gain further insight into their chemical and magnetic states, we will present the physical properties of 2D MTCNQ_x in the following. The charge transfer phenomena are discussed in Section 5.1 with a combined analysis of x-ray photoelectron spectroscopy (XPS) measurements and density functional theory (DFT) calculations. The magnetic properties of MTCNQ_x complexes on Cu(100) and Ag(100) obtained by x-ray magnetic circular dichroism (XMCD) are presented in Section 5.2.

5.1 Charge Transfer of Metal-TCNQ coordination structures on Cu(100)

XPS reveals element-specific electronic information and is used to study the bonding, local environment and charge state of Mn-, Fe-, Co- and Ni-TCNQ coordination structures on Cu(100). XPS spectra of the nitrogen 1s region are shown in Figure 5.1 for (a) MnTCNQ₂ networks, (b) disordered Mn-TCNQ and (c) Fe-TCNQ grown on Cu(100). The N 1s lineshape of Co- and Ni-TCNQ are very similar to that of Fe-TCNQ. The N 1s core level shifts of neutral TCNQ powder and TCNQ monolayer on Cu(100) are marked for comparison by the two grey dashed lines at 399.6 and 398.7 eV, respectively (c.f. Figure 3.3). The N 1s XPS spectrum of MnTCNQ₂ is very similar to that of TCNQ adsorbed on Cu(100). The main N 1s resonance is at 398.7 eV and a shake-up feature is identified at 399.8 eV. This result indicates no significant variation in the charge state of TCNQ upon switching from Cu-N to Mn-N bonds, despite the obvious change in the overall coordination structure. In addition to the charge state of TCNQ, the 398.7 eV peak has been associated with the π -bonding of the CN triple bond to the Cu(100) substrate (see Section 3.1). We can thus infer that such cyano-substrate interactions still participate in the stabilization of MnTCNQ₂ networks. This conclusion is consistent with our tentative

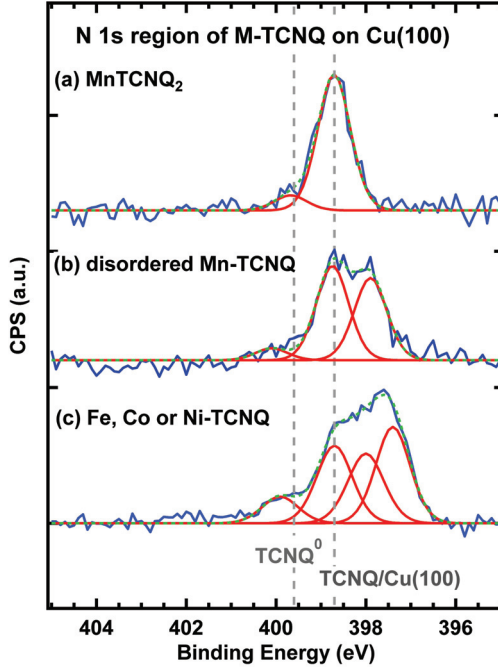


Figure 5.1: XPS N 1s spectrum of (a) MnTCNQ₂ networks, (b) disordered Mn-TCNQ and (c) Fe-, Co- and Ni-TCNQ structures on Cu(100).

model (Figure 4.1(e)) which shows that half of the cyano groups interact with the substrate ascribed to the specific orientation and adsorption site of TCNQ.

Increasing Mn concentration results in disordered Mn-TCNQ structures as shown in the inset of Figure 4.1(a). Concomitant with the formation of disordered Mn-TCNQ, the XPS spectrum shows an additional component at 398.0 eV (Figure 5.1(b)). The 398.0 eV peak grows with the reduction of the 398.7 eV peak and with increasing Mn concentration. This energy shift has been assigned to represent TCNQ⁻² anion in NiTCNQ compounds [91,92]. Thus, the emergence of the 398.0 eV peak implies further charge transfer to TCNQ at a higher Mn:TCNQ ratio although the structure does not exhibit long-range ordering. The spectrum of Fe-, Co- and Ni-TCNQ (Figure 5.1(c)) shows a further broadening of the

N 1s XPS peak. In addition to the 398.7 and 398.0 eV peaks observed in the spectrum of disordered Mn-TCNQ, one more component is identified at 397.3 eV. The well-defined peak positions indicate specific nitrogen configurations although no long-range ordering has been observed. The 397.3 eV peak suggests the existence of an even more negatively charged TCNQ component upon coordination with Fe, Co or Ni, compared with the disordered Mn-TCNQ structures.

Since the XPS peak position is sensitive to the coordination environment and chemical state as well as the charge state, we provide an alternative interpretation to the multiple XPS peaks as the following. It has been shown in gas-phase experiments that Mn, Fe, Co and Ni metal ions react with cyano molecules by attaching at the cyano groups in either end-on or side-on coordination modes [133–136]. The metal coordination can induce the reduction of the CN triple bonds or even lead to molecule decomposition, especially when side-on coordinated, which has been attributed to the formation of disordered M-TCNQ structures on Cu(100) (see Section 4.1). It has also been reported that the adsorption of cyano molecules on Ni, Pd or Pt substrates involves a strong chemical hybridization of the CN triple bonds to the substrate in a side-on configuration, which leads to the reduction of CN triple bonds to double (sp^2 hybridized) or single bonds (sp^3 hybridized) [106, 107]. The degree of hybridization, depending on the interaction strength, corresponds to the XPS N 1s core level shifts from 398.0 (sp^2 hybridized) to 397.3 eV (sp^3 hybridized). The XPS core level shifts we observed here seem to have a strong correlation to the chemical reaction and bond order reduction observed in the systems of cyano adsorption on reactive substrates. In the case of Mn, the XPS spectrum of MnTCNQ₂ networks shows a single peak at 398.7 eV, indicating the intact cyano triple bonds (Figure 5.1(a)). At higher Mn concentrations, the formation of the disordered Mn-TCNQ structures can be attributed to the excess Mn adatoms attaching in a side-on mode to the CN bonds as discussed in Section 4.1. This coordination mode consequently leads to the reduction of the triple bonds to double bonds as evidenced by the XPS peak at 398.0 eV. In comparison with Mn, the Fe, Co and Ni metal adatoms possess stronger chemical reactivities and tendencies to be side-on coordinated to CN triple bonds. Consistently, the 398.0 and 397.3 eV peaks indicate the reduction of CN triple bonds to double and single bonds, respectively, due to a robust chemical reaction induced by metal adatoms. Upon the bond reduction, the molecule adsorption mode switches from CN π -bonding to covalent bonding from the carbon and nitrogen atoms to the metal adatoms or to the Cu(100) substrate [106, 107]. Such a strong covalent bonding hinders the self-assembly of adsorbates and to some extent

explains the disordered structures due to the lack of surface mobility. Finally, as STM images of disordered M-TCNQ structures (Figure 4.1 and 4.2) indicate the existence of mobile species on Cu(100), molecule fragmentation cannot be completely excluded, especially for Co- and Ni-TCNQ, and can be associated with the multiple XPS peaks in Figure 5.1. A more detailed description of how different metal species induce such chemical reactions requires further systematic studies and theoretical analysis.

To understand more accurately the charge transfer phenomenon of the MnTCNQ₂ networks on Cu(100), we performed density functional theory (DFT) calculations to complement the XPS measurements. The structure simulated by DFT methods agrees well with the geometrical model presented in Figure 4.1. The assumption that Mn centers reside on hollow sites is confirmed to be a highly probable geometry by a local energy minimum in the total-energy calculations. The optimum distance between Mn and the four nearest Cu atoms is 2.98 Å, which is slightly longer than the sum of the covalent radii of Cu (1.32 Å) and Mn (1.61 Å for Mn in high spin state). The DFT calculation further shows the TCNQ conformational bending and surface Cu atom buckling, both cannot be concluded simply from STM data. The C atoms of the TCNQ central ring are at an average height of 3.32 Å above the average position of the flat part of the first copper layer. The Mn atoms reside on hollow sites and are 0.89 Å lower than the C atoms in the central ring. Two of the cyano groups of a TCNQ molecule are slightly tilted towards the Mn atoms, which facilitates the coordination of nitrogen lone pairs to Mn atoms. The Mn-N bond is 2.15 Å. The other two cyano groups are strongly bent towards the metal surface with the N atoms binding to the Cu surface atoms with a Cu-N bond of length 2.00 Å. Both Cu-N and Mn-N distances can be reasonably attributed to metal coordination bonds. The copper atoms binding to the N atoms of TCNQ move outwards by 0.20 Å compared to the average height of the other Cu atoms in that layer. This substrate reconstruction is similar to the lift of 0.22 Å occurred in the adsorption of TCNQ on Cu(100) in the absence of Mn (cf. Figure 3.5). Thus, when two of the cyano groups switches to coordinate with Mn atoms, the other two stays unchanged with similar Cu-N bonds.

The bending of the bonds results from the conformational freedom of TCNQ molecules obtained upon charge transfer (see Figure 2.7). Through Bader charge analysis of the DFT optimized geometry, we can gain insight into the charge-transfer mechanism by considering the partial systems listed in Table 5.1. We stress that the trends in such charges are more meaningful than the precise numerical values since these numbers depend on how the

Table 5.1: Bader charge analysis in units of $|e|$ in the different calculated models. N1 are nitrogen atoms that bind to Cu while N2 are nitrogen atoms that bind to Mn in the full system.

System	per TCNQ	Mn	Cu(100)	N1	N2
2TCNQ	0			-1.00	-1.00
2TCNQ/Cu(100)	-1.12		+2.25	-1.24	-1.10
2TCNQ+Mn	-0.73	+1.46		-1.04	-1.31
2TCNQ+Mn/Cu(100)	-1.38	+1.33	+1.43	-1.24	-1.30

charge is partitioned between ions. The atomic coordinates of the three partial systems are the same as in the full 2TCNQ+Mn/Cu(100) system. In the absence of either Cu substrate or Mn adatoms as electron donors, both N1 and N2 atoms are $-1.00|e|$ charged due to the intramolecular charge distribution while the whole molecule is neutral (cf. the electrostatic potential of TCNQ in Figure 3.1). In the Mn-free 2TCNQ/Cu(100) system, we found a transfer of $-1.12|e|$ from the copper surface to each TCNQ and in the 2TCNQ+Mn system, a transfer of $-0.73|e|$ per TCNQ occurs from Mn. In the full system, the TCNQ molecule carries a negative charge of $-1.38|e|$. The charge of Mn is $+1.33|e|$, whereas the Cu(100) surface is charged to $+1.43|e|$. The charge on the TCNQ in the full 2TCNQ+Mn/Cu(100) system, $-1.38|e|$, exceeds those in the partial systems, indicating that both the Cu and the Mn contribute to the electron donation. For the Mn-free 2TCNQ/Cu(100) system, the charge redistribution is principally localized in the N-Cu bonds, where each N1 atom gains $-0.24|e|$ relative to N in the pure molecular 2TCNQ system. For the 2TCNQ+Mn system in the absence of the Cu substrate, the N2 atoms gain $-0.31|e|$. Consistently, the charges on the N atoms in the full system increase by $-0.24|e|$ for N1 and $-0.30|e|$ for N2. This charge increase is primarily due to the donation from Cu to N1 and from Mn to N2. This analysis reveals that in the full system the charge of the N1 atoms in the Cu-N bonds is similar to that of the N2 atoms in the Mn-N bonds, which is reflected in the XPS data by the similar peak position before and after Mn coordination (see Figure 5.1). This is also consistent with a strong electron donation from both Mn and Cu to the TCNQ, especially to the N atoms. This significant charge transfer is a critical aspect of the system, both for structural arrangement and for determining the electronic configuration.

We next address the magnetic property in the full system, i.e., 2TCNQ+Mn on

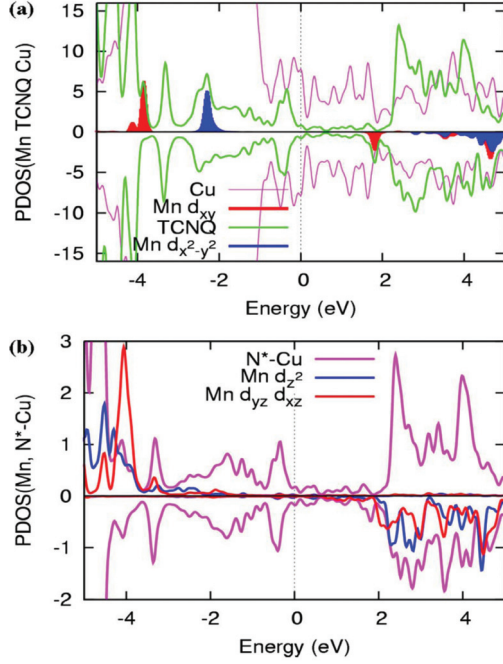


Figure 5.2: (a) The PDOS of the top copper layer, of the TCNQ molecule, and of the Mn d_{xy} and $d_{x^2-y^2}$ orbitals. (b) The PDOS of the Mn d_{xz} , d_{yz} , and d_{z^2} orbitals and of the four N atoms bonded to Cu.

Cu(100). Figure 5.2 shows the projected density of states (PDOS) on the top Cu layer, on the TCNQ molecule, on the four N atoms bonded to Cu and on the five Mn d orbitals. In Figure 5.2(a), the PDOS on the TCNQ molecules shows a sharp peak at $E_F - 3.5$ eV, a family of peaks at $E_F - 2.5$ eV, and another sharp peak at $E_F - 0.5$ eV. Compared to the PDOS on the N atoms bonded to Cu shown in Figure 5.2(b), the similarity between them indicates that the cyano groups close to Cu atoms are the dominant contribution to the DOS of TCNQ. However, TCNQ and Cu do not participate in the spin polarization as shown by the spin up and spin down peaks occurring at the same energy. As the two TCNQs in one unit cell are symmetry equivalent and each represents a closed shell system

in which all electrons are paired, they should each receive two electrons. Two electrons are given by Mn atoms and the other two from the Cu atoms engaged in Cu-N bonds. Figure 5.2 also shows that the five Mn d orbitals are each occupied by one electron. Therefore, Mn atoms can be regarded as Mn^{2+} ions in the d^5 state. We further found that Mn in a high spin state is more stable than the low spin state by 0.675 eV. The magnetic moment for the Mn atom reaches $\mu = 4.9 \mu_B$, which is close to the nominal value of 5 for a Mn^{2+} ion in a high spin state. Finally, we searched for a periodic spin arrangement and found that the ferromagnetic configuration of the Mn^{2+} ions is more stable than the antiferromagnetic configuration by only 5 meV per Mn ion. Therefore, we conclude from our DFT calculations that spin is highly localized on Mn ions in the MnTCNQ_2 networks on Cu(100). Experimental results of magnetic properties of M-TCNQ networks on metal substrates will be presented in the next section by x-ray magnetic circular dichroism (XMCD) measurements.

5.2 Magnetic Properties of Metal-TCNQ Coordination Structures

XAS and XMCD are used to study the electronic and magnetic properties of MTCNQ_x complexes synthesized on Cu(100) and Ag(100) surfaces. In comparison with metallic Mn and Ni impurities, the XAS multiplet structure at both the Mn and Ni L -edges shows the localized $3d$ orbital configuration due to the formation of coordination bonds to the TCNQ molecules. From the XAS and XMCD lineshapes, the electronic states of Mn and Ni are identified to be d^5 and d^9 , respectively. The analysis of the XMCD further yields valuable information on the magnetic moments of Mn and Ni in the coordination networks.

The experiments were performed at the beamline ID08 of the European Synchrotron Radiation Facility in Grenoble. The coordination structures were prepared *in-situ* and characterized by STM before XAS measurements. The metal impurities were prepared by the deposition of minute quantities of metal atoms on substrates held at 8 K to obtain isolated adatoms. XAS spectra were recorded at the metal L -edges and the nitrogen K -edge in total electron yield mode with circularly polarized light (I^+ or I^-) in magnetic fields up to 5 T. XMCD spectra were obtained by taking the difference of XAS spectra recorded at opposite light polarization. Linearly polarized light (in-plane or out-of-plane) was used to probe the orientations of empty orbitals at a grazing incidence angle ($\theta =$

70°). In the following, the results are organized by the coordination metal species into two main parts: MnTCNQ_x and NiTCNQ_x.

Figure 5.3(a) and (b) show the XAS spectra of MnTCNQ₂ and 0.025 ML Mn impurities on Cu(100) recorded with linear light polarization (T = 8 K, B = 50 mT), respectively. In comparison with the Mn impurities, the MnTCNQ₂ networks exhibit a pronounced multiplet structure signifying localized atomic orbitals. The strong linear dichroism at the Mn *L*-edge signifies the strong interaction between the Mn atoms and the TCNQ molecules, which implies a low-symmetry crystal field around the 3*d* shell of Mn atoms. XAS spectra for right (*I*⁺) and left (*I*[−]) circular polarization obtained at the Mn *L*_{2,3}-edge for the MnTCNQ₂ and Mn impurities on Cu(100) are shown in Figure 5.3(c) and (d), respectively. The corresponding XMCD spectra (*I*[−] − *I*⁺) are also plotted for each case. The XAS and XMCD spectra are compared with the atomic multiplet calculations reported by van der Laan and Thole [151] to determine the electronic configurations of the Mn atoms. For Mn impurities adsorbed on Cu(100) (Figure 5.3(d)), the spectra strongly resemble the calculated *d*⁵ high-spin configuration in zero crystal field. The isotropic spectra also indicate a vanishing crystal field and the hybridization with the metal substrate. On the other hand, the XAS and XMCD lineshape of MnTCNQ₂ on Cu(100) suggest that the Mn centers are mostly dominated by coordination bonds to TCNQ. However, there is still a close match to the *d*⁵ configuration (see the zoom-in of the *L*₃ XMCD spectra in Figure 5.5(g)), indicating that the binding to the TCNQ molecules does not change the electron occupation in the Mn *d* shell in accordance with the DFT calculations. The magnetization curves recorded at the *L*₃-edge at incident angles $\theta = 0^\circ$ and 70° after normalization are presented in Figure 5.3(e) and (f). Paramagnetic behavior is observed for both MnTCNQ₂ and Mn impurities on Cu(100) as shown by the absence of remanent magnetization. Additionally, for MnTCNQ₂/Cu(100), the relative intensity of XMCD to XAS, i.e., the normalized XMCD signal, is inversely proportional to temperature from 300 to 8 K (not shown), which also indicates a Curie-like paramagnetic behavior. No anisotropy has been observed in Figure 5.3(e) and (f). The fitting of the magnetization curves (shown by dotted lines in Figure 5.3(e) and (f)) with the Brillouin function suggests a total angular momentum $J = 5/2$. Since the analysis of the XMCD branching ratio indicates a negligible orbital moment, we can thus conclude that the MnTCNQ₂/Cu(100) consists of independent paramagnetic Mn centers in a *d*⁵ high-spin state, i.e., $S = 5/2$ and $L = 0$, and the Mn impurities/Cu(100) behave similarly. However, as the MnTCNQ₂ networks represent ordered arrays of spin moments stable at temperatures up to 460 K,

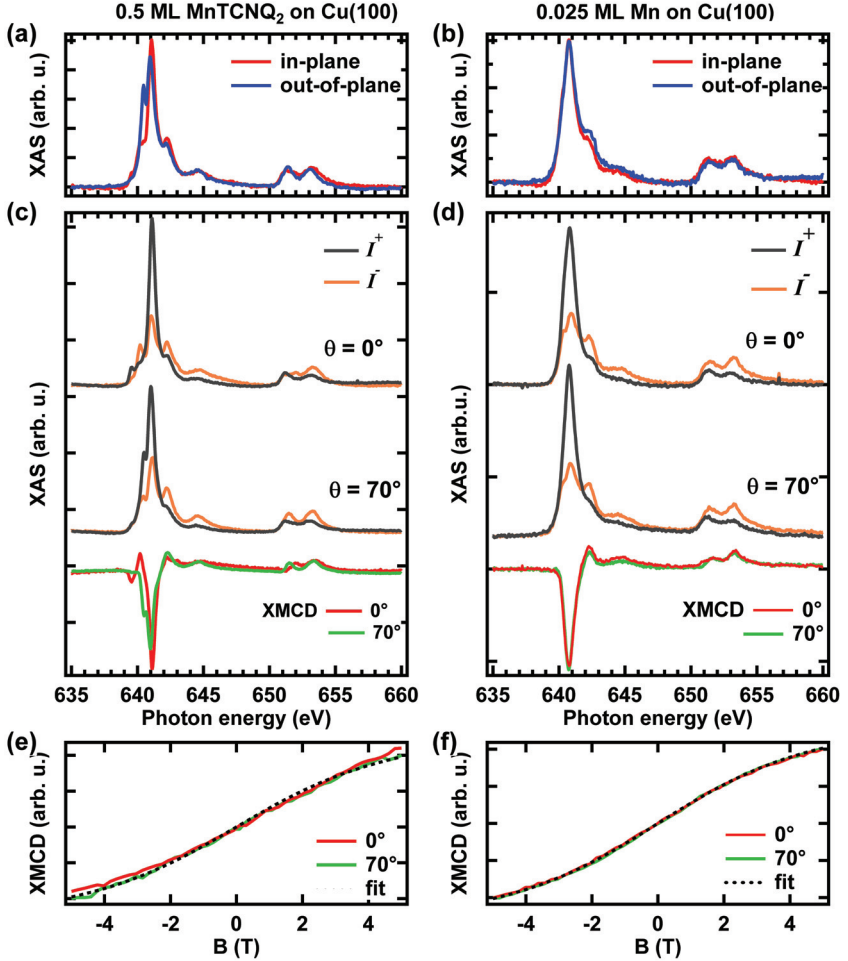


Figure 5.3: XAS and XMCD of MnTCNQ₂ and 0.025 ML Mn impurities on Cu(100). (a)-(b) XAS for linear polarized light parallel to the surface (in-plane) and 20° to the surface normal (out-of-plane) ($T=8$ K, $B=50$ mT). (c)-(d) Circular polarized XAS at 0° (normal) and 70° (grazing) incidence and the corresponding XMCD ($T=8$ K, $B=5$ T). (e)-(f) Magnetization curves obtained by the Mn L_3 XMCD intensity at $T=8$ K. Fitting by a Brillouin function yields a spin magnetic moment of $S = 5/2$ for the Mn atoms in both cases.

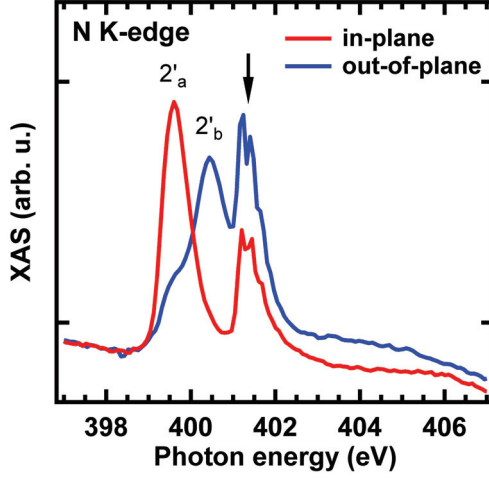


Figure 5.4: Linear polarized XAS spectra recorded at $T = 8$ K, $B = 5$ mT. The XAS lineshape indicates strong interaction between cyano groups and the Mn centers, as well as the Cu substrate. The arrow marks a feature arising from the adsorption of molecular nitrogen (N_2) in the cryogenic environment.

the Mn impurities would form clusters or surface alloy at elevated temperatures, which have been observed to exhibit a much lower magnetic moment [152].

Figure 5.4 shows the nitrogen K -edge XAS spectra measured with linearly polarized light for the MnTCNQ₂ networks on Cu(100). There is a noticeable signal of molecular nitrogen (marked by an arrow) resulting from the absorption of molecular nitrogen in the cryogenic environment. Apart from this, the XAS lineshape is similar to the NEXAFS spectra shown in Figure 3.4(a) for TCNQ on Cu(100). Two main peaks are identified and can be denoted as $2'_a$ and $2'_b$ accordingly. The presence of $2'_a$ and $2'_b$ peaks indicates the strong Mn-cyano coordination as well as the substrate-cyano interaction. In comparison with the spectra shown in Figure 3.4(a), the $2'_a$ peak of Mn-coordinated TCNQ shows a stronger angular dependence. In the other words, the molecular orbital corresponding to the $2'_a$ peak is more in-plane localized when cyano groups coordinate to Mn adatoms. This phenomenon is consistent with the reduced bending of cyano groups when coordinating

to Mn adatoms, than to the substrate, as our DFT calculation suggests. The zero XMCD intensity observed at the N-edge (not shown) indicates no orbital magnetic moment localized on nitrogen atoms. Although information of spin magnetic moment is not available from the N K -edge spectra, the absence of orbital magnetic moment is consistent with the conclusion deduced from DFT calculations (Figure 5.2) that TCNQ molecules represent a closed shell system in which all electrons are paired due to the charge transfer from both Mn and Cu substrate. This closed shell configuration also partially explains the absence of magnetic coupling between the Mn centers since TCNQ molecules could not act as a mediator for spin exchange coupling. The other reasons include the strong Mn-substrate coupling which can quench the spin coupling or alternatively due to the large distance between the Mn centers (12.8 Å, cf. Figure 4.1).

Figure 5.5 shows the comparison of Mn L_3 -edges of MnTCNQ₂ on Cu(100), MnTCNQ₂ on Ag(100) and MnTCNQ on Ag(100). As can be seen in the the XAS spectra recorded with linearly polarized light (Figure 5.5(a)-(c)) and the corresponding x-ray natural linear dichroism (XNLD) spectra (Figure 5.5(d)-(f)), a strong natural linear dichroism is observed in all the three networks which signifies the formation of strong coordination bonds to the TCNQ molecules in each structure. The variation in the lineshape and peak intensities are strongly influenced by the ligand field imposed by the surrounding cyano groups, even though all Mn centers are four-fold coordinated, and the local adsorption environment. From the coordination structure point of view, the MnTCNQ₂ networks on Cu(100) and Ag(100) are similar to each other apart from their domain orientations with respect to the substrate high symmetry [011] directions (Figure 4.7). However, interestingly, the lineshape of MnTCNQ₂/Cu(100) has a strong resemblance to that of MnTCNQ/Ag(100) while the MnTCNQ₂/Ag(100) shows an obvious difference from them. Since XAS resonances are directly related to electronic properties, we propose that these (dis)similarities reflect the inherent properties of the Mn centers. A comparison of the STM images of these three structures (Figures 4.1, 4.4 and 4.6) shows that the Mn coordination centers in MnTCNQ₂/Cu(100) and MnTCNQ/Ag(100) appear as depressions while the Mn centers in MnTCNQ₂/Ag(100) are bright and exhibit alternate contrasts. We thus conclude that there is a strong correlation between STM contrasts and the XAS lineshape, which is reasonable since both are associated with electronic properties.

Figure 5.5(g)-(i) shows the XMCD L_3 -edge spectra of MnTCNQ₂ on Cu(100), MnTCNQ₂ on Ag(100) and MnTCNQ on Ag(100). Corresponding to the XAS and XNLD, there is a strong similarity between (g) and (i) while (h) possesses additional features together

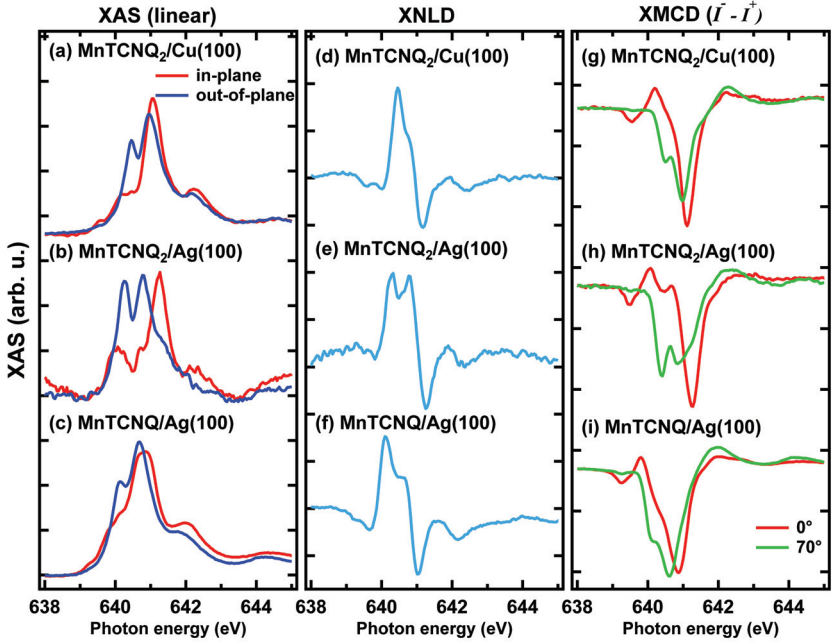


Figure 5.5: Comparison of Mn L_3 -edges of MnTCNQ₂ on Cu(100), MnTCNQ₂ on Ag(100) and MnTCNQ on Ag(100). (a)-(c) XAS spectra measured with linearly polarized light (8 K, 5 mT), (d)-(f) XNLD (8 K, 5 mT) and (g)-(i) XMCD spectra ($I^- - I^+$) (8 K, 5 T).

with variations in relative peak intensities. The analysis of the XAS and XMCD spectra of MnTCNQ₂ and MnTCNQ on Ag(100) suggests that the Mn centers are in the d^5 high-spin state with negligible spin coupling. Theoretical calculations are in progress in order to gain insight into the crystal field effects.

In the following we discuss the magnetic properties of NiTCNQ_x on Ag(100). The XAS spectra for the $x = 1, 2$ and 4 structures strongly resemble each other and thus the results of the NiTCNQ₂ system are presented. The XAS spectra for linear polarization ($T = 8$ K, $B = 50$ mT) of NiTCNQ₂ and 0.018 ML Ni impurities on Ag(100) are shown in Figure 5.6(a) and (b), respectively. For Ni impurities, the similar L_3 intensities measured at in-plane and out-of-plane light polarization imply the isotropic orbital distribution at the

Ni atoms. In the case of Ni centers coordinated to TCNQ, the out-of-plane L_3 intensity almost vanishes. The single in-plane absorption peak at the L_3 -edge thus indicates a single hole in the ground state lying in the surface plane. Again, the anisotropy is attributed to the crystal field induced by ligand coordination.

XAS spectra measured with right (I^+) and left (I^-) circular polarization and the corresponding XMCD spectra are shown in Figure 5.3(c)-(d) ($T = 8$ K, $B = 5$ T). The lineshape of Ni impurities is very simple, showing a single peak at the L_3 -edge and almost zero L_2 intensity (Figure 5.3(d)). The absence of the L_2 resonance implies that only the transition from the initial $j = 3/2$ to the final $j = 5/2$ occurs. In comparison with literature, the lineshape suggests a d^9 configuration [153]. The very low XMCD intensity shows the almost complete quenching of the Ni spin moment. At this coverage one would expect a significant amount of Ni dimers and Ni adatoms at step edges (and so forth), and therefore the moment of a single Ni impurity on a terrace could be completely quenched. In ferromagnetic Ni, the ground state is represented by a hybridized d^8 , d^9 and d^{10} configuration [154, 155]. Here we argue that a change in the d^{10} weight due to the substrate hybridization can lead to the non-magnetic behavior of Ni impurities adsorbed on Ag(100). On the other hand, the Ni centers in coordination with TCNQ molecules exhibit substantial XMCD intensity (Figure 5.3(c)). The single L_3 peak and the XAS lineshape indicate a d^9 configuration with the hole in the plane. In addition, satellite features at ~ 3.2 eV above the L_3 and L_2 mainlines are noticeable in the XAS spectra and become prominent in the XMCD spectra. The satellite peaks can be attributed to the hybridization of the d states to the unoccupied s or p states lying above the d band and to the configurational mixing of the d^8 state to the d^9 state [155–157]. The weighting of the d^8 , d^9 and d^{10} states is related to the satellite intensity and the Ni spin moment. Thus, an electronic configuration of a mixture of d^8 , d^9 and d^{10} states can be expected for the NiTCNQ₂ on Ag(100). The magnetization curves of NiTCNQ₂ on Ag(100) are presented in Figure 5.3(e). Fitting the magnetization curves with the Brillouin function yields a total angular momentum $J = 1.86$ at 8 K. This J value suggests the existence of an orbital magnetic moment since the highest possible spin moment value for a d^8 , d^9 and d^{10} hybridized state would not exceed $S = 1$. Analysis of the XMCD branching ratio consistently indicates an appreciable orbital moment at the Ni centers. As discussed above, the Mn centers in the structurally identical MTCNQ₂ network on Ag(100) do not possess an orbital magnetic moment due to their orbital singlet ground state given by Hund’s rule. In addition to the different Ni-substrate interaction, the orbital moment

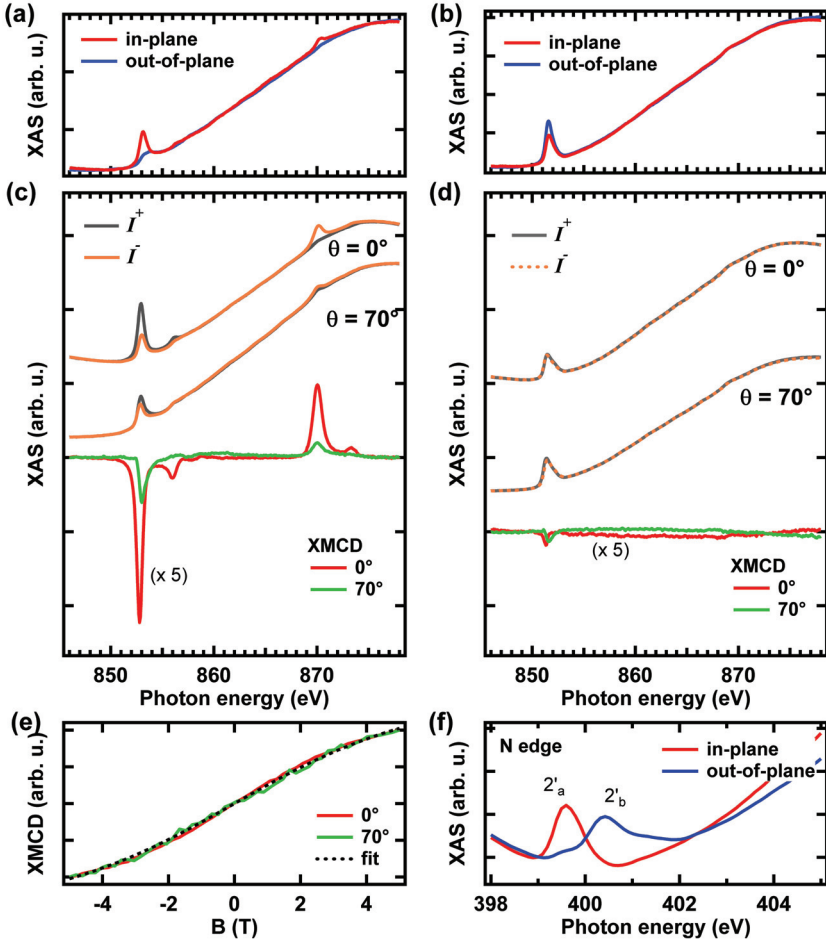


Figure 5.6: XAS spectra measured at linear polarized light parallel to the surface (in-plane) and 20° to the surface normal (out-of-plane) for (a) NiTCNQ₂ and (b) 0.018 ML Ni impurities on Ag(100) ($T=8$ K, $B=50$ mT). (c) and (d) are the XAS and XMCD spectra for NiTCNQ₂ and 0.018 ML Ni impurities on Ag(100), respectively ($T=8$ K, $B=5$ T). (e) Magnetization curves of NiTCNQ₂ on Ag(100) obtained by the Ni L_3 XMCD intensity at $T=8$ K. (f) Linearly polarized N edge XAS spectra of NiTCNQ₂ on Ag(100).

on Ni comes from spin-orbit coupling and the possible mixing of the d^8 state, since d^8 has some orbital moment on its own. Unfortunately, XMCD spectra at nitrogen K -edge do not provide information on spin magnetic moments but only indicate no orbital moment localized at nitrogen atoms. In order to determine the spin moment on nitrogen, further analysis and theoretical calculations are in progress. Furthermore, the L_3 peak of NiTCNQ₂ is shifted by 1.1 eV to higher energy than that of Ni impurities. This energy shift again indicates the strong crystal field environment of Ni centers due to the rearrangement of atomic orbitals upon TCNQ coordination. Nevertheless, charge transfer effects might contribute to the XAS energy shift. As a general phenomenon, the absorption energy increases with the oxidation number [158]. Thus, this energy shift implies that the Ni centers in the NiTCNQ₂ networks are more positively charged than the Ni impurities supported by the Ag(100) substrate, which is consistent with the expectation of charge transfer from Ni coordination centers to TCNQ molecules.

Figure 5.6(f) shows nitrogen K -edge XAS spectra measured with linearly polarized light for the NiTCNQ₂ networks on Ag(100) (300 K, 5 mT). Two main peaks are identified and can be associated with the $2'_a$ and $2'_b$ peaks shown in Figure 3.7(a). The presence of $2'_a$ and $2'_b$ peaks indicates strong interaction of cyano groups to both Ni adatoms and the Ag(100) substrate. Similar to the MnTCNQ₂ on Cu(100) (Figure 5.4), the almost-vanishing out-of-plane intensity of the $2'_a$ peak indicates the strong in-plane localization of the molecular orbital localized on cyano groups. Since the molecular orbital orientation is directly related with the bond angle, we thus conclude that the cyano groups are less-bent as switching from substrate-cyano to Ni-cyano coordination.

In conclusion, the multiplet XAS and XMCD structures of both Mn and Ni coordination centers display the robust modification of the metal electronic configuration by molecular ligands, compared with the relatively featureless spectra of metal impurities adsorbed on surfaces. In the case of MnTCNQ_x, the networks represent regular arrays of paramagnetic atoms carrying a high spin moment of $S = 5/2$. The detailed XAS and XMCD lineshape show the electronic configuration of Mn centers and are correlated with STM contrasts. For NiTCNQ_x networks on Ag(100), magnetism is induced by the dehybridization from the substrate, bonding to the molecules and the accompanying charge transfer in the system. Further analysis is in progress in order to elucidate the intricate electronic and magnetic interactions.

Chapter 6

Summary and Perspectives

In this thesis, 2D supramolecular architectures of TCNQ and M-TCNQ ($M = \text{Mn, Fe, Co}$ and Ni) at $\text{Cu}(100)$ and $\text{Ag}(100)$ surfaces have been explored. The focus of this study lies on two aspects. First, the principles underlying molecular self-assembly on metal surfaces have been discussed. Charge transfer has been shown to be a prime factor governing the molecular self-assembly. Controlling the subtle interplay between adsorbate-adsorbate and adsorbate-substrate interactions by varying supramolecular building blocks, surface chemistry and substrate temperature has led to the synthesis of a variety of MTCNQ_x complexes. Second, the chemical and magnetic properties of TCNQ and MTCNQ_x coordination nanostructures have been investigated with a combination of XPS and XAS studies and DFT calculations.

The self-assembly of TCNQ on a $\text{Cu}(100)$ substrate has been examined. Charge transfer from substrate to TCNQ has been shown to induce a molecular conformational bending. This bending allows the cyano groups to coordinate with substrate atoms and consequently results in a significant substrate reconstruction. The substrate reconstruction caused by TCNQ adsorption influences the nucleation and growth of the TCNQ domains. Finally, with the mediation of electrostatic interactions, TCNQ molecules assemble into elongated rectangular islands. The results show the dramatic consequences of charge transfer across the interface, which not only induces a structural rearrangement at both the TCNQ molecules and the $\text{Cu}(100)$ surface but also affects the growth of the organic film. The mutual interactions of TCNQ and $\text{Cu}(100)$ have been revealed by a combination of surface analytic techniques which provide complementary information. STM allows the visualization of TCNQ arrangements on $\text{Cu}(100)$ with an atomic resolution while XPS and NEXAFS measurements reveal information on the charge transfer and TCNQ bending.

DFT calculations support the conclusions drawn from experimental studies and assist the interpretation of experiments.

TCNQ has high surface mobility on the Ag(100) substrate at room temperature and thus well-ordered domains are only observed when the molecular coverage is close to a full monolayer. Despite the larger work function and reduced reactivity of Ag(100) compared to Cu(100), a charge transfer occurs as TCNQ adsorbs on Ag(100). NEXAFS analysis consistently indicates a bent conformation of TCNQ concomitant with the charge transfer. Together with the molecular packing shown by STM data, it has been concluded that the adsorption of TCNQ on Ag(100) is governed by a similar mechanism as that described above, i.e., a charge transfer-induced Ag-cyano coordination.

Further structural complexation is achieved by the synthesis of M-TCNQ coordination networks. The incorporation of metal coordination centers is an important strategy in supramolecular chemistry to produce more robust structures. More importantly, it introduces potential functionalities to supramolecular materials by integrating the electronic or magnetic properties of metal centers into metal-organic coordination structures. In this study, metal adatoms, including Mn, Fe, Co and Ni, are utilized in the fabrication of MTCNQ_x complexes on Cu(100) and Ag(100). On Cu(100), well-ordered MnTCNQ₂ domains have been synthesized with a domain size up to 30 nm in width. The networks are commensurate with the substrate lattice and exhibit organizational chirality due to the substrate confinement. The coordination networks formed by another metal, Fe adatoms, possess an identical coordination ratio, i.e., FeTCNQ₂. However, the domain size of FeTCNQ₂ is relatively small (~ 10 nm in width) and disordered Fe-TCNQ complexes cannot be fully eliminated. Furthermore, the Co- and Ni-TCNQ structures have been found to be poorly ordered. Such a growth behavior of Mn-, Fe-, Co- and Ni-TCNQ has been associated with the reactivity of different metals and their coordination geometry with cyano groups. On the other substrate, Ag(100), the growth phenomenon of MTCNQ_x (M = Mn, Ni and x = 1, 2, 4) coordination networks has been investigated. The x = 2 and 4 structures exhibit distinct chiral motifs and are nearly identical for the Mn and Ni metals. However, the two metals differ strongly in their x = 1 structures when all cyano groups of TCNQ are coordinated to metal atoms. This phenomenon has been partially explained by the limited molecular conformational freedom in the fully coordinated configuration. As fully coordinated, the metal-N bonds have little freedom to bend or stretch to adapt the substrate periodicity. Thus, a small variation in the local metal-N bond length could result in distinct structural ordering. The phase transition

from $x = 4$ to $x = 2$ networks exhibits a hierarchical self-assembly process which is driven by the relative metal concentration. The non-equivalent binding and adsorption sites of the metal centers in the $x = 2$ phase are evidenced by distinct topography features in the STM images. Furthermore, a comparison between the Ni-TCNQ structures on Cu(100) and Ag(100) shows the active role of substrates in altering the chemistry of the adsorbates and therefore affecting the ordering of Ni-TCNQ.

The magnetic properties of Mn-TCNQ and Ni-TCNQ coordination structures were investigated by XAS and XMCD measurements. For Mn centers, the sharp and rich multiplet features in the $L_{2,3}$ XAS and XMCD spectra indicate the dominant influence of the TCNQ coordination bonds to the electronic configuration of the Mn centers. The detailed XAS and XMCD lineshapes are correlated with the dark or bright contrasts observed in STM images. The Mn centers are found to be in the d^5 high-spin state and show paramagnetic behavior down to 8 K. Thus, the MnTCNQ_x networks represent ordered arrays of spin moments of $S = 5/2$. For Ni-TCNQ coordination networks, the Ni $L_{2,3}$ -edge spectra also indicate that the Ni centers are embedded in a robust crystal field environment induced by ligand coordination. Furthermore, magnetism of Ni is induced by the dehybridization of the Ni centers from the Ag substrate upon coordination to TCNQ, whereas the magnetic moment of Ni impurities on Ag(100) is nearly completely quenched.

This thesis shows a detailed investigation of TCNQ and M-TCNQ coordination networks on metal surfaces. The results give rise to several future investigations. The adsorption of TCNQ on metal surfaces is a model study of the interface between organic electron acceptors and metal films. The design of organic electronic devices consisting of a stacking of thin films requires such detailed understanding of the relevant chemical and physical processes occurring at metal-organic interfaces. Further studies extending these concepts into the third dimension should provide a deeper understanding of more realistic systems made of thicker organic films. The formation of M-TCNQ coordination structures is affected by the TCNQ-substrate coordination and thus represents a competition between the TCNQ-metal adatom and TCNQ-substrate interactions. These experiments demonstrate that multiple factors have to be considered for the molecular self-assembly on metal surfaces, especially the mutual interaction at the metal-organic interface. Continuing the exploration of metal-cyano coordination complexes on surfaces would be of great interest for the potential self-assembly phenomena and charge transfer induced effects. The distinct chemical reactivity of metal centers induced by surface interactions is another interesting subject which requires further experimental and theoretical

investigation. The metal centers might possess unique catalytic properties due to their unsaturated coordination numbers. Experiments utilizing inert or non-metal substrates would be also interesting for the study of reactions arising purely from metal-organic interactions and should provide further insight into the properties of bulk metal-TCNQ compounds. The chemical and physical properties emerging from the coordination of metal centers and organic molecules will provide design strategies in the fabrication of novel and functional materials. The ability to control the coordination structures on substrates offers the opportunity to prepare grids of metal atoms of potential importance for scientific studies and technological applications. The regular arrays of spin moments formed by nanometer-spaced metal centers serve as model systems for fundamental studies of single-spin phenomena or spin interactions. High density magnetic storage devices based on such metal grids have been envisioned and require the development of switchable and detectable MOCN systems. In addition to the experimental studies, theoretical analysis will provide a significant advancement in the understanding of both the structural and functional properties of the molecular self-assemblies. The power of 2D supramolecular chemistry allows the integration organic and inorganic materials into ordered nanostructures in a simple self-assembly process. With the interdisciplinary cooperation between chemistry and physics, the development of novel metal-organic materials of multiple properties has been envisioned.

Bibliography

- [1] J. M. Lehn, *Supramolecular Chemistry: Concepts and Perspectives*. VCH, Weinheim, Germany. 1995.
- [2] J. M. Lehn, *Supramolecular Chemistry - Scope and Perspectives Molecules, Supermolecules, and Molecular Devices (Nobel Lecture)*. *Angew. Chem. Int. Ed. Engl.* 1988, 27, 89.
- [3] S. Subramanian, M. J. Zaworotko, Exploitation of the hydrogen bond: recent developments in the context of crystal engineering. *Coord. Chem. Rev.* 1994, 137, 357-401.
- [4] L. J. Prins, D. N. Reinhoudt, P. Timmerman, Non-covalent synthesis using hydrogen bonding. *Angew. Chem. Int. Ed.* 2001, 40, 2382-2426.
- [5] D. Philp, J. F. Stoddart, Self-assembly in natural and unnatural systems. *Angew. Chem. Int. Ed.* 1996, 35, 1154-1196.
- [6] J. M. Lehn, Toward self-organization and complex matter. *Science* 2002, 295, 2400-2403.
- [7] M. W. Hosseini, Molecular tectonics: From simple tectons to complex molecular networks. *Acc. Chem. Rev.* 2005, 38, 313-323.
- [8] S. Kitagawa, R. Kitaura, S. Noro, Functional porous coordination polymers. *Angew. Chem. Int. Ed.* 2004, 43, 2334-2375.
- [9] O. M. Yaghi, M. O'Keeffe, N. W. Ockwig, H. K. Chae, M. Eddaoudi, J. Kim, Reticular synthesis and the design of new materials. *Nature* 2003, 423, 705-714.
- [10] B. Moulton, M. J. Zaworotko, From molecules to crystal engineering: Supramolecular isomerism and polymorphism in network solids. *Chem. Rev.* 2001, 101, 1629-1658.

- [11] Q. Chen, N. V. Richardson, Surface facetting induced by adsorbates. *Prog. Surf. Sci.* 2003, 73, 59-77.
- [12] M. Schunack, L. Petersen, A. Khnle, E. Lgsgaard, I. Stensgaard, I. Johannsen, F. Besenbacher, Anchoring of Organic Molecules to a Metal Surface: HtBDC on Cu(110). *Phys. Rev. Lett.* 2001, 86, 456-459.
- [13] D. P. Woodruff, The interface structure of n-alkylthiolate self-assembled monolayers on coinage metal surfaces. *Phys. Chem. Chem. Phys.* 2008, 10, 7211-7221.
- [14] T. C. Tseng, C. Urban, Y. Wang, R. Otero, S. L. Tait, M. Alcami, D. Ecija, M. Trelka, J. M. Gallego, N. Lin, M. Konuma, U. Starke, A. Nefedov, A. Langner, C. Wöll, M. A. Herranz, F. Martin, N. Martin, K. Kern, R. Miranda, Charge-transfer-induced structural rearrangements at both sides of organic/metal interfaces. *Nat. Chem.* 2010, 2, 374-379.
- [15] C. J. Pedersen, Cyclic Polyethers And Their Complexes With Metal Salts. *J. Am. Chem. Soc.* 1967, 89, 7017.
- [16] R. Sessoli, D. Gatteschi, A. Caneschi, M. A. Novak, Magnetic Bistability In A Metal-Ion Cluster. *Nature* 1993, 365, 141-143.
- [17] C. Kollmar, O. Kahn, Spin Polarization and Ferromagnetic Coupling in Metalloce-nium Charge-Transfer Complexes. *J. Chem. Phys.* 1992, 96, 2988-2997.
- [18] H. O. Stumpf, L. Ouahab, Y. Pei, D. Grandjean, O. Kahn, A Molecular-Based Mag-net With A Fully Interlocked 3-Dimensional Structure. *Science* 1993, 261, 447-449.
- [19] D. Maspoch, D. Ruiz-Molina, K. Wurst, N. Domingo, M. Cavallini, F. Biscarini, J. Tejada, C. Rovira, J. Veciana, A nanoporous molecular magnet with reversible solvent-induced mechanical and magnetic properties. *Nat. Mater.* 2003, 2, 190-195.
- [20] V. Madhavan, W. Chen, T. Jamneala, M. F. Crommie, N. S. Wingreen, Tunneling into a single magnetic atom: Spectroscopic evidence of the Kondo resonance. *Science* 1998, 280, 567-569.
- [21] B. C. Stipe, M. A. Rezaei, W. Ho, Single-molecule vibrational spectroscopy and microscopy. *Science* 1998, 280, 1732-1735.

- [22] D. M. Eigler, E. K. Schweizer, Positioning Single Atoms With A Scanning Tunneling Microscope. *Nature* 1990, 344, 524.
- [23] J. A. Stroschio, D. M. Eigler, Atomic And Molecular Manipulation With The Scanning Tunneling Microscope. *Science* 1991, 254, 1319.
- [24] T. A. Jung, R. R. Schlittler, J. K. Gimzewski, H. Tang, C. Joachim, Controlled Room-Temperature Positioning of Individual Molecules: Molecular Flexure and Motion. *Science* 1996, 271, 181.
- [25] C. F. Hirjibehedin, C. -Y. Lin, A. F. Otte, M. Ternes, C. P. Lutz, B. A. Jones, A. J. Heinrich, Large Magnetic Anisotropy of a Single Atomic Spin Embedded in a Surface Molecular Network. *Science* 2007, 317, 1199-1203.
- [26] J. V. Barth, G. Costantini, K. Kern, Engineering atomic and molecular nanostructures at surfaces. *Nature* 2005, 437, 671-679.
- [27] A. Khnle, Self-assembly of organic molecules at metal surfaces. *Curr. Opin. Colloid Interface Sci.* 2009, 14, 157-168
- [28] S. Stepanow, N. Lin, J. V. Barth, Modular assembly of low-dimensional coordination architectures on metal surfaces. *J. Phys.: Condens. Matter* 2008, 20, 184002.
- [29] J. V. Barth, J. Weckesser, N. Lin, S. Dmitriev, K. Kern, Supramolecular architectures and nanostructures at metal surfaces. *Appl. Phys. A* 2003, 76, 645.
- [30] S. De Feyter, F. C. De Schryver, Two-dimensional supramolecular self-assembly probed by scanning tunneling microscopy. *Chem. Soc. Rev.* 2003, 32, 139-150.
- [31] A. Langner, S. L. Tait, N. Lin, C. Rajadurai, M. Ruben, K. Kern, Self-recognition and self-selection in multicomponent supramolecular coordination networks on surfaces. *Proc. Natl. Acad. Sci. U. S. A.* 2007, 104, 17927-17930.
- [32] M. Ruben, J. Rojo, F. J. Romero-Salguero, L. H. Uppadine, J. M. Lehn, Grid-type metal ion architectures: Functional metallosupramolecular arrays. *Angew. Chem. Int. Ed.* 2004, 43, 3644-3662.
- [33] T. L. Cairns, R. A. Carboni, D. D. Coffman, V. A. Engelhardt, R. E. Heckert, E. L. Little, E. G. McGeer, B. C. McKusick, W. J. Middleton, R. M. Scribner, C. W.

- Theobald, H. E. Winberg, Cyanocarbon Chemistry. I. Preparation and Reactions of Tetracyanoethylene. *J. Am. Chem. Soc.* 1958, 80, 2275.
- [34] D. S. Acker, W. R. Hertler, Substituted Quinodimethans. I. Preparation and Chemistry of 7,7,8,8-Tetracyanoquinodimethan. *J. Am. Chem. Soc.* 1962, 84, 3370.
- [35] J. Ferraris, D. O. Cowan, V. Walatka, Jr., J. H. Perlstein, Electron-Transfer In A New Highly Conducting Donor-Acceptor Complex. *J. Am. Chem. Soc.* 1973, 95, 948.
- [36] R. Jain, K. Kabir, J. B. Gilroy, K. A. R. Mitchell, K. C. Wong, R. G. Hicks, High-temperature metal-organic magnets. *Nature* 2007, 445, 291.
- [37] J. S. Miller, J. C. Calabrese, A. J. Epstein, R. W. Bigelow, J. H. Zhang, W. M. Reiff, Ferromagnetic Properties of One-dimensional Decamethylferrocenium Tetracyanoethylenide (1 : 1): $[\text{Fe}(\eta^5\text{-C}_5\text{Me}_5)_2]^{\bullet+}\text{TCNE}^{\bullet-}$. *J. Chem. Soc., Chem. Commun.* 1986, 13, 1026.
- [38] P. J. Kunkeler, P. J. van Koningsbruggen, J. P. Cornelissen, A. N. van der Horst, A. M. van der Kraan, A. L. Spek, J. G. Haasnoot, J. Reedijk, Novel Hybrid Spin Systems of 7,7',8,8'-Tetracyanoquinodimethane (TCNQ) Radical Anions and 4-Amino-3,5-bis(pyridin-2-yl)-1,2,4-triazole (abpt). Crystal Structure of $[\text{Fe}(\text{abpt})_2(\text{TCNQ})_2]$ at 298 and 100 K, Mössbauer Spectroscopy, Magnetic Properties, and Infrared Spectroscopy of the Series $[\text{M}^{\text{II}}(\text{abpt})_2(\text{TCNQ})_2]$ ($\text{M} = \text{Mn}, \text{Fe}, \text{Co}, \text{Ni}, \text{Cu}, \text{Zn}$). *J. Am. Chem. Soc.* 1996, 118, 2190.
- [39] R. Clerac, S. O'Kane, J. Cowen, X. Ouyang, R. Heintz, H. Zhao, M. J. Bazile, Jr., K. R. Dunbar, Glassy magnets composed of metals coordinated to 7,7,8,8-tetracyanoquinodimethane: $\text{M}(\text{TCNQ})_2$ ($\text{M} = \text{Mn}, \text{Fe}, \text{Co}, \text{Ni}$). *Chem. Mater.* 2003, 15, 1840.
- [40] E. B. Vickers, I. D. Giles, J. S. Miller, $\text{M}[\text{TCNQ}]_y$ -based magnets ($\text{M} = \text{Mn}, \text{Fe}, \text{Co}, \text{Ni}$; $\text{TCNQ} = 7,7,8,8$ -tetracyano-p-quinodimethane). *Chem. Mater.* 2005, 17, 1667.
- [41] K. I. Pokhodnya, M. Bonner, J. H. Her, P. W. Stephens, J. S. Miller, Magnetic ordering ($T_c = 90 \text{ K}$) observed for layered $[\text{Fe}^{\text{II}}(\text{TCNE}^{\bullet-})(\text{NCMe})_2]^+ [\text{Fe}^{\text{III}}\text{Cl}_4]^-$ ($\text{TCNE} = \text{tetracyanoethylene}$). *J. Am. Chem. Soc.* 2006, 128, 15592.
- [42] K. I. Pokhodnya, A. J. Epstein, J. S. Miller, Thin-film $\text{V}[\text{TCNE}]_x$ magnets. *Adv. Mater.* 2000, 12, 410.

- [43] J. M. Manriquez, G. T. Yee, R. S. McLean, A. J. Epstein, J. S. Miller, A Room-Temperature Molecular Organic Based Magnet. *Science* 1991, 252, 1415.
- [44] B. Milián, R. Pou-Amérigo, R. Viruela, E. Ortí, A theoretical study of neutral and reduced tetracyano-p-quinodimethane (TCNQ). *J. Mol. Struct.* 2004, 709, 97-102.
- [45] G. Binnig, H. Rohrer, C. Gerber, E. Weibel, Tunneling through a Controllable Vacuum Gap. *Appl. Phys. Lett.* 1982, 40, 178-180.
- [46] N. D. Lang, Spectroscopy of Single Atoms in the Scanning Tunneling Microscope. *Phys. Rev. B* 1986, 34, 5947-5950.
- [47] N. D. Lang, Vacuum Tunneling Current from an Adsorbed Atom. *Phys. Rev. Lett.* 1985, 55, 230-233.
- [48] P. K. Hansma, J. Tersoff, Scanning Tunneling Microscopy. *J. Appl. Phys.* 1987, 61, 1-23.
- [49] J. Tersoff, D. R. Hamann, Theory and Application for the Scanning Tunneling Microscope. *Phys. Rev. Lett.* 1983, 50, 1998-2001.
- [50] D. A. Shirley, High-Resolution X-Ray Photoemission Spectrum of the Valence Bands of Gold. *Phys. Rev. B* 1972, 5, 4709-4714.
- [51] S. Hfner, Photoelectron Spectroscopy: Principles and Applications. Springer, 2003.
- [52] J. Stöhr, NEXAFS Spectroscopy. Springer-Verlag. 2003.
- [53] G. Hähner, Near edge X-ray absorption fine structure spectroscopy as a tool to probe electronic and structural properties of thin organic films and liquids. *Chem. Soc. Rev.* 2006, 35, 1244-1255.
- [54] D. A. Outka, J. Stöhr, Curve fitting analysis of near-edge core excitationspectra of free, adsorbed, and polymeric molecules. *J. Chem. Phys.* 1988, 88, 3539-3554.
- [55] J. Stöhr, D. A. Outka, Determination of molecular orientations on surfaces from the angular dependence of near-edge X-ray-absorption fine-structure spectra. *Phys. Rev. B* 1987, 36, 7891-1905.

- [56] A. P. Hitchcock, C. E. Brion, Carbon K-Shell Excitation of C_2H_2, C_2H_4, C_2H_6 and C_6H_6 by 2.5 keV Electron-Impact. *J. Electron. Spectrosc. Relat. Phenom.* 1977, 10, 317-330.
- [57] P. A. Stevens, R. J. Madix, J. Stöhr, The Bonding of Acetonitrile and CH_3CN on Ag(110) Determined by Near Edge X-Ray Absorption Fine Structure: Evidence for π -Donor Bonding and Azimuthal Ordering. *J. Chem. Phys.* 1989, 91, 4338-4345.
- [58] B. T. Thole, P. Carra, F. Sette, and G. van der Laan, X-ray circular dichroism as a probe of orbital magnetization. *Phys. Rev. Lett.* 1992, 68, 1943-1946.
- [59] P. Carra, B. T. Thole, M. Altarelli, and X. Wang, X-ray circular dichroism and local magnetic fields. *Phys. Rev. Lett.* 1993, 70, 694-397.
- [60] C. T. Chen, Y. U. Idzerda, H.-J. Lin, N. V. Smith, G. Meigs, E. Chaban, G. H. Ho, E. Pellegrin, and F. Sette, Experimental Confirmation of the X-Ray Magnetic Circular Dichroism Sum Rules for Iron and Cobalt. *Phys. Rev. Lett.* 1995, 75, 152-155.
- [61] G. Schütz, W. Wagner, W. Wilhelm, P. Kienle, R. Zeller, R. Frahm, G. Materlik, Absorption of Circularly Polarized X Rays in Iron. *Phys. Rev. Lett.* 1987, 58, 737-740.
- [62] J. Stöhr, Exploring the microscopic origin of magnetic anisotropies with X-ray magnetic circular dichroism (XMCD) spectroscopy. *J. Mag. Mag. Mater.* 1999, 200, 470-497.
- [63] S. Stepanow, Low-Dimensional Supramolecular Architectures at Metal Surfaces. 2005, PhD thesis, Ecole Polytechnique Fédérale de Lausanne (EPFL), Switzerland.
- [64] S. R. Forrest, The path to ubiquitous and low-cost organic electronic appliances on plastic. *Nature* 2004, 428, 911.
- [65] E. Moons, Conjugated polymer blends: linking film morphology to performance of light emitting diodes and photodiodes. *J. Phys. Condens. Matter.* 2002, 14, 12235-12260.
- [66] F. Cicoira, C. Santato, Organic light emitting field effect transistors: advances and perspectives. *Adv. Funct. Mater.* 2007, 17, 3421-3434.
- [67] P. W. M. Blom, V. D. Mihailetchi, L. J. A. Koster, D. E. Markov, Device physics of polymer: fullerene bulk heterojunction solar cells. *Adv. Mater.* 2007, 19, 1551-1566.

- [68] C. J. Brabec, N. S. Sariciftci, J. C. Hummelen, Plastic solar cells. *Adv. Funct. Mater.* 2001, 11, 15-26.
- [69] D. Jérôme, Organic conductors: from charge density wave TTF-TCNQ to superconducting TMTSF₂PF₆. *Chem. Rev.* 104, 5565-5591 (2004).
- [70] D. Haskel, Z. Islam, J. Lang, C. Kmety, G. Srajer, K. I. Pokhodnya, A. J. Epstein, J. S. Miller, Local structural order in the disordered vanadium tetracyanoethylene room-temperature molecule-based magnet. *Phys. Rev. B* 70, 2004, 054422.
- [71] P. Gambardella, S. Stepanow, A. Dmitriev, J. Honolka, F. M. F. de Groot, M. Lingenfelder, S. S. Gupta, D. D. Sarma, P. Bencok, S. Stanescu, S. Clair, S. Pons, N. Lin, A. P. Steitsonen, H. Brune, J. V. Barth, K. Kern, Supramolecular control of the magnetic anisotropy in two-dimensional high-spin Fe arrays at a metal interface. *Nat. Mater.* 2009, 8, 189-193.
- [72] X. -Y. Zhu, Electronic structure and electron dynamics at molecule-metal interfaces: implications for molecule based electronics. *Surf. Sci. Rep.* 2004, 56, 1-83.
- [73] C. D. Lindstrom, X. -Y. Zhu, Photoinduced electron transfer at molecule-metal interfaces. *Chem. Rev.* 2006, 106, 4281-4300.
- [74] R. Otero, D. Ecija, G. Fernandez, J. M. Gallego, L. Sanchez, N. Martin, R. Miranda, An organic donor/acceptor lateral superlattice at the nanoscale. *Nano Lett.* 2007, 7, 2602-2607.
- [75] L. Wang, W. Chen, S. W. Thye, A. Charge-transfer across the molecule/metal interface using the core hole clock technique. *Surf. Sci. Rep.* 2008, 63, 465-386.
- [76] H. Ishii, K. Sugiyama, E. Ito, K. Seki, Energy level alignment and interfacial electronic structures at organic/metal and organic/organic interfaces. *Adv. Mater.* 1999, 11, 605-625.
- [77] X. Crispin, V. Geskin, A. Crispin, J. Cornil, R. Lazzaroni, W. R. Salaneck, J. L. Bredas, Characterization of the interface dipole at organic/metal interfaces. *J. Am. Chem. Soc.* 2002, 124, 8131-8141.
- [78] N. Koch, S. Duhm, J. P. Rabe, A. Vollmer, R. L. Johnson, Optimized hole injection with strong electron acceptors at organic-metal interfaces. *Phys. Rev. Lett.* 2005, 95, 237601.

- [79] G. Witte, S. Lukas, P. S. Bagus, C. Wöll, Vacuum level alignment at organic/metal junctions: "cushion" effect and the interface dipole. *Appl. Phys. Lett.* 2005, 87, 263502.
- [80] S. Braun, W. R. Salaneck, Fermi level pinning at interfaces with tetrafluorotetracyanoquinodimethane (F4-TCNQ): the role of integer charge transfer states. *Chem. Phys. Lett.* 2007, 438, 259-262.
- [81] L. Romaner, G. Heimel, J. L. Bredas, A. Gerlach, F. Schreiber, R. L. Johnson, J. Zegenhagen, S. Duhm, N. Koch, E. Zojer, Impact of bidirectional charge transfer and molecular distortions on the electronic structure of a metal-organic interface. *Phys. Rev. Lett.* 2007, 99, 256801.
- [82] S. Bedwani, D. Wegner, M. F. Crommie, A. Rochefort, Strongly reshaped organic-metal interfaces: tetracyanoethylene on Cu(100). *Phys. Rev. Lett.* 2008, 101, 216105.
- [83] J. B. Torrance, The difference between metallic and insulating salts of tetracyanoquinodimethane (TCNQ): how to design an organic metal. *Acc. Chem. Res.* 1979, 12, 79-86.
- [84] W. Kaim, M. Moscherosch, The coordination chemistry of TCNE, TCNQ and related polynitrile π acceptors. *Coord. Chem. Rev.* 1994, 129, 157-193.
- [85] D. Wegner, R. Yamachika, Y. Wang, V. W. Brar, B. M. Bartlett, J. R. Long, M. F. Crommie, Single-molecule charge transfer and bonding at an organic/inorganic interface: Tetracyanoethylene on noble metals. *Nano Lett.* 2008, 8, 131-135.
- [86] M. M. Kamna, T. M. Graham, J. C. Love, P. S. Weiss, Strong electronic perturbation of the Cu(111) surface by 7,7',8,8'-tetracyanoquinodimethane. *Surf. Sci.* 1998, 419, 12-23.
- [87] I. Fernández-Torrente, K. J. Franke, J. I. Pascual, Structure and electronic configuration of tetracyanoquinodimethane layers on a Au(111) surface. *Int. J. Mass Spectrosc.* 2008, 277, 269-273.
- [88] H. T. Jonkman, G. A. van der Velde, W. C. Nieuwpoort, Ab Initio SCF MO Calculation of Ionisation Energies and Charge Distributions of TCNQ and Its Mono- and Divalent anions. *Chem. Phys. Lett.* 1973, 25, 62-65.

- [89] J. M. Lindquist, J. C. Hemminger, High-Resolution Core Level Photoelectron Spectra of Solid TCNQ: Determination of Molecular Orbital Spatial Distribution from Localized Shake-up Features. *J. Phys. Chem.* 1988, 92, 1394-1396.
- [90] J. M. Lindquist, J. C. Hemminger, High-Energy Resolution X-ray Photoelectron Spectroscopy Studies of Tetracyanoquinodimethane Charge-Transfer Complexes with Copper, Nickel, and Lithium. *Chem. Mater.* 1989, 1, 72-78.
- [91] J. Giergiel, S. Wells, T. A. Land, J. C. Hemminger, Growth and chemistry of TCNQ films on nickel (111). *Surf. Sci.* 1991, 255, 31-40.
- [92] S. K. Wells, J. Giergiel, T. A. Land, J. M. Lindquist, J. C. Hemminger, Beam-induced modifications of TCNQ multilayers. *Surf. Sci.* 1991, 257, 129-145.
- [93] J. Fraxedas, J. Caro, A. Figuerasc, P. Gorostiza, F. Sanz, Surface characterization of thin films of tetrathiofulvalene 7,7,8,8-tetracyano-p-quinodimethane evaporated on NaCl(001). *J. Vac. Sci. Technol. A* 1998, 16, 2517-2523.
- [94] M. Higo, T. Futagawa, M. Mitsushio, T. Yoshidome, Y. Ozono, Adsorption State and Morphology of Tetracyanoquinodimethane Deposited from Solution onto the Atomically Smooth Native Oxide Surface of Al(111) Films Studied by X-ray Photoelectron Spectroscopy and Atomic Force Microscopy. *J. Phys. Chem. B* 2003, 107, 5871-5876.
- [95] W. D. Grobman, R. A. Pollak, D. E. Eastman, E. T. Maas, Jr., B. A. Scott, Valence Electronic Structure and Charge Transfer in Tetrathiofulvalinium Tetracyanoquinodimethane (TTF-TCNQ) from Photoemission Spectroscopy. *Phys. Rev. Lett.* 1974, 32, 534-537.
- [96] W. D. Grobman, B. D. Silverman, Intramolecular screening of crystal fields and the x-ray photoemission determination of charge transfer in TTF-TCNQ. *Solid State Commun.* 1976, 19, 319-322.
- [97] T. Patterson, J. Pankow, N. R. Armstrong, Tetracyanoquinodimethane Thin Films on Cu, Au, Pt, and SnS₂: Characterization by X-ray Photoelectron Spectroscopy. *Langmuir* 1991, 7, 3160-3166.
- [98] K. Xiao, I. N. Ivanov, A. A. Puztzy, Z. Liu, D. B. Geohegan, Directed Integration of Tetracyanoquinodimethane-Cu Organic Nanowires into Prefabricated Device Architectures. *Adv. Mater.* 2006, 18, 2184-2188.

- [99] R. Müller, S. De Jonge, K. Myny, D. J. Wouters, J. Genoe, P. Heremans, Organic CuTCNQ integrated in complementary metal oxide semiconductor copper back end-of-line for nonvolatile memories. *Appl. Phys. Lett.* 2006, 89, 223501.
- [100] P. Liu, Y. Jiang, H. Xie, F. Guo, J. Li, Diffusion Mechanism in Ag/TCNQ Thin Films with Cu as Tracers. *Jpn. J. Appl. Phys.* 2005, 44, 494-496.
- [101] D. Jérôme, H. J. Schulz, Organic conductors and superconductors. *Adv. Phys.* 1982, 31, 299-490.
- [102] W. R. Hertler, W. Mahler, L. R. Melby, J. S. Miller, R. E. Putscher, O. W. Webster, Cyanocarbons - Their History From Conducting To Magnetic Organic Charge-Transfer Salts. *Mol. Cryst. Liq. Cryst.* 1989, 171, 205-216.
- [103] H. Alves, A. S. Molinari, H. X. Xie, A. F. Morpurgo, Metallic conduction at organic charge transfer interfaces. *Nat. Mater.* 2008, 7, 574-580.
- [104] S. Ferlay, T. Mallah, R. Ouahes, P. Veillet, M. Verdager, A Room-Temperature Organometallic Magnet Based on Prussian Blue. *Nature* 1995, 378, 701-703.
- [105] M. F. Calhoun, J. Sanchez, D. Olaya, M. E. Gershenson, V. Podzorov, Electronic functionalization of the surface of organic semiconductors with self-assembled monolayers. *Nat. Mater.* 2008, 7, 84-89.
- [106] T. Nakayama, K. Inamura, Y. Inoue, S. Ikeda, Adsorption of benzonitrile and alkyl cyanides on evaporated nickel and palladium films studied by XPS. *Surf. Sci.* 1987, 179, 47-58.
- [107] B. A. Sexton, N. R. Avery, Coordination of Acetonitrile (CH_3CN) to Platinum (111): Evidence for an $\eta_2(\text{C}, \text{N})$ Species. *Surf. Sci.* 1983, 129, 21-36.
- [108] J. L. Solomon, R. J. Madix, J. Stöhr, Orientation and Absolute Coverage of Benzene, Aniline, and Phenol on Ag(110) Determined by NEXAFS and XPS. *Surf. Sci.* 1991, 255, 12-30.
- [109] G. Iucci, V. Caravetta, P. Altamura, M. V. Russo, G. Paolucci, A. Goldoni, G. Polzonetti, XPS, NEXAFS and theoretical study of phenylacetylene adsorbed on Cu(100). *Chem. Phys.* 2004, 302, 43-52.

- [110] M. Bässler, R. Fink, C. Buchbeger, P. Väterlein, M. Jung, E. Umbach, Near edge X-ray absorption fine structure resonances of quinoide molecules. *Langmuir* 2000, 16, 6674-6681.
- [111] M. Sing, J. Meyer, M. Hoinkis, S. Glawion, P. Blaha, G. Gavrila, C. S. Jacobsen, R. Claessen, Structural versus electronic origin of renormalized band widths in TTF-TCNQ: an angular dependent NEXAFS study. *Phys. Rev. B* 2007, 76, 245119.
- [112] J. Fraxedas, Y. J. Lee, I. Jiménez, R. Gago, R. M. Nieminen, P. Ordejón, E. Canadell, Characterization of the unoccupied and partially occupied states of TTF-TCNQ by XANES and first-principles calculations. *Phys. Rev. B* 2003, 68, 195115.
- [113] J. Somers, M. E. Kordesch, T. Lindner, H. Conrad, A. M. Bradshaw, G. P. Williams, An adsorbed diatomic molecule showing parallel bonding: CN/Pd(111). *Surf. Sci.* 1987, 188, 693-700.
- [114] K. Kern, H. Niehus, A. Schatz, P. Zeppenfeld, J. Goerge, G. Comsa, Long-range spatial self-organization in the adsorbate-induced restructuring of surfaces: Cu110-(2 x 1)O. *Phys. Rev. Lett.* 1991, 67, 855-858.
- [115] P. Zeppenfeld, M. Krzyzowski, C. Romainczyk, G. Comsa, M. G. Lagally, Size relation for surface systems with long-range interactions. *Phys. Rev. Lett.* 1994, 72, 2737-2740.
- [116] G. Prevot, B. Croset, Y. Girard, A. Coati, Y. Garreau, M. Hohage, L. D. Sun, P. Zeppenfeld, Elastic origin of the O/Cu(110) self-ordering evidenced by GIXD. *Surf. Sci.* 2004, 549, 52-56.
- [117] J. V. Barth, J. Weckesser, N. Lin, A. Dmitriev, K. Kern, Supramolecular architectures and nanostructures at metal surfaces. *Appl. Phys. A* 2003, 76, 645-652.
- [118] J. S. Miller, Magnetically ordered molecule-based assemblies. *Dalton Trans.* 2006, 23, 2742-2749.
- [119] E. J. Schelter, F. Karadas, C. Avendano, A. V. Prosvirin, W. Wernsdorfer, K. R. Dunbar, A family of mixed-metal cyanide cubes with alternating octahedral and tetrahedral corners exhibiting a variety of magnetic behaviors including single molecule magnetism. *J. Am. Chem. Soc.* 2007, 129, 8139-8149.

- [120] S. Stepanow, N. Lin, D. Payer, U. Schlickum, F. Klappenberger, G. Zoppellaro, M. Ruben, H. Brune, J. V. Barth, K. Kern, Surface-Assisted Assembly of 2D Metal-Organic Networks That Exhibit Unusual Threefold Coordination Symmetry. *Angew. Chem. Int. Ed.* 2007, 46, 710-713.
- [121] U. Schlickum, R. Decker, F. Klappenberger, G. Zoppellaro, S. Klyatskaya, M. Ruben, I. Silanes, A. Arnau, K. Kern, H. Brune, J. V. Barth, Metal-Organic Honeycomb Nanomeshes with Tunable Cavity Size. 2007, 7, 3813-3817.
- [122] S. Stepanow, N. Lin, J. V. Barth, K. Kern, Surface-Template Assembly of Two-Dimensional Metal-Organic Coordination Networks. *J. Phys. Chem. B* 2006, 110, 23472-23477.
- [123] N. Lin, S. Stepanow, F. Vidal, J. V. Barth, K. Kern, Manipulating 2D metal-organic networks via ligand control. *Chem. Commun.* 2005, 1681-1683.
- [124] S. L. Tait, A. Langner, N. Lin, S. Stepanow, C. Rajadurai, M. Ruben, K. Kern, One-Dimensional Self-Assembled Molecular Chains on Cu(100): Interplay between Surface-Assisted Coordination Chemistry and Substrate Commensurability. *J. Phys. Chem. C* 2007, 111, 10982-10987.
- [125] D. Heim, D. Ećija, K. Seufert, W. Auwärter, C. Aurisicchio, C. Fabbro, D. Bonifazi, J. V. Barth, Self-Assembly of Flexible One-Dimensional Coordination Polymers on Metal Surfaces. *J. Am. Chem. Soc.* 2010, 132, 6783-6790.
- [126] C. H. Gorbitz, H. P. Hersleth, On the inclusion of solvent molecules in the crystal structures of organic compounds. *Acta. Cryst. B* 2000, 56, 526-534.
- [127] H. Miyasaka, C. S. Campos-Fernandez, R. Clerac, K. R. Dunbar, Hexagonal layered materials composed of $M_2(O_2CCF_3)_4$ ($M = Ru$ and Rh) donors and TCNQ acceptors. *Angew. Chem. Int. Ed.* 2000, 39, 3831.
- [128] H. Miyasaka, T. Izawa, N. Takahashi, M. Yamashita, K. R. Dunbar, Long-range ordered magnet of a charge-transfer Ru_2^{4+} /TCNQ two-dimensional network compound. *J. Am. Chem. Soc.* 2006, 128, 11358.
- [129] N. Lopez, H. Zhao, A. V. Prosvirin, A. Chouai, M. Shatruk, K. R. Dunbar, Conversion of a porous material based on a Mn^{II} -TCNQF₄ honeycomb net to a molecular magnet upon desolvation. *Chem. Commun.* 2007, 4611.

- [130] H. Miyasaka, N. Motokawa, S. Matsunaga, M. Yamashita, K. Sugimoto, T. Mori, N. Toyota, K. R. Dunbar, Control of Charge Transfer in a Series of Ru-2(II,II)/TCNQ Two-Dimensional Networks by Tuning the Electron Affinity of TCNQ Units: A Route to Synergistic Magnetic/Conducting Materials. *J. Am. Chem. Soc.* 2010, 132, 1532.
- [131] K. R. Dunbar, R. A. Heintz, Progress in inorganic chemistry, Vol. 45 (1997): Chemistry of transition metal cyanide compounds: Modern perspectives.
- [132] H. Zhao, R. A. Heintz, X. Ouyang, K. R. Dunbar, C. F. Campana, R. D. Rogers, Spectroscopic, thermal, and magnetic properties of metal/TCNQ network polymers with extensive supramolecular interactions between layers. *Chem. Mater.* 1999, 11, 736-746.
- [133] L. Z. Chen, J. M. Miller, Ion-Molecule Reactions of Alkanenitriles and Transition-Metal Ions in the Gas Phase: A Study on Fragmentation Mechanism of the Adducts. *J. Am. Soc. Mass. Spectrom.* 1991, 2, 120-124.
- [134] L. Z. Chen, J. M. Miller, Ion-Molecule Reactions of Transition-Metal Ions with Nitriles in the Gas Phase: Competitive Formation of Both End-On and Side-On coordination. *Can. J. Chem.* 1991, 69, 2002-2007.
- [135] L. Z. Chen, J. M. Miller, Fragmentation of Ion-Molecule Adducts of Transition Metal Ions with Aromatic Ring-containing Nitriles in the Gas Phase. *Org. Mass. Spectro.* 1991, 69, 19-26.
- [136] R. M. Stepnowski, J. Allison, Gas Phase Chemistry of First-Row Transition-Metal- and Metal-Containing Ions with Alkyl Cyanides. *Organometallics* 1988, 7, 2097-2103.
- [137] C. B. Lebrilla, C. Schulze, H. Schwarz, The Reaction of Nitriles and Fe⁺ in the Gas Phase. A Case of Remote Functionalization. *J. Am. Chem. Soc.* 1987, 109, 98-100.
- [138] M. A. Lingenfelder, H. Spillmann, A. Dmitriev, S. Stepanow, N. Lin, J. V. Barth, K. Kern, Towards surface-supported supramolecular architectures: tailored coordination assembly of 1,4-benzenedicarboxylate and Fe on Cu(100). *Chem. Eur. J.* 2004, 10, 1913-1919.
- [139] A. Dmitriev, H. Spillmann, M. Lingenfelder, N. Lin, J. V. Barth, K. Kern, Design of extended surface-supported chiral metal-organic arrays comprising mononuclear iron centers. *Langmuir* 2004, 20, 4799-4801.

- [140] H. Spillmann, A. Dmitriev, N. Lin, P. Messina, J. V. Barth, K. Kern, Hierarchical assembly of two-dimensional homochiral nanocavity arrays. *J. Am. Chem. Soc.* 2003, 125, 10725-10728.
- [141] R. A. Heintz, H. Zhao, X. Ouyang, G. Grandinetti, J. Cowen, K. R. Dunbar, New insight into the nature of Cu(TCNQ): Solution routes to two distinct polymorphs and their relationship to crystalline films that display bistable switching behavior. *Inorg. Chem.* 1999, 38, 144-156.
- [142] T. C. Tseng, C. S. Lin, X. Q. Shi, S. L. Tait, X. Liu, U. Starke, N. Lin, R. Q. Zhang, C. Minot, M. A. Van Hove, J. I. Cerda, K. Kern, Two-dimensional metal-organic coordination networks of Mn-7,7,8,8-tetracyanoquinodimethane assembled on Cu(100): Structural, electronic, and magnetic properties. *Phys. Rev. B* 2009, 80, 155458.
- [143] D. Wegner, R. Yamachika, X. W. Zhang, Y. Y. Wang, T. Baruah, M. R. Pederson, B. M. Bartlett, J. R. Long, M. F. Crommie, Tuning Molecule-Mediated Spin Coupling in Bottom-Up-Fabricated Vanadium-Tetracyanoethylene Nanostructures. *Phys. Rev. Lett.* 2009, 103, 087205.
- [144] J. P. Cornelissen, J. H. van Diemen, L. R. Groeneveld, J. G. Haasnoot, A. L. Spek, J. Reedijk, Synthesis and Properties of Isostructural Transition-Metal (Copper, Nickel, Cobalt, And Iron) Compounds With 7,7',8,8'-Tetracyanoquinodimethanide(1-) in an Unusual Monodentate Coordination Mode. Crystal-Structure Of Bis(3,5-bis(pyridin-2-yl)-4-amino-1,2,4-triazole)bis(7,7',8,8'-tetracyanoquinodimethanido)Copper(II). *Inorg. Chem.* 1992, 31, 198-202.
- [145] H. Oshio, E. Ino, I. Mogi, T. Ito, A Weak Antiferromagnetic Interaction between Mn_{2+} Centers through a TCNQ Column: Crystal Structures and Magnetic Properties of $[Mn_{II}(tpa)(\mu-O_2CCH_3)]_2(TCNQ)_2 \cdot 2CH_3CN$, and $[Mn_{II}(tpa)(NCS)_2] \cdot CH_3CN$ ($tpa = \text{Tris}(2\text{-pyridylmethyl})\text{amine}$). *Inorg. Chem.* 1993, 32, 5697-5703.
- [146] H. Zhao, M. J. Bazile, J. R. Galan-Mascaros, K. R. Dunbar, A rare-earth metal TCNQ magnet: Synthesis, structure, and magnetic properties of $[Gd_2(TCNQ)_5(H_2O)_9][Gd(TCNQ)_4(H_2O)_3] \cdot 4H_2O$. *Angew. Chem. Int. Ed.* 2003, 42, 1015-1018.

- [147] S. Shimomura, R. Matsuda, T. Tsujino, T. Kawamura, S. Kitagawa, TCNQ dianion-based coordination polymer whose open framework shows charge-transfer type guest inclusion. *J. Am. Chem. Soc.* 2006, 128, 16416-16417.
- [148] N. Uyeda, T. Kobayashi, K. Ishizuka, Y. Fujiyoshi, H. Inokuchi, G. Saito, Direct Molecular Imaging Of Low Dimensional Solids By High Resolution Electron Microscopy. *Mol. Cryst. Liq. Cryst.* 1985, 125, 103-112.
- [149] J. Zhang, J. Ensling, V. Ksenofontov, P. Gütlich, A. J. Epstein, J. S. Miller, $[\text{Mn}_{\text{II}}(\text{tcne})_2] \cdot x\text{CH}_2\text{Cl}_2$ ($\text{M} = \text{Mn}, \text{Fe}, \text{Co}, \text{Ni}$) molecule-based magnets with T_c values above 100 K and coercive fields up to 6500 Oe. *Angew. Chem. Int. Ed.* 1998, 37, 657-660.
- [150] L. Bartels, Tailoring molecular layers at metal surfaces. *Nat. Chem.* 2010, 517, 87.
- [151] G. van der Laan, B. T. Thole, Strong magnetic x-ray dichroism in 2p absorption spectra of 3d transition-metal ions. *Phys. Rev. B* 1991, 43, 13401-13411.
- [152] Y. Huttel, C. M. Teodorescu, F. Bertran, G. Krill, Experimental evidence of long-range magnetic order in the $c(2 \times 2)$ MnCu(100) surface alloy. *Phys. Rev. B* 2001, 64, 094405.
- [153] P. Gambardella, S. S. Dhesi, S. Gardonio, C. Grazioli, P. Ohresser, C. Carbone, Localized Magnetic States of Fe, Co, and Ni Impurities on ALkali Metal Films. *Phys. Rev. Lett.* 2002, 88, 047202.
- [154] T. Jo, G. A. Sawatzky, Ground state of ferromagnetic nickel and magnetic circular dichroism in Ni 2p core x-ray-absorption spectroscopy. *Phys. Rev. B* 1991, 43, 8771-8774.
- [155] G. van der Laan, B. T. Thole, Electronic correlations in Ni 2p and 3p magnetic x-ray dichroism and x-ray photoemission of ferromagnetic nickel. *J. Phys.: Condens. Matter* 1992, 4, 4181-4188.
- [156] C. T. Chen, F. Sette, Y. Ma, S. Modesti, Soft-x-ray magnetic circular dichroism at the $L_{2,3}$ edges of nickel. *Phys. Rev. B* 1990, 42, 7262-7265.
- [157] C. T. Chen, N. V. Smith, F. Sette, Exchange, spin-orbit, and correlation effects in the soft-x-ray magnetic-circular-dichroism spectrum of nickel. *Phys. Rev. B* 1991, 43, 6785-6787.

- [158] W. S. Yoon, M. Balasubramanian, K. Y. Chung, X. Q. Yang, J. McBreen, C. P. Grey, D. A. Fischer, Investigation of the Charge Compensation Mechanism on the Electrochemically Li-Ion Deintercalated $\text{Li}_{1-x}\text{Co}_{1/3}\text{Ni}_{1/3}\text{Mn}_{1/3}\text{O}_2$ Electrode System by Combination of Soft and Hard X-ray Absorption Spectroscopy. *J. Am. Chem. Soc.* 2005, 127, 17479-17487.

Publications

Two-dimensional metal-organic coordination networks of

Mn-7,7,8,8-tetracyanoquinodimethane assembled on Cu(100): Structural, electronic, and magnetic properties

T. C. Tseng, C. Lin, X. Shi, S. L. Tait, X. Liu, U. Starke, N. Lin, R. Zhang, C. Minot, M. A. Van Hove, J. I. Cerd, K. Kern

Phys. Rev. B 2009, 80, 155458.

Charge-transfer-induced structural rearrangements at both sides of organic/metal interfaces

T. C. Tseng, C. Urban, Y. Wang, R. Otero, S. L. Tait, M. Alcamí, D. Eciija, M. Trelka, J. M. Gallego, N. Lin, M. Konuma, U. Starke, A. Nefedov, A. Langner, C. Wöll, M. A. Herranz, F. Martin, N. Martin, K. Kern, R. Miranda

Nat. Chem. 2010, 2, 374-379.

Structural analysis and electronic properties of negatively charged TCNQ: 2D networks of (TCNQ)₂Mn assembled on Cu(100)

X. Q. Shi, C. Lin, C. Minot, T. C. Tseng, S. L. Tait, N. Lin, R.Q. Zhang, K. Kern, J. I. Cerd, M. A. Van Hove

submitted

Spin and Orbital Magnetic Moment Anisotropies of Monodispersed

Bis(Phthalocyaninato)Terbium on a Copper Surface

S. Stepanow, J. Honolka, P. Gambardella, L. Vitali, N. Abdurakhmanova, T. C. Tseng, S. Rauschenbach, S. L. Tait, V. Sessi, S. Klyatskaya, S. Brink, M. Ruben, K. Kern

submitted

Two-dimensional metal-organic coordination networks of Mn- and Ni-TCNQ_x (x = 1, 2, 4) self-assembled on Ag(100)

T. C. Tseng, N. Abdurakhmanova, S. Stepanow, K. Kern

in preparation

Acknowledgements

I would like to express my sincere gratitude to my supervisor, Prof. Klaus Kern. His wide knowledge, comprehensive perspective on scientific questions and logical way of thinking have a remarkable influence on my PhD study.

I am deeply grateful to Prof. Nian Lin, who introduced me into the field of STM and 2D supramolecular chemistry, and Prof. Steven Tait, who guided me into my first x-ray spectroscopic studies. Their patience, enthusiasm and motivating attitude have been very helpful for this study.

I have an immense gratitude to Dr. Sebastian Stepanow. His guidance, insightful comments, extensive discussions have been extremely important through my work.

I wish to give my warmest thanks to my group members who have been always helpful: Alexander Langner, Jingcheng Li, Nan Jiang, Nasiba Abdurakhmanova, Christopher Kley, Jan Cechal, Takashi Kumagai, and Tim Koppenrath. I also want to thank Max Assig, Violetta Sessi, Adarsh Sagar, Theresa Lutz and Gordon Rinke for the pleasant office hours and lunch breaks you create. And I wish to extend my thanks to everyone in the Nanoscale Science Department for the cooperative atmosphere you make.

Finally, my special thanks go to my family. Their love, understanding and encouragement support me throughout my life.

Curriculum Vitae

Name	Tzu-Chun Tseng
Date of Birth	16.11.1982
Nationality	Taiwan
2010	PhD thesis, EPF Lausanne, Switzerland
2007-2010	Research assistant in the group of Prof. Dr. Klaus Kern at the Max Planck Institute for Solid State Research in Stuttgart, Germany
2004-2006	Master thesis in the group of Prof. Tri-Rung Yew at the Department of Materials Science and Engineering of the National Tsing-Hua University, Taiwan: "Integration of Self-Aligned Carbon Nanotube Via with Electroless CoWP Catalyst at Low-temperature (400 °C) for Future CMOS Interconnect"
2004-2005	Research assistant in the Material and Chemical Research Laboratories of the Industrial Technology Research Institute, Taiwan
2000-2004	Undergraduate studies at the Department of Materials Science and Engineering of the National Tsing-Hua University, Taiwan
1997-2000	High school at the Ching-Cheng High School, Chang-Hua, Taiwan